Spectroscopic tools for the study of natural and artificial photosynthetic catalysts

Benedikt Lassalle-Kaiser

MÉMOIRE D'HABILITATION À DIRIGER DES RECHERCHES DE L'UNIVERSITÉ PARIS-SUD

Université Paris-Saclay

Spécialité Chimie

Présenté par

Dr. Benedikt Lassalle

En vue d'obtenir l'habilitation à diriger des recherches de

L'UNIVERSITÉ PARIS-SUD

Sujet du mémoire:

OUTILS SPECTROSCOPIQUES POUR L'ÉTUDE DE CATALYSEURS PHOTOSYNTHÉTIQUES NATURELS ET ARTIFICIELS

Soutenue le 15 Février 2019

Devant le jury composé de:

Mme Hynd Remita	PR, U. Paris-Sud, Orsay	Rapportrice
M. Cyrille Costentin	PR, U. Paris Diderot, Paris	Rapporteur
M. Mark Koper	PR, U. Leiden, Leiden	Rapporteur
Mme Anne Bleuzen	PR, U. Paris-Sud, Orsay	Examinatrice
Mme Serena DeBeer	PR, Max Planck Inst., Mülheim	Examinatrice
M. Jean Daillant	DR, SOLEIL, Gif-sur-Yvette	Examinateur

Table of Contents

Preamble: Natural and Artificial Photosynthesis

Natural Photosynthesis. About 2.5 billion years ago, a solar-to-fuel conversion system was developed by the first living organisms, which was capable of extracting electrons from water using sunlight, in order to power their vital functions. This revolutionary evolution, known as the photosynthetic apparatus, has changed the face of Earth in many aspects.
This nano-scale power plant is composed of several enzymatic units, which all have a precise function to be performed in a concerted way. Light-capturing units absorb photons to generate charge-separated states, which are carried-over on the two opposite sides of a lipidic membrane, where they perform chemical reactions. Two of such photosystems work in series to convert photons into chemical bonds, thus storing solar energy in a small molecule, adenosine triphosphate (ATP). This molecule is then used where required to power various biochemical processes. This whole process, known as photosynthesis, is a solar-to-chemical conversion system that is self-sustained – the complex photosynthetic machinery can be repaired – and is completely renewable, since it uses sunlight, water and carbon dioxide.

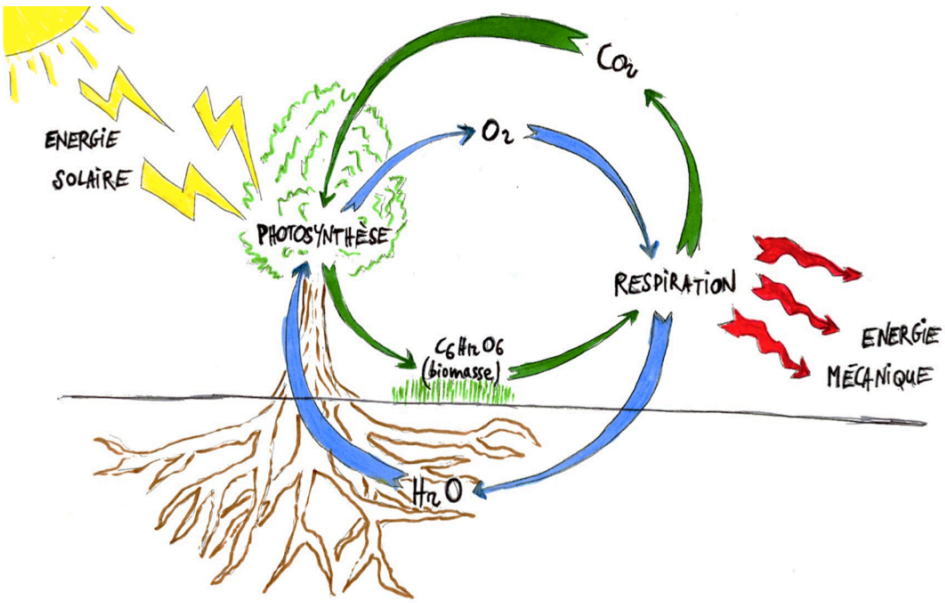

Scheme 1. Simplified representation of the natural photosynthetic and respiration processes.

In higher plants with an annual life cycle, the energy converted during these chemical processes is stored as sugars or fatty acids in organs such as rhizomes, tubers or seeds. These energy-storing units are filled up during the warm and sun-abundant parts of the year and emptied the next year when a new growth period arrives that requires an intense energy surge. Incidentally, these energy-loaded organs are used as energy source by the animal reign. Respiration-based animals have developed a process that converts the chemical energy stored in the chemical bonds of sugars into other chemicals that can fulfill their various energy needs: controlling their temperature, moving around and maintaining vital functions. This process, known as respiration, is complementary to photosynthesis since the products of one process are the reactants of the other one. The combination of photosynthesis and respiration therefore constitutes a fantastic solar-to-power conversion system, as exemplified on scheme 1.

Artificial Photosynthesis. Artificial photosynthesis aims at using sunlight to make chemical bonds and produce energy-storing molecules. It emerged, originally, from the idea that mimicking the activity of natural photosynthetic and respiratory enzymes could lead to conversion processes producing molecules of energetic interest such as dihydrogen or, even better, hydrocarbons, which could be later consumed to recover the stored energy. Although nature uses ATP as its main energy carrier, dihydrogen has been identified as a much more convenient and industrially viable energy carrier.[1] Much work has been devoted to synthesizing mimics of the active sites of enzymes such as hydrogenases[2] or Photosystem II.[3] It turned out, however, that the most faithful mimics were either unable to reproduce the function of their natural counterparts or required drastic conditions to do so. These difficulties in making a structural mimic functional highlighted the challenge to reproduce the precise molecular architecture of metalloenzymes, not only in the first and second coordination spheres of their active sites, but also in their substrate/product delivery channels or their protection and repair mechanisms. Such features are clearly not reproducible with a purely biomimetic approach, as they would imply recreating complete enzymes. Artificial photosynthesis therefore tries to replace each part from a natural enzymatic process with known and mastered synthetic components.

The current challenges of artificial photosynthesis are multiple, but they all pertain to the conversion of solar energy into chemical bonds. Different strategies – modular or integrated – are currently being pursued to convert sunlight into fuels, and they all share in common the need for efficient catalysts. Light capture and conversion can still be optimized, but a lot of research has already been done in the past fifty years, as exemplified by the commercial availability and wide use of solar panels. Fuel-producing electrocatalysis, such as water-splitting has also shown to be technologically ready, but requires the use of noble metals, which scarcity and price make the wide-spread use of this technology unlikely. The development of electrocatalysts, based on earth abundant elements, that can convert small molecules such as water, carbon dioxide or dinitrogen into energy-rich chemicals therefore appears as a critical technological bottleneck.[4] Discovering such catalysts have been the focus of many research groups worldwide, starting in the 70's and efforts are still going on to understand both fundamental and applied aspects of their preparation, functioning and failure behavior. As tempting as it is, inspiration from Nature has not been very successful so far in the field of artificial photosynthesis, at least from a structural and elemental point of view. On the other side, concepts such as charge compensation,[5] second-sphere interactions[6] or multi-photon absorption[7] have been successfully applied to artificial reactions. The last bits of knowledge that are still being sought after in the reactions carried out by Photosystem II, hydrogenases or nitrogenases should certainly be helpful in our endeavor to design efficient and sustainable energy-converting catalysts.

The task to replace the machinery involved in the photosynthesis and respiration processes is immense. It consists, in fact, in finding an evolutionary shortcut that will allow human societies to develop systems as efficient and sustainable as those occurring in plants, which took them millions of years to develop. Unfortunately, we can't wait for millions of years. This is where deterministic approaches, which have been used successfully by mankind to develop its societies and technology, can help. We can hope that logic thinking and careful design will allow finding technological solutions that will mimic the functions of the natural photosynthetic and respiratory processes, within decades rather than billions of years.

Outline of the manuscript. We have been involved in the last ten years in several aspects of research on natural and artificial photosynthesis. More specifically, we have been interested in the study of natural and artificial water oxidizing catalytic system. These studies have been performed at different institutions in France and in the United States under the supervision and in collaboration with many other researchers of the field. Rather then presenting this work in a chronological order, we will describe it following our two main research lines, while the last chapter will be dedicated to our future projects:

Chapter 1 : X-ray spectroscopic studies of Photosystem II and related synthetic models.

In this chapter, we will present our contributions to understand the structure of the active site of Photosystem II and its water-oxidation mechanism. We will describe our work on the characterization of molecular mechanistic models for the water oxidation reaction that occur during natural photosynthesis. We will also show how X-ray techniques on these models and on Photosystem II help understanding the mechanism by which water is oxidized in Nature.

Chapter 2 : *Operando* studies of electrocatalytic systems using X-ray spectroscopies.

This chapter will describe the development of X-ray spectroelectrochemical techniques that were developed and used to study oxygen- and hydrogen-evolving electrocatalytic systems. Several catalysts based on transition metal oxides or sulfides will be described, which structure were determined using *in situ* and/or *operando* X-ray spectroscopies.

Chapter 3 : Time-resolved X-ray spectroscopic and microfluidic tools for the study of the CO_2 reduction reaction.

In this chapter we will present our futures projects, which are centered on the electrocatalytic reduction of CO_2 into valuable chemicals or fuels. One side of it is the further development of *in situ* X-ray spectroscopic techniques with time-resolution capabilities. An other side consists in developing microfluidic systems that can reduce CO_2 following multi-step, sequential reactions.

In a concluding paragraph, we will discuss the progresses made in the last decade and the challenges that lie ahead of the field of artificial photosynthesis.

References

(1) Turner, J. A. ***Science*** **1999**, ***285*** (5428), 687–689.
(2) Tard, C.; Pickett, C. J. ***Chem. Rev.*** **2009**, ***109*** (6), 2245–2274.
(3) Mukhopadhyay, S.; Mandal, S. K.; Bhaduri, S.; Armstrong, W. H. ***Chem. Rev.*** **2004**, ***104*** (9), 3981–4026.
(4) Tatin, A.; Bonin, J.; Robert, M. ***ACS Energy Lett.*** **2016**, ***1*** (5), 1062–1064.
(5) Takashima, T.; Hashimoto, K.; Nakamura, R. ***J. Am. Chem. Soc.*** **2012**, ***134*** (44), 18153–18156.
(6) Costentin, C.; Drouet, S.; Robert, M.; Saveant, J.-M. ***Science*** **2012**, ***338*** (6103), 90–94.
(7) Jacobsson, T. J.; Fjallstrom, V.; Sahlberg, M.; Edoff, M.; Edvinsson, T. ***Energy Environ. Sci.*** **2013**, ***6*** (12), 3676–3683.

Chapter 1 : X-ray spectroscopic studies of Photosystem II and related synthetic models

In this chapter, we will first present Photosystem II (PS II) and the current knowledge on the structure of the oxygen evolving complex (OEC), we will present the structural studies of this enzyme that occurred in the last ten years and in which we have been partly involved, together with the study of synthetic manganese complexes using X-ray spectroscopy. We will finally discuss the possible mechanism for the water oxidation reaction in PS II.

1.1 The mechanism of water oxidation in Photosystem II

Photosystem II is a 10 kDa transmembrane protein composed of several subunits, which collects photons from sunlight and converts them into charges in order to oxidize water on the lumenal side and reduce quinones on the stromal side of the thylakoids membrane. Figure 1-1A schematically describes the structure of PS II, its main cofactors and the sequence of events that lead to the eventual oxidation of two water molecules and the reduction of two plastoquinones. The catalytic cycle corresponding to this photochemical conversion, represented in figure 1-1B and named « Kok cycle » after one of its discoverers,[1] is divided into 5 states, known as the S-states. Each state is generated after a photon is absorbed by PS II, inducing electron and/or proton transfer processes and subsequent structural and electronic changes. The absorption of four photons by the P680 pair of chlorophylls eventually transfers four electrons from two water molecules on the lumenal side to two plastoquinones on the stromal side. These plastoquinones later transfer their electrons through the thylakoid membrane back to the donor side of Photosystem I, which re-energizes them with another photon absorption to further reduce NADH into NADPH. Concomitantly, a proton gradient is generated across the membrane thanks to water oxidation and to a proton-pumping mechanism associated with the plastoquinone re-oxidation. This proton gradient is later used to drive the ADP to ATP synthesis by ATP synthase.

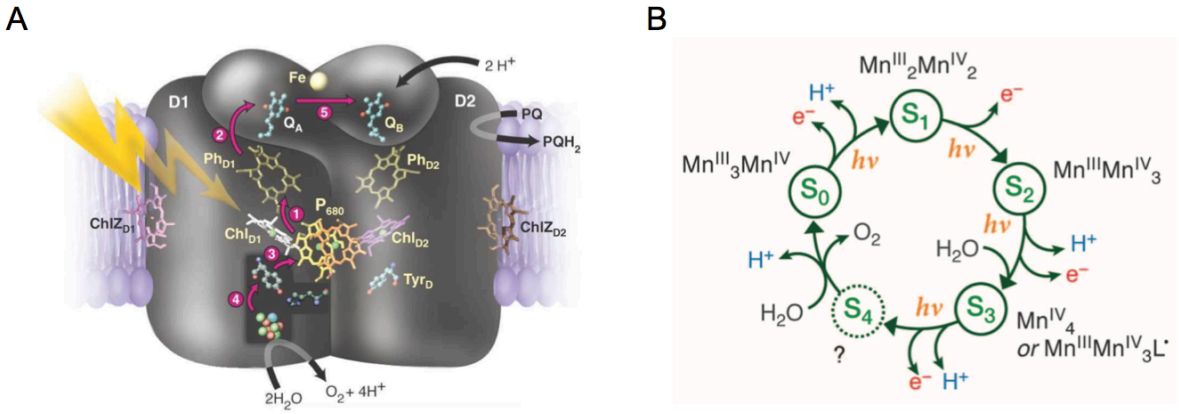

Figure 1-1. Schematic description of Photosystem II from Rutherford and Boussac[61] (A) and Kok cycle as represented by Cox *et al.*[10] (B)

Perhaps the most iconic cofactor of PS II is the active site that is responsible for the water oxidation reaction, known as the Oxygen Evolving Center (OEC). Because it is the locus of the oxygen-oxygen bond formation and because of the potential it holds in inspiring synthetic chemists for the design of artificial photosynthetic systems, the structure and catalytic mechanism of this Mn_4O_6Ca cluster has been extensively studied.[2,3]

Tremendous progresses have been made in our understanding of this active site in the last decades. The first low resolution (3.8-3.7 Å) crystallographic structures of PS II obtained in 2001[4] and 2003[5] were improved to atomic resolution (3.5 Å) in 2004 and a cubane-like structure was proposed,[6] with a fourth, so-called "dangling", manganese site protruding from it. Although X-ray photoreduction remained an issue and molecular details were subject to caution, this structure inspired many mechanistic proposals for the water oxidation reaction. A slightly different, open-cubane structure was proposed in 2006 by Yano *et al.* from polarized EXAFS experiments,[7] which has been later confirmed by high resolution (1.95 Å), radiation damage-free data from XFEL experiments.[8,9] After long debates, the oxidation states of the manganese ions have now been established for the S_0 to S_3 states.[10] Structural data are now available with high resolution, for all of the S-states (except for S_4) and for intermediate states between the S_3 and S_4 states.[11] Although theoretical calculations[12,13] and X-ray spectroscopic data[14] suggest the involvement of an oxygen radical species during the O-O bond formation step, EPR data[10] argue for an all Mn^{IV} structure in the S_3 state.

The mechanism for water oxidation at the OEC have generally been proposed to occur through one of the two following types of mechanisms,[15] which are depicted on scheme 1-1:

i) A nucleophilic attack from a hydroxide ligand bound to a manganese or calcium ion onto a highly electrophilic oxygen belonging to an Mn^{IV} or Mn^{V}-oxo species. This mechanism was long favored because several synthetic Mn^{IV}-O or Mn^{V}-O species were isolated and characterized, which exogenous oxo ligand showed electrophilic character. The possibility to transfer this oxygen atom to oxophilic species such as phosphines or thiols suggested a similar reaction with another nucleophilic oxygen species.

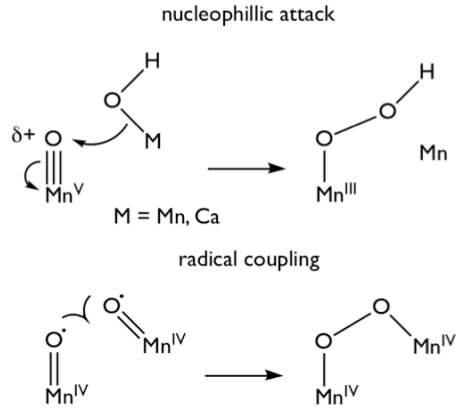

Scheme 1-1. "Nucleophillic attack" and "radical coupling" simplified mechanisms proposed for the O-O bond formation at the OEC.

ii) The coupling of two manganese-bound oxygen species with radical character. The involvement of oxygen radical species was proposed by the Berkeley group in light of their XAS data, which suggested an oxidation that was not centered on the manganese ions from the S_2 to S_3 transition.[14] Later calculations also favored this type of mechanism,[12] although Mn^{IV}-oxyl species have never been isolated and described in the literature as far as we are aware of.

Discriminating these two types of mechanism required a comparison of spectroscopic data measured on both photosystem II in the most advanced S-states and on model compounds having structural similarities with the OEC. Such models were scarce or non-existent 10 years ago, but thanks to hard synthetic work, new species were isolated that proved essential in this comparative work. The next two parts will present spectroscopic data on both PS II and synthetic Mn compounds, in the collection of which we have participated over the past 10 years. These data, along with those measured and analyzed by many other groups worldwide bring their contribution to a better understanding of the OEC and its water oxidation mechanism. The present state of knowledge and current hypotheses will be described in the last part of this chapter.

1.2 Structural and spectroscopic studies of Photosystem II using an X-ray Free Electron Laser

1.2.1 General considerations about serial crystallography experiments at XFELs

Tremendous progresses have been made in the last decade in the description of the 3D arrangement of the OEC, using X-ray diffraction and spectroscopic experiments at synchrotron and free-electron laser sources as well as other spectroscopic techniques such as EPR[16] and computational chemistry.[12] From the very original XRD structure of PS II from Zouni *et al.* in 2001,[4] the resolution has kept improving to current values close to or below 2.0 Å.[9,17,18] Although X-ray induced radiation damages have been an issue in the early days of both synchrotron and XFEL based structures,[19] radiation damage-free data have now been collected using the so-called « collect-before-destroy » approach. This technique was proposed by Neutze and Hajdu[20] and popularized by Chapman and others[21] in conjunction with the advent of XFELs. It allows determining the three-dimensional structure of an ordered biological object (*e.g.* a protein crystal or a virus capsid) at room temperature and with time-resolution. The principle of this technique consists in exposing a crystallized sample of very small size (in the microns range) to an X-ray pulse so intense (10^{12} photons / pulse) that diffraction and/or spectroscopic data can be collected in a single shot. The pulse used is so short-lived (tens of fs) that the data can be collected before the sample is irreversibly destroyed. The « collect-before-destroy » approach is schematically described on Figure 1-2, although many variations of it have been reported.

Since 2011, the group led by Vittal Yachandra and Junko Yano at the Lawrence Berkeley National Laboratory have set up an international consortium to determine the three dimensional and electronic structure of the OEC in its different S-states and the associated catalytic cycle for the oxidation of water. This consortium involves collaborators from many countries and institutions, each one taking care of a specific part of the project: PS II purification and crystallization (A. Zouni, Humbold Universität Berlin and J. Kern, LBNL), model compounds synthesis (A. Borovik, UC Irvine and T. Agapie, Caltech), sample injection

(M. Bogan, SLAC, S. Gul and F. Fuller, LBNL), spectrometer development (U. Bergmann and R. Alonso-Mori, SLAC and P. Wernet, Helmholtz Zentrum Berlin), sample illumination setup (J. Messinger, Uppsala Universitet) crystallographic data refinement methods (P. Adams and N. Sauter, LBNL) and theoretical calculations (P. Wernet, Helmholtz Zentrum Berlin).
As a post-doc in the group of V. Yachandra and J. Yano at LBNL, we had the chance to be involved in this project, preparing model compounds, developing sample injection methods and collecting data. The next two sections describe the experiments that were carried out while we were participating in the consortium but also, for the sake of clarity, a few results that were obtained after our stay and without our contribution.

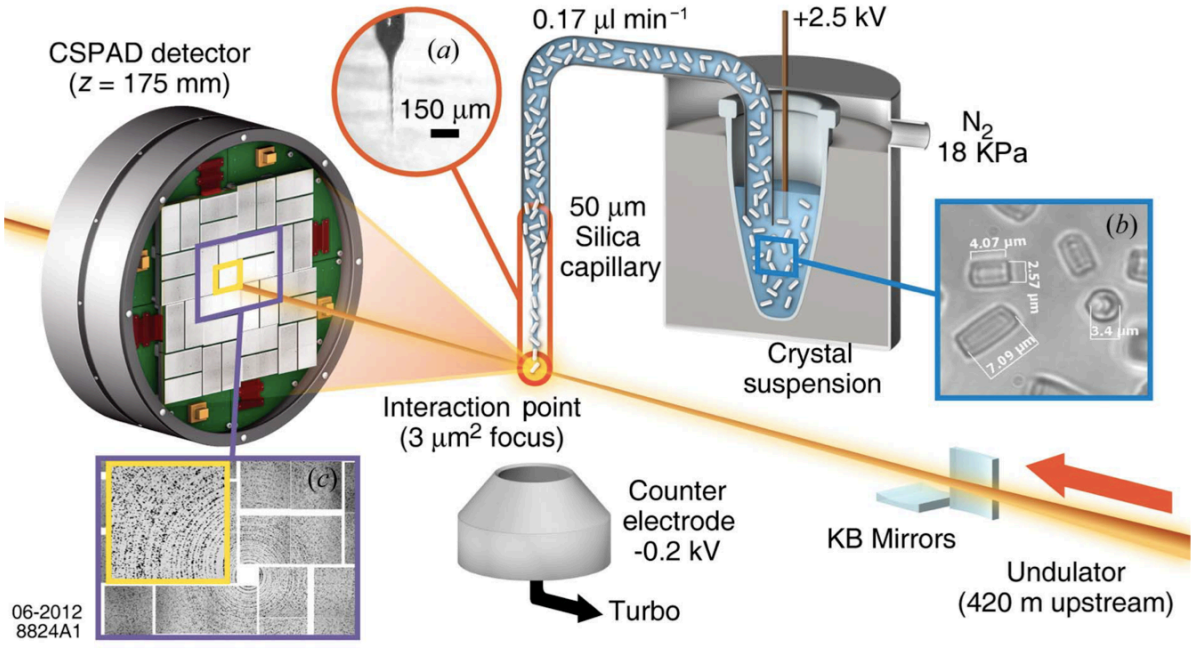

Figure 1-2. Schematic description of a collect-before-destroy XFEL experiment as presented in Sierra *et al.*[22] CSPAD stands for Cornell-Stanford Pixel Array Detector. The Von Hamos X-ray emission spectrometer, not repreented on this figure, is located on the side of the interaction point, perpendicular to the incident beam.

1.2.2. Hard X-ray diffraction and spectroscopic experiments on PS II at the LCLS.

Much progress have been achieved since the first experiments run by the Berkeley group about 8 years ago; we will describe them in chronological order.
The first experiments goal was to simultaneously collect XRD and X-ray emission data on PS II microcrystals in the different S-states of the Kok cycle. The sample injection system described on figure 1-2 and used for the first PS II experiments at LCLS uses a specific electrospray technique, which allows the consumption of very low amounts of samples (flow rate of 0.5-2 µl/min).[22] An illumination setup affixed at the end of the injection capillary was designed to illuminate PS II microcrystals and advance them along the Kok cycle just before

being shot by an LCLS X-ray pulse. An XRD detector located downstream of the interaction point and a Von Hamos-type X-ray emission spectrometer[23] placed at 90° to the incident beam would collect diffraction and emission data for each crystal shot, respectively. Data were first collected on thermolysin, a model protein which data were later used to calibrate the crystallographic refinement procedure developed by Nick Sauter and his team.[24] These data were also used to demonstrate the validity of the electrospun microfluidic jet,[22] which was specifically designed for a much lower sample consumption than the "gas driven virtual nozzle" (GDVN) technology (µL *vs.* mL). X-ray emission data were measured on synthetic manganese compounds, which were essential in demonstrating, for the first time, the potential application of this technique to XFEL measurements.[25] Finally, the first X-ray diffraction data were collected from PS II.[26] Their low resolution did not improve our understanding of the structure or behavior of PS II at the time, but it showed that microcrystals of PS II could survive the harsh conditions of this experimental setup and thus demonstrated the feasibility of the experiment. The following experiments were more successful each time, although injection of PS II into vacuum chambers remained a challenge until it was replaced by other methods (*vide infra*).[27] The next achievement of the consortium was the simultaneous measurement of XRD and XES data on PS II microcrystals.[28] In this experiment, both XRD and XES data were collected at room temperature on microcrystals of PS II in the dark (S_1) and single flash (S_2) states. The XES data collected simultaneously to XRD show that the microcrystals were intact and did not suffer from any radiation-induced damage (see figure 1-3A), which was also true for solutions of PS II (see figure 1-3B).

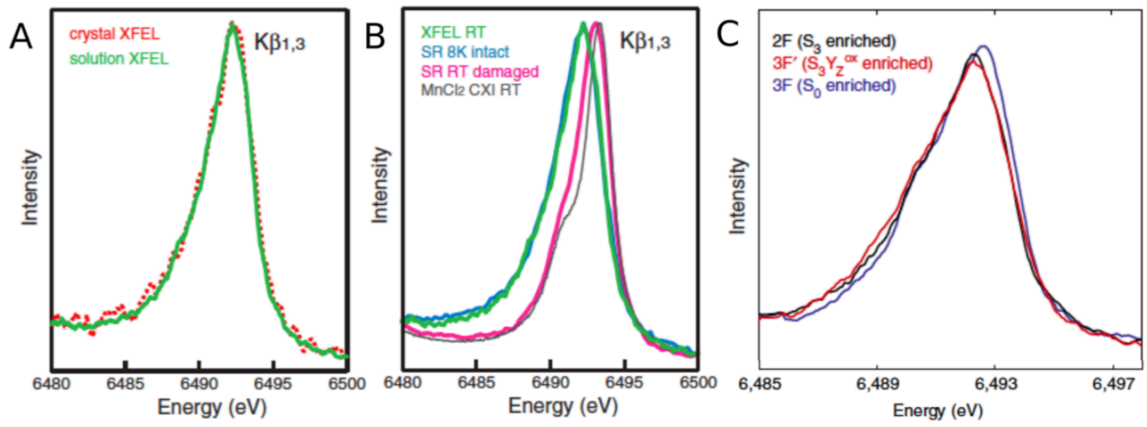

Figure 1-3. Mn $K\beta_{1,3}$ XES spectra measured at room temperature at the LCLS on : a solution (0.8 mM in Mn) and crystals of PS II (A), a PS II solution and a $MnCl_2$ solution (500mM), compared to synchrotron measurements on an intact PS II solution measured at 8K and a damaged PS II solution measured at room temperature (B) and on S_3 enriched (2 flashes), S_0 enriched (3 flashes) and $S_3Y_z^{ox}$ enriched (3 flashes + 250 ms) PS II solutions (C). CXI stands for "Coherent X-ray Imaging" beamline.

Another achievement was the measurement of XES spectra on PS II solutions in the S_3, S_0 and S_3 + 250ms states.[29] Figure 1-3B shows the time-resolved XES spectra of PS II after two, three or three flashes + 250ms. The reduction of the manganese centers after three flashes

and the formation of the S0 state can be clearly seen as a shift of the peak towards higher energies. On the contrary, the absence of any shift 250 ms after the third flash indicates that the evolution of O_2 occurs after this point.
Although we did not participate in these experiments, it is worth mentioning that improvements in the crystals quality and in the sample injection method[27] led to the collection of XRD data at 2.25 Å resolution for the S_1, S_3 and ammonia-bound S_3 states.[9] Another study by Suga *et al.* was also published shortly after, which presented crystallographic data of the S_1 and S_3 states of PS II, proposing the formation of an O-O bond already in the S_3 state.[18] As this manuscript was being prepared, the crystallographic structures of all meta-stable S-states (S_0, S_1, S_2 and S_3), as well as different points in time between the S2 and S3 states, were published by the Berkeley group.[11]

1.2.3. Soft X-ray spectroscopic experiments on PS II at the LCLS.

In parallel to the collection of these structural pieces of information, a series of experiment was carried out using the Soft X-Ray (SXR) beamline of the LCLS, in order to measure Mn L-edge spectra of PS II at room temperature. All previous attempts to measure L-edge spectra of PS II (and other metalloenzymes) led to its complete reduction due to X-ray damage and the spectra obtained were characteristic of manganese(II) species. The advent of XFELs and the development of the "collect-before-destroy" approach described above made it possible to design experiments for the collection of Mn L-edge spectra of PS II. These experiments were led by the Berkeley group, in strong collaboration with the group of Philippe Wernet at the Helmholtz Zentrum in Berlin. His team developed optical zone plates, which allows distinguishing the Mn Lα (637.4 eV) and the O Kα (524.9 eV) fluorescence signals of PS II.

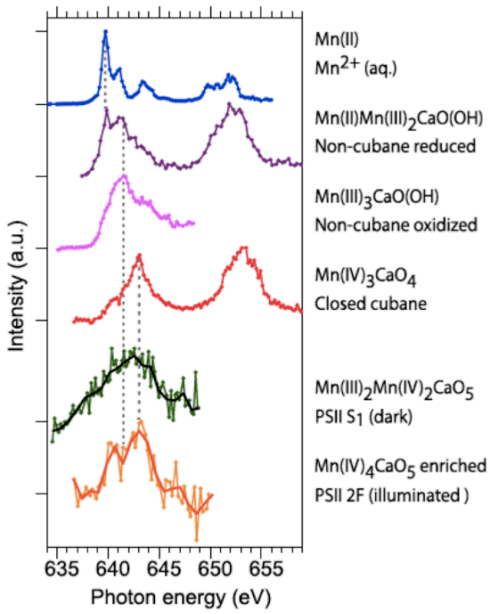

Figure 1-4. Mn L-edge spectra of inorganic model complexes and of PS II in the S_1 and S_3-enriched state. All spectra were measured at room temperature in solutions.

These experiments proved being as challenging as the crystallographic ones and the first series only led to proof of principle results, showing that L-edge spectra of $Mn(II)Cl_2$ concentrated solutions could be measured using this setup and the LCLS beam without perturbing its spectroscopic signature.[30] Further experiments focused on more sophisticated, polynuclear manganese model compounds as well as PS II solutions.[31] After several beamtimes and intense efforts, undamaged Mn $L_{2,3}$- and L_3-edge spectra were measured on $Mn^{II}Mn^{III}_2Ca$, Mn^{III}_3Ca and Mn^{IV}_3Ca model compounds, as well as on PS II in the S_1 and S_3 states, which are shown on

figure 1-4. Although the improvement of the signal quality for PS II requires technological improvements of the spectrometer and detector, the current configuration of the experiment is appropriate for the study of model compounds in the 5-20 mM range. These experiments on PS II and model compounds in the soft X-ray range are being continued in order to improve the data quality.

1.3 X-ray spectroscopy of highly-valent manganese complexes, models of the OEC

The study of the OEC's structure has long been backed by the study of synthetic manganese complexes, with geometric and/or electronic structures somehow reproducing that of the OEC. Comparing the spectroscopic signatures of these models to those of the natural system was very helpful in determining it's geometric and electronic arrangement. This was particularly true when no XRD structure was available for PS II and many geometrical structures were still considered. Now that the structure of the OEC is known in the early S_1 and possibly S_2 states, the comparison with synthetic systems remains useful, but considering the higher S-states, where the O-O bond is formed. The challenge is therefore even higher, since the potential intermediates are likely to be less stable and thus not comparable to any known or synthetically accessible model compound. Efforts are nevertheless directed in many groups worldwide towards the synthesis and study of mononuclear and polynuclear complexes that can model the OEC, either structurally or mechanistically. While polynuclear complexes provide signatures for specific Mn-O-Mn or Mn-O-Ca interactions that can be compared to the natural system, highly-valent mononuclear complexes give clues on the spectroscopic signatures that one could expect from highly reactive, transient intermediates in the OEC's catalytic cycle.
The following two paragraphs describe X-ray spectroscopic studies we have performed on mononuclear and polynuclear manganese complexes that model the OEC, either mechanistically or structurally. These studies were realized through collaborations with other groups whose main expertise is the preparation of such delicate synthetic complexes.

1.3.1. Mononuclear systems

1.3.1.1 Case of a series of octahedral $Mn^{III/IV}$ complexes with an exogenous hydroxo, chlorido or methoxo ligand.

We have been involved in the synthesis and study of mononuclear manganese complexes since our PhD work,[32] which was dedicated to the preparation and study of mononuclear manganese complexes for the activation of water. This work was partly continued after our graduation, notably by Dr. Sanae El Gachtouli,[33–35] a post-doctoral fellow at the *Institut de*

Chimie Moléculaire et des Matériaux d'Orsay, and we therefore took the opportunity to perform X-ray absorption experiments on some of these complexes. We particularly focused our attention on a series of mononuclear manganese complexes in an octahedral coordination sphere, bearing a single exogenous ligand (OH^-, CH_3O^- or Cl^-), and isolated in the +III and +IV oxidation states. Figure 1-5 shows the $_{tBu}$LH ligand used for this study, together with the ORTEP diagrams of the $_{tBu}$LMn^{III}-OH and $_{tBu}$LMn^{III}-Cl complexes.

The $_{tBu}$LH ligand, represented on figure 1-5A is monoanionic and pentadentate, which leaves a single free coordination position, and features *tert*butyl groups on the *para* and *ortho* position of the phenolic ring in order to avoid dimerization between two mononuclear units. The hydroxo, chloro and methoxo derivatives of these complexes were synthesized by reaction of the ligand with one equivalent of Mn(II) perchlorate, in the presence of dioxygen (non-inert atmosphere) and yielded the Mn(III) derivatives. The structures of the hydroxo and chloro compounds (see figure 1-5B and 1-5C, respectively) present similar features, with an identical arrangement of the $_{tBu}L^-$ ligand and a compressed Jahn-Teller axis along the N_1-Mn-X axis (X=OH, Cl). Interestingly the Jahn-Teller distortion was clearly observed in the EXAFS Fourier transform signal of the Mn(III) complexes, while it totally disappeared for the Mn(IV) complexes (data not shown).

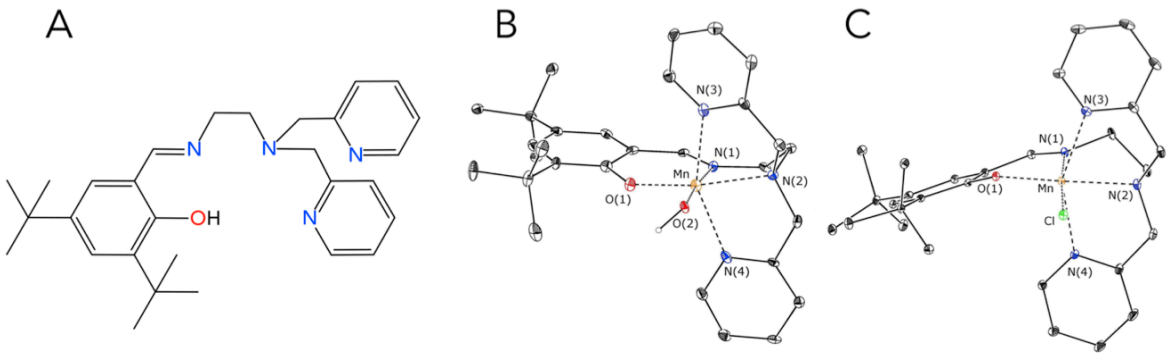

Figure 1-5. Semi-developed structure of the $_{tBu}$LH ligand (A), ORTEP diagrams of the $[_{tBu}LMnOH]^+$ (B) and $[_{tBu}LMnCl]^+$ (C) complexes. Ellipsoids are drawn with a 50% presence probability.

The Mn(III) complexes were then dissolved in acetonitrile and oxidized electrochemically by one electron to generated the corresponding Mn(IV) complexes. Aliquots of the Mn(III) and Mn(IV) solutions were frozen for XAS experiments. X-ray absorption spectra were recorded at the manganese K-edge at the 7-3 beamline of the Stanford Synchrotron Radiation Lightsource (SSRL) at the Stanford Linear Accelerator Center (SLAC). Samples were kept frozen in a liquid helium cryostat during the measurements and radiation-induced damages were carefully checked.

Figure 1-6 A, B and C shows the manganese K-edge absorption spectra for the Mn(III) and Mn(IV) series. As expected, the main edge energy position is shifted towards higher values for the Mn(IV) complexes with respect to their Mn(III) counterparts. The pre-edge region, shown in the insets of figure 1-6 A, B, C show low-intensity double features, which correspond to the d-block t_{2g} and e_g orbitals in high spin Mn(III) and Mn(IV). Figure 1-6 D and E compares the

three species for the +III and +IV oxidation states respectively. It is worth noting that the Mn(IV)hydroxo complex has an edge position that is higher than the two other complexes, suggesting that the charge is mostly present on the metallic center rather than on the hydroxide ligand. A double-peak can also be observed for this species in the pre-edge region, whereas the two other only features a single one. Comparing the spectral signatures of these complexes helps understanding their electronic structures and provides blueprint elements in understanding more complex systems such as photosystem II. An in depth understanding of their electronic structures would require, however, the use of advanced theoretical tools.

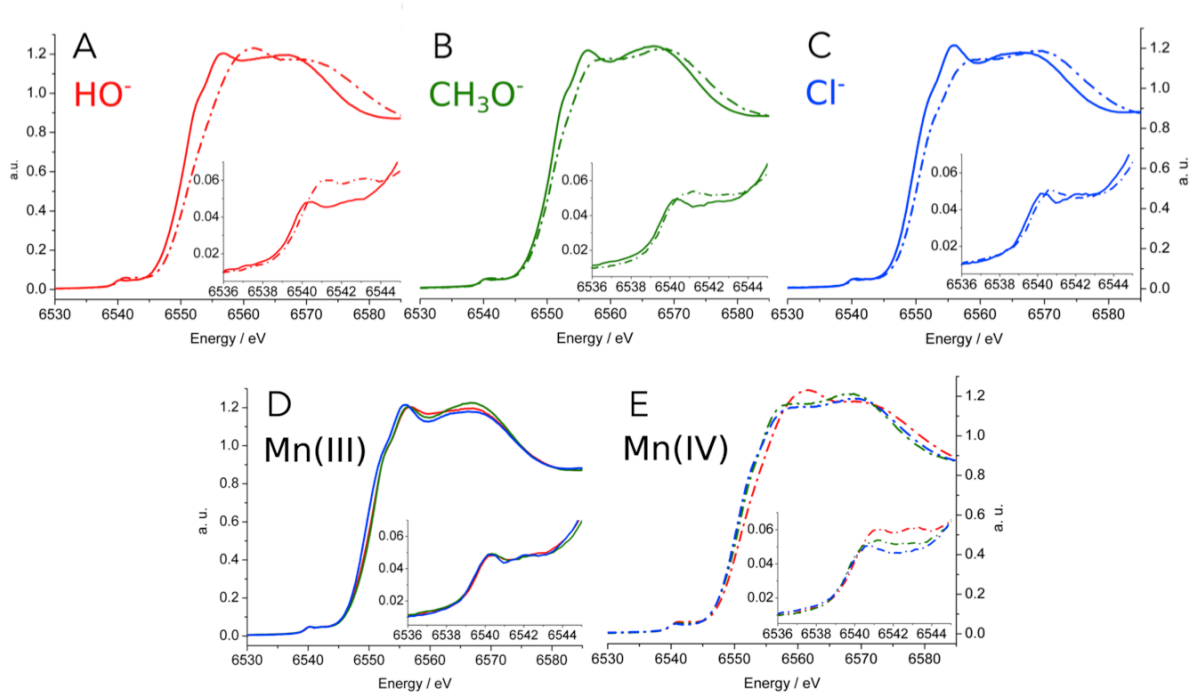

Figure 1-6. Manganese K-edge XAS spectra for the following series of complexes: (A) $_{tBu}$LMn(III)OH (red plain) and $_{tBu}$LMn(IV)OH (red dashed), (B) $_{tBu}$LMn(III)OMe (green) and $_{tBu}$LMn(IV)OMe (green dashed), (C) $_{tBu}$LMn(III)Cl (blue) and $_{tBu}$LMn(IV)Cl (blue dashed), $_{tBu}$LMn(III)OH, $_{tBu}$LMn(III)OMe and $_{tBu}$LMn(III)Cl (D) and $_{tBu}$LMn(IV)OH, $_{tBu}$LMn(IV)OMe and $_{tBu}$LMn(IV)Cl.

1.3.1.2 Case of a series of pentacoordinated, trigonal bispyramidal $Mn^{II/III/IV/V}$ complexes with aquo, hydroxo or oxo ligands.

During our post-doctoral stay at LBNL, we had the opportunity to collaborate with the group of Pr. Andrew Borovik, at the University of California in Irvine, who is an expert in the preparation of biomimetic, highly-valent manganese and iron complexes.[36] In particular, he has developed a family of tripodal ligands, which allows the coordination of a metal in a trigonal pyramid geometry, leaving a free coordination position for an exogenous ligand. Using this scaffold, his group has prepared several manganese or iron hydroxo and oxo

compounds in high oxidation states, which mimic intermediate states of manganese or iron containing enzymes.[37] Although these compounds are very delicate and need to be manipulated with the highest precautions, their relative stability is made possible thanks to the interaction of second sphere interactions between pendant groups affixed to the ligand scaffold and the exogenous oxygen ligands (hydroxo or oxo).[38] Considering intermediate species along the water oxidation reaction at the OEC of PS II, manganese(IV/V)-oxo intermediates have often been postulated, the electrophilicity of their oxo ligand being key to the formation of an O-O bond. Examples of such Mn^{V}-O (with an Mn-O triple bond) in a square pyramidal geometry have been described,[39,40] but they did not show the reactivity nor spectroscopy expected for a highly reactive electrophilic species.[41] On the contrary, manganese-oxo complexes in a trigonal bypiramidal geometry were postulated to present a different spin configuration, hence reactivity. The energy diagrams of such high and low spin configurations of Mn(V)-oxo complexes in octahedral and trigonal bipyramidal geometries are shown on scheme 1, together with the chemical structure of a Mn(III) complex coordinated by the H_3buea^{3-} ligand developed and used by the Borovik group.

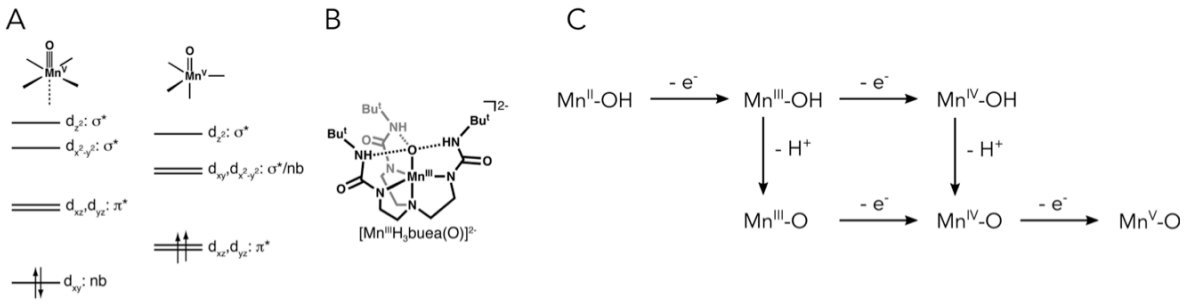

Scheme 1-2. (A) Simplified energy diagrams of high and low spin configurations of Mn(V)-oxo complexes in octahedral and trigonal bipyramidal geometries, (B) chemical structure of the $[H_3$bueaMn(III)-O$]^{2-}$ complex and (C) series of complexes we have studied spectroscopically and their electron/proton transfer relationships.

In 2006, The Borovik group reported a Mn(IV)-O complex in a trigonal bipyramidal geometry which presented reactivity and spectroscopic features that were compatible with what is observed or expected in PS II.[42] In this context, collecting extensive spectroscopic information on this type of complexes presented a very high interest for comparison with spectroscopic data on PS II. A whole family of Mn^{n+}-OH_x (n=2, 3, 4, 5 and x=0, 1) complexes, represented on scheme 1 (C), with various oxidation and protonation states were prepared by the Borovik group and spectroscopically characterized, using XAS and XES in our case, but also using EPR spectroscopy.[43,44] In particular, the very first Mn(V)-O complex in a low spin configuration was prepared and extensively studied using multiple spectroscopic techniques.[45]

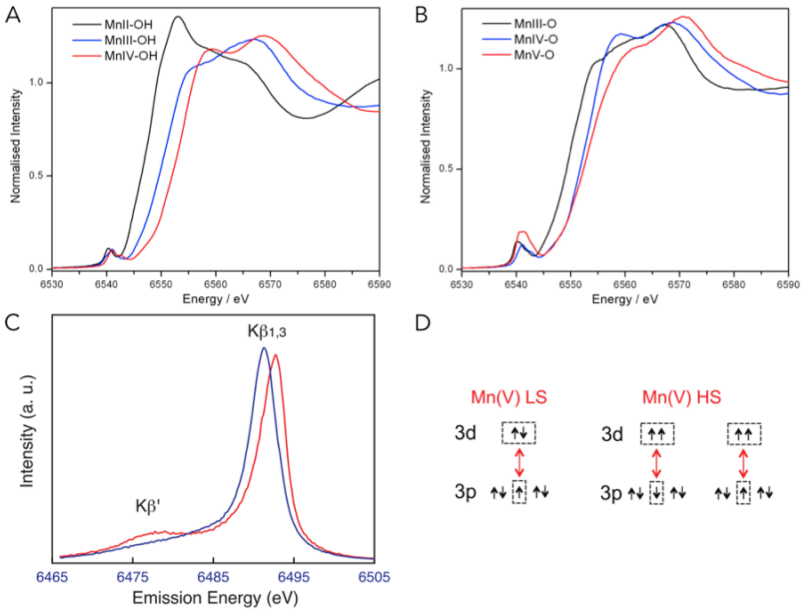

Figure 1-7. Manganese K-edge XAS spectra of the H_3bueaMn-OH (A) and H_3bueaMn-O (B) series, manganese K-edge $K\beta_{1,3}$ X-ray emission spectra for the [H_3bueaMn^{V}O] (red) and [DMBMn^{V}O] complexes (C) and simplified scheme describing the core-hole excited state configuration for high and low spin Mn(V)-oxo complexes (D).

Figure 1-7A-B presents the manganese K-edge XANES data collected on the series of the [H_3bueaMn-X] (X=O, OH) complexes at cryogenic temperatures. As observed previously in another mononuclear manganese complex in an octahedral environment featuring a single exogenous water molecule,[46] an edge energy shift is observed on going from lower to higher oxidation states, the shift being more pronounced for lower (*i.e.* from Mn(II) to Mn(III)) than for higher (*i.e.* from Mn(IV) to Mn(V)) oxidation states. In the hydroxo series, the pre-edge features are notably weak in intensity, which is known and expected for single metal-oxygen bonds. In the oxo series, the pre-edge intensity of the Mn(V)-O complex is more intense than that of the Mn(IV) or Mn(III) counterparts, but still much less than for a low spin, square pyramidal Mn(V)≡O complex, in which the pre-edge features accounts for about 50% of the main edge jump.[47] This high pre-edge intensity in this low spin, square pyramidal complex was used as a marker to rule out the presence of such a species in the water oxidation mechanism at the OEC up to the S_3 state.[41] The decreased pre-edge intensity observed in the [H_3bueaMn^{V}O] complex reshuffles the cards and rehabilitates the possible presence of a transient Mn^{V}-O species along the water oxidation at the OEC, but in a geometry containing a C3 rather than a C4 symmetry axis, and with a high spin configuration.

The high spin configuration of the [H_3bueaMn^{V}O] complex was demonstrated using, among other techniques, manganese K-edge X-ray emission spectroscopy, which spectra are displayed on figure 1-7 (C). This technique measures the energy of photons emitted from the recombination of a higher orbital electron into the core hole generated from the absorption of an X-ray photon. When the electron originates from the 3p orbitals, the emission peak is

called $K\beta_{1,3}$ (also known as Kβ main line) and is sensitive to the spin state of the sample due to interactions between the p and d orbitals in the final state after the core hole is filled.[48] In the case of a Mn(V) species, which has a d^2 electronic configuration, the outcome is simple: there are either one single (LS) or two final states (HS) depending on the spin configuration of the d-block. A single state (LS) therefore gives rise to a single peak, while two final states (HS) give rise to two peaks, a high intensity one for constructive interaction between the p and d orbitals, and a low intensity one for destructive interactions. This situation has been observed in the case of two Fe(III)-oxo complexes in low and high spin configurations.[49] The XES measurement performed on the [H_3bueaMn^{V}O] and [DMBMn^{V}O] complexes show this exact spectroscopic signature, *i.e.* a singlet for the low spin [DMBMn^{V}O] complex and a doublet for the [H_3bueaMn^{V}O] complex, thus assessing its high spin configuration. The comparison between the series of model compounds prepared by the Borovik group, which we have studied using X-ray spectroscopies, and the OEC has been specifically discussed by us[44] and others[50] in 2015.

1.3.2. Polynuclear systems

Polynuclear manganese complexes have long been very valuable synthetic models when trying to understand the structure of the OEC of PS II.[51] The advent of advanced X-ray spectroscopic techniques such as XES make it worthwhile revisiting the spectroscopic signature of some of these structural biomimetic complexes. We have collaborated with the group of Pr. Vincent Pecoraro from the University of Michigan, who has been synthesizing numerous manganese biomimetic complexes for many years. In order to demonstrate the potential of the valence-to-core X-ray emission spectroscopy and use it as a tool to identify intermediate species in the OEC, we focused our attention on a series of complexes, originally synthesized in 1994 by Dr. Baldwin,[52] and which features a dinuclear Mn^{IV}_2 core, held together by oxo and/or hydroxo bridges.

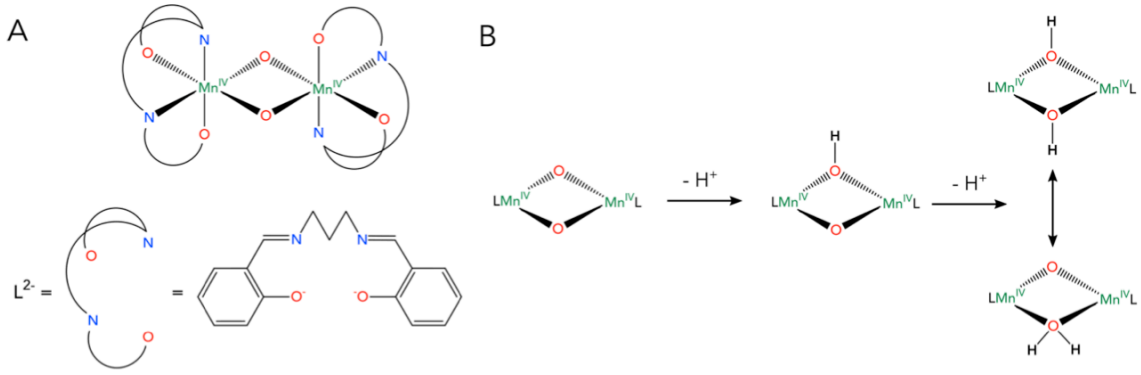

Scheme 1-3. Semi-developed chemical structure of the salpen ligand and general structure of the [(salpen)$_2$Mn$^{IV}_2$O$_2$H$_x$] (x=0,1,2) complexes (A). Simplified representation of the complexes considered in this study (B).

Scheme 1-3 shows the chemical structure of the organic ligand used in this study, as well as the series of complexes that were measured spectroscopically. Remarkably, the series consists of three complexes that only differ by the sequential protonation of each of the bridging oxygen atoms. The complexes that has been protonated twice (starting from the di-μ-oxo complex) can adopt two forms, one with a di-μ-hydroxo bridge and one with a μ-oxo, μ-aquo bridge. Although the di-μ-hydroxo seems more likely in terms of chemical stability, the original study by Baldwin *et al.*[52] could not provide a definite evidence to distinguish between these two species.

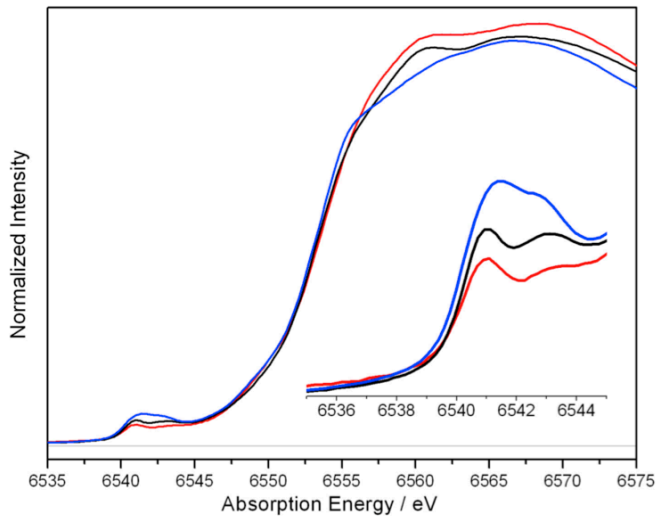

Figure 1-8. Manganese K-edge XAS spectra of $Mn^{IV}_2O_2$ (blue), $Mn^{IV}_2O_2H$ (black) and $Mn^{IV}_2O_2H_2$ (red) species (A), with the pre-edge region in inset.

X-ray absorption[53] and emission[54] (both $K\beta_{1,3}$ and $K\beta_{2,5}$) at the manganese K-edge were collected on these three samples at beamlines 7-3 (XAS) and 6-2 (XES) at SSRL. The XAS data collected on this series of complexes is presented on figure 1-8. The first feature to observe on the Mn K-edge XAS data of the series, presented on figure 1-8 is the quasi-absence of any shift in the main edge position. This confirms the +IV/+IV oxidation state of the dimer and also indicates that single and double protonation of the bridge does not impact significantly the Mn K-edge position of these complexes. Looking at the pre-edge region (inset of figure 1-8) it can be seen, however, that the peaks position and relative intensities change with the degree of protonation. This is expected, since hydroxo and oxo ligands should not have the same orbital overlaps with manganese, thus modifying the d-block arrangement and the p-d orbitals mixing. DFT calculations were performed using the high spin and broken symmetry wavefunctions to simulate the pre-edge regions of these spectra (data not shown). Without discussing in details the parameters and results of these calculations, which are beyond the scope of this manuscript and can be consulted elsewhere, it can be easily noted that both procedures lead to a single conclusion: the μ-oxo, μ-aquo dimeric species postulated for the doubly protonated species does not match at all any of the experimental data, thus completely discarding it.

X-ray emission spectroscopy, as described in part 3.1 of this chapter, probes the electronic structure of the filled orbitals of a given element. Several recombination processes can occur to fill the excited core-hole in a first row transition metal: 2p → 1s ($K\alpha$ transition), 3p → 1s ($K\beta_{1,3}$) and 3d → 1s ($K\beta_{2,5}$), with a decreasing occurrence probability as the energy difference between the core hole and the level providing the recombining electron increases. The 3d to

1s recombination process, also known as valence-to-core, is of particular interest in our case, since it probes the d-block orbitals and as such, also holds information on the ligands bound to the excited metal center. This transition indeed features a satellite transition, called Kβ" or *crossover* peak, which originates from the recombination of an electron from a 2p orbital from the ligand into the core hole of the metal. Figure 1-9A schematically describes this process. Series of manganese model compounds have been studied by other groups using this spectroscopy in order to identify the main features observed as a function of the metal oxidation state, the nature of the ligand or its binding mode.[55,56] Such data on oxo-bridged manganese complexes in different protonation states are very valuable blueprints for later comparison with data collected on the OEC. We therefore measured the $K\beta_{1,3}$ (main line) and $K\beta_{2,5}$ (valence-to-core) data on the $Mn^{IV}_2O_2H_x$ (x=0,1,2) series, which are shown on Figure 1-9B. As expected, the main line transition does not present any significant shift in energy for the $Mn^{IV}_2O_2$ and $Mn^{IV}_2O_2H$ compounds. A slight shift towards higher energies is observed for the $Mn^{IV}_2O_2H_2$ sample, which corresponds to a formal reduction, and is explained by a slight increase of the electronic density on the manganese ion induced by the protonation of the two bridges. The crossover peak in the valence-to-core spectra show an evolution that follows the protonation state of the di-μ-oxo bridges: a peak with a high intensity is observed at 6520.5 eV for the non-protonated species, while another low intensity, single peak is observed at lower energy (6517.5 eV) for the doubly protonated species. These observations follow the trend expected from the literature,[48] *i.e.* higher intensity peaks at higher energies for stronger, shorter bonds. Interestingly, the intermediate, singly protonated species presents two distinguishable peaks that correspond to the positions of the purely non-protonated or doubly protonated species.

DFT calculations were again performed in order to correlate the spectral features observed with a detailed electronic structure. The results are shown on figure 1-9C and show that the crossover peaks contain contributions from the oxo, hydroxo and aquo bridging ligands, but also from the oxygen and nitrogen atoms from the salpn ligand. The contributions from the salpn ligand are shown to be negligible, which is expected since their orbitals are too involved in the salpn organic framework to have a significant contribution into the metal's orbitals. Similarly, the contribution of an aquo bridging ligand is calculated to be negligible, again because of the involvement of the oxygen's orbitals in the O-H bonds. On the contrary, the orbitals of the oxo and hydroxo ligands in the bridge are the main contributors to the crossover peak for compounds 1 ($Mn^{IV}_2O_2$), 2 (Mn^{IV}_2OOH), and 3a ($Mn^{IV}_2OH_2$). The energy positions found for these contributions match very well with the measured data and confirm the original attribution of these peaks. This combination of experimental and theoretical data showcases the power of valence-to-core X-ray emission spectroscopy in distinguishing the presence of a single proton on a bridging oxygen atom. It therefore appears like an essential technique for the study of metal-containing enzymes[57,58], molecular catalysts[56,59] or other materials where the role of light elements is critical.[60]

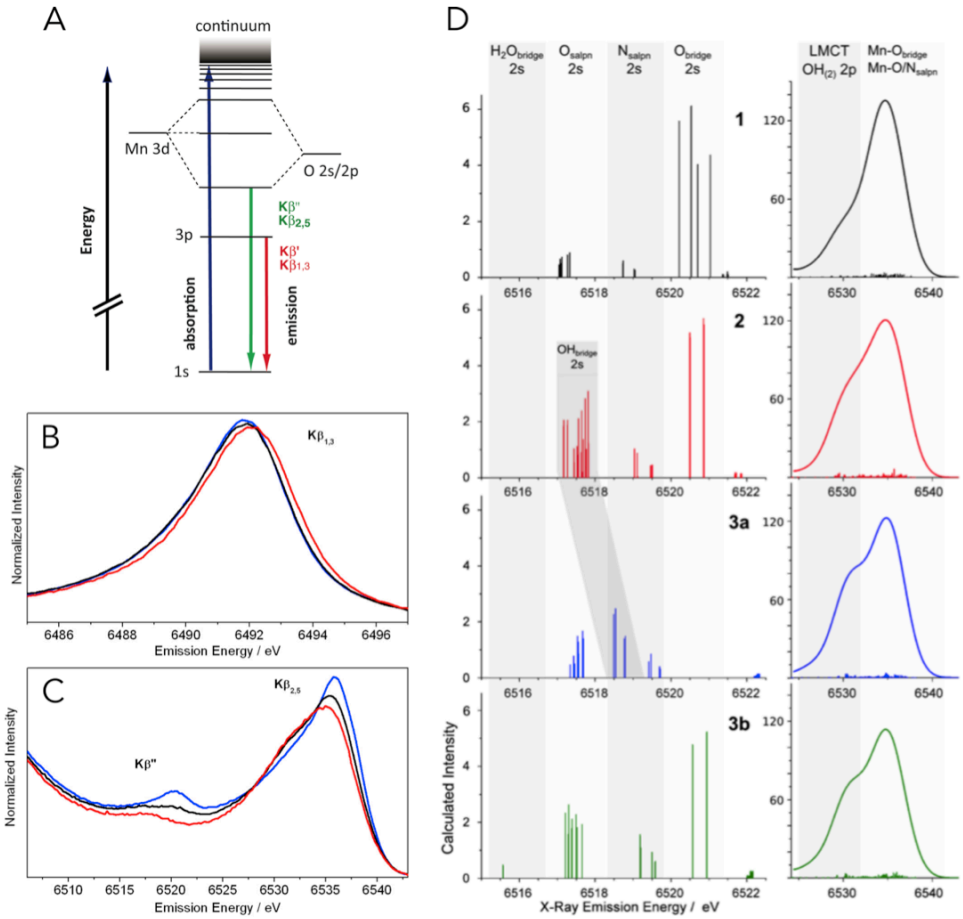

Figure 1-9. Schematic diagram of the X-ray absorption and emission processes (A), X-ray emission $Kb_{1,3}$ (B) and $Kb_{2,5}$ (C) spectra recorded on the $Mn^{IV}_2O_2$ (blue), $Mn^{IV}_2O_2H$ (black) and $Mn^{IV}_2O_2H_2$ (red) species and DFT calculations performed with the Orca software on these compounds (D).

1.4 Implications for the water oxidation mechanism in the OEC

Several milestones have been reached within the last ten years in our understanding of the OEC and major breakthroughs are currently being reached. It was shown that PS II can be studied at room temperature in its different S-states, without any radiation-induced damages, using time-resolved XRD and XES. The community is now just starting to benefit from the work that was required to adapt PS II preparations to XFEL experiments and to optimize the experimental conditions in terms of sample injection, laser illumination, signal detection and data analysis. The recent paper from Kern *et al.*[11] is a foretaste of how powerful the whole technique can be. We should indeed soon be the spectators of molecular movies shot with an X-ray camera featuring the OEC of PS II as main character, with photons and electrons circulating in concert as the Kok cycle advances.

We can, however, already extract significant mechanistic insight from the structural and spectroscopic data collected on PS II when compared to those collected on synthetic model compounds. The presence of a genuine manganyl, *i.e.* $Mn^{V}\equiv O$ was originally considered as a possible water oxidation intermediate in light of the electrophilic reactivity of such synthetic species, but was then ruled out (at least up to the S_3 state) on the basis of X-ray absorption measurements.[41] The synthesis and characterization of a Mn(V)-oxo complex in a trigonal bispyramidal geometry with a high spin electronic configuration opens up new mechanistic hypotheses. The pre-edge feature and the rather long Mn-O bond (1.68 Å as determined by EXAFS and DFT[44]) found for this complex are consistent with the XAS data collected on PS II up to the S_3 state. Moreover, it has been shown by combined EPR measurements and DFT calculations that the oxido ligand in this complex have a slight amount of radical character. Although a Mn(IV)-oxyl compound (with a full charge on the oxygen ligand) would be quite different (with a longer Mn-O bond), the presence of radical character in the oxido ligand suggests a possible reaction pattern that would be different from a classical 2 electrons nucleophilic-electrophilic attack. The reactivity of this compound has been tested with compounds of the same family, *e.g.* the Mn(III)-OH relative, and showed that single electron transfer (to yield a Mn(IV)-O and a Mn(IV)-OH species) is preferred over a hydroxide-oxo O-O bond formation. These reactivity considerations should, however, not be taken as conclusive as far as the OEC is concerned, since the oxido/hydroxo environment in these complexes is very peculiar, with three hydrogen bonds and bulky groups maintaining it in a protected pocket. Such configuration is obviously not directly comparable to two manganese ions apart from each other by only 3.5-4.0 Å and held together by inorganic interactions in the OEC and by an organic scaffold around it. The potential role of calcium should also be emphasized here, which can act both as a water relay and as the provider of a weak interaction with an unstable Mn-oxo intermediate. The recent XRD structure of the OEC in the S_3 state[11] confirms its essential role in bringing a new water molecule in the active site, either as direct substrate before the O-O bond formation or as the next replacement oxygen after the O-O bond is formed.

In the first part of this chapter, we briefly described two mechanisms for the O-O bond formation that were commonly referred to in the last decade, *i.e.* the "nucleophilic attack" and "radical coupling" mechanisms. In light of the knowledge gathered in the past decade by the whole community working on the OEC and on synthetic model compounds, it appears that these two models can somehow be combined into a unique one. In this model, the oxygens of a terminal and of a bridging Mn-oxo units have a radical character and their geometric and electronic structures are asymmetric. The driving force for the O-O bond formation is yet to be discovered and probably lies in the quick ejection of a proton, very far away from the newly formed peroxo species.

We should stress here the importance of the synthesis and characterization of inorganic model compounds, which have been essential throughout in exploring the potential intermediates that can be proposed along the water oxidation mechanism in the OEC. Notwithstanding the importance of these comparisons, the conclusive evidences on the intermediates present in the

OEC will be provided by the experimental data collected on PS II with time and energy resolution. Although X-ray spectroscopies have proved powerful in describing the geometry and spin state of synthetic manganese complexes or even the protonation state of oxygen ligands, its application to establish the geometric and electronic structure of the OEC along the Kok cycle will require tremendous efforts, not only in terms of data collection (signal-to-noise improvement) but also in their interpretation (theoretical calculations).

References

(1) Kok, B.; Forbush, B.; McGloin, M. ***Photochem. Photobiol.*** **1970**, ***11*** (6), 457-.
(2) Yachandra, V. K.; Sauer, K.; Klein, M. P. ***Chem. Rev.*** **1996**, ***96*** (7), 2927–2950.
(3) Yano, J.; Yachandra, V. ***Chem. Rev.*** **2014**, ***114*** (8, SI), 4175–4205.
(4) Zouni, A.; Witt, H. T.; Kern, J.; Fromme, P.; Krauss, N.; Saenger, W.; Orth, P. ***Nature*** **2001**, ***409*** (6821), 739–743.
(5) Kamiya, N.; Shen, J. R. ***Proc. Natl. Acad. Sci. U. S. A.*** **2003**, ***100*** (1), 98–103.
(6) Ferreira, K. N.; Iverson, T. M.; Maghlaoui, K.; Barber, J.; Iwata, S. ***Science*** **2004**, ***303*** (5665), 1831–1838.
(7) Yano, J.; Kern, J.; Sauer, K.; Latimer, M. J.; Pushkar, Y.; Biesiadka, J.; Loll, B.; Saenger, W.; Messinger, J.; Zouni, A.; Yachandra, V. K. ***Science*** **2006**, ***314*** (5800), 821–825.
(8) Suga, M.; Akita, F.; Hirata, K.; Ueno, G.; Murakami, H.; Nakajima, Y.; Shimizu, T.; Yamashita, K.; Yamamoto, M.; Ago, H.; Shen, J.-R. ***Nature*** **2015**, ***517*** (7532), 99-U265.
(9) Young, I. D.; Ibrahim, M.; Chatterjee, R.; Gul, S.; Fuller, F. D.; Koroidov, S.; Brewster, A. S.; Tran, R.; Alonso-Mori, R.; Kroll, T.; Michels-Clark, T.; Laksmono, H.; Sierra, R. G.; Stan, C. A.; Hussein, R.; Zhang, M.; Douthit, L.; Kubin, M.; de Lichtenberg, C.; Pham, L. V.; Nilsson, H.; Cheah, M. H.; Shevela, D.; Saracini, C.; Bean, M. A.; Seuffert, I.; Sokaras, D.; Weng, T.-C.; Pastor, E.; Weninger, C.; Fransson, T.; Lassalle, L.; Braeuer, P.; Aller, P.; Docker, P. T.; Andi, B.; Orville, A. M.; Glownia, J. M.; Nelson, S.; Sikorski, M.; Zhu, D.; Hunter, M. S.; Lane, T. J.; Aquila, A.; Koglin, J. E.; Robinson, J.; Liang, M.; Boutet, S.; Lyubimov, A. Y.; Uervirojnangkoorn, M.; Moriarty, N. W.; Liebschner, D.; Afonine, P. V; Waterman, D. G.; Evans, G.; Wernet, P.; Dobbek, H.; Weis, W. I.; Brunger, A. T.; Zwart, P. H.; Adams, P. D.; Zouni, A.; Messinger, J.; Bergmann, U.; Sauter, N. K.; Kern, J.; Yachandra, V. K.; Yano, J. ***Nature*** **2016**, ***540*** (7633), 453+.
(10) Cox, N.; Retegan, M.; Neese, F.; Pantazis, D. A.; Boussac, A.; Lubitz, W. ***Science*** **2014**, ***345*** (6198), 804–808.
(11) Kern, J.; Chatterjee, R.; Young, I. D.; Fuller, F. D.; Lassalle, L.; Ibrahim, M.; Gul, S.; Fransson, T.; Brewster, A. S.; Alonso-Mori, R.; Hussein, R.; Zhang, M.; Douthit, L.; de Lichtenberg, C.; Cheah, M. H.; Shevela, D.; Wersig, J.; Seuffert, I.; Sokaras, D.; Pastor, E.; Weninger, C.; Kroll, T.; Sierra, R. G.; Aller, P.; Butryn, A.; Orville, A. M.; Liang, M.; Batyuk, A.; Koglin, J. E.; Carbajo, S.; Boutet, S.; Moriarty, N. W.; Holton, J. M.; Dobbek, H.; Adams, P. D.; Bergmann, U.; Sauter, N. K.; Zouni, A.; Messinger, J.; Yano, J.; Yachandra, V. K. ***Nature*** **2018**.
(12) Siegbahn, P. E. M. ***Acc. Chem. Res.*** **2009**, ***42*** (12), 1871–1880.
(13) Siegbahn, P. E. M. ***Biochim. Biophys. Acta-Bioenergetics*** **2013**, ***1827*** (8–9, SI), 1003–1019.
(14) Messinger, J.; Robblee, J. H.; Bergmann, U.; Fernandez, C.; Glatzel, P.; Visser, H.; Cinco, R. M.; McFarlane, K. L.; Bellacchio, E.; Pizarro, S. A.; Cramer, S. P.; Sauer, K.; Klein, M. P.; Yachandra, V. K. ***J. Am. Chem. Soc.*** **2001**, ***123*** (32), 7804–7820.
(15) Betley, T. A.; Wu, Q.; Van Voorhis, T.; Nocera, D. G. ***Inorg. Chem.*** **2008**, ***47*** (6), 1849–1861.
(16) Cox, N.; Pantazis, D. A.; Neese, F.; Lubitz, W. ***Acc. Chem. Res.*** **2013**, ***46*** (7), 1588–1596.
(17) Umena, Y.; Kawakami, K.; Shen, J.-R.; Kamiya, N. ***Nature*** **2011**, ***473*** (7345), 55-U65.
(18) Suga, M.; Akita, F.; Sugahara, M.; Kubo, M.; Nakajima, Y.; Nakane, T.; Yamashita, K.; Umena, Y.; Nakabayashi, M.; Yamane, T.; Nakano, T.; Suzuki, M.; Masuda, T.; Inoue, S.; Kimura, T.; Nomura, T.; Yonekura, S.; Yu, L.-J.; Sakamoto, T.; Motomura, T.; Chen, J.-H.; Kato, Y.; Noguchi, T.; Tono, K.; Joti, Y.; Kameshima, T.; Hatsui, T.; Nango, E.; Tanaka, R.; Naitow, H.; Matsuura, Y.; Yamashita, A.; Yamamoto, M.; Nureki, O.; Yabashi, M.; Ishikawa, T.; Iwata, S.; Shen, J.-R. ***Nature*** **2017**, ***543*** (7643), 131+.

(19) Yano, J.; Kern, J.; Irrgang, K. D.; Latimer, M. J.; Bergmann, U.; Glatzel, P.; Pushkar, Y.; Biesiadka, J.; Loll, B.; Sauer, K.; Messinger, J.; Zouni, A.; Yachandra, V. K. ***Proc. Natl. Acad. Sci. U. S. A.*** **2005**, ***102*** (34), 12047–12052.

(20) Neutze, R.; Wouts, R.; van der Spoel, D.; Weckert, E.; Hajdu, J. ***Nature*** **2000**, ***406*** (6797), 752–757.

(21) Chapman, H. N.; Fromme, P.; Barty, A.; White, T. A.; Kirian, R. A.; Aquila, A.; Hunter, M. S.; Schulz, J.; DePonte, D. P.; Weierstall, U.; Doak, R. B.; Maia, F. R. N. C.; Martin, A. V; Schlichting, I.; Lomb, L.; Coppola, N.; Shoeman, R. L.; Epp, S. W.; Hartmann, R.; Rolles, D.; Rudenko, A.; Foucar, L.; Kimmel, N.; Weidenspointner, G.; Holl, P.; Liang, M.; Barthelmess, M.; Caleman, C.; Boutet, S.; Bogan, M. J.; Krzywinski, J.; Bostedt, C.; Bajt, S.; Gumprecht, L.; Rudek, B.; Erk, B.; Schmidt, C.; Hoemke, A.; Reich, C.; Pietschner, D.; Strueder, L.; Hauser, G.; Gorke, H.; Ullrich, J.; Herrmann, S.; Schaller, G.; Schopper, F.; Soltau, H.; Kuehnel, K.-U.; Messerschmidt, M.; Bozek, J. D.; Hau-Riege, S. P.; Frank, M.; Hampton, C. Y.; Sierra, R. G.; Starodub, D.; Williams, G. J.; Hajdu, J.; Timneanu, N.; Seibert, M. M.; Andreasson, J.; Rocker, A.; Joensson, O.; Svenda, M.; Stern, S.; Nass, K.; Andritschke, R.; Schroeter, C.-D.; Krasniqi, F.; Bott, M.; Schmidt, K. E.; Wang, X.; Grotjohann, I.; Holton, J. M.; Barends, T. R. M.; Neutze, R.; Marchesini, S.; Fromme, R.; Schorb, S.; Rupp, D.; Adolph, M.; Gorkhover, T.; Andersson, I.; Hirsemann, H.; Potdevin, G.; Graafsma, H.; Nilsson, B.; Spence, J. C. H. ***Nature*** **2011**, ***470*** (7332), 73-U81.

(22) Sierra, R. G.; Laksmono, H.; Kern, J.; Tran, R.; Hattne, J.; Alonso-Mori, R.; Lassalle-Kaiser, B.; Gloeckner, C.; Hellmich, J.; Schafer, D. W.; Echols, N.; Gildea, R. J.; Grosse-Kunstleve, R. W.; Sellberg, J.; McQueen, T. A.; Fry, A. R.; Messerschmidt, M. M.; Miahnahri, A.; Seibert, M. M.; Hampton, C. Y.; Starodub, D.; Loh, N. D.; Sokaras, D.; Weng, T.-C.; Zwart, P. H.; Glatzel, P.; Milathianaki, D.; White, W. E.; Adams, P. D.; Williams, G. J.; Boutet, S.; Zouni, A.; Messinger, J.; Sauter, N. K.; Bergmann, U.; Yano, J.; Yachandra, V. K.; Bogan, M. J. ***Acta Crystallogr. Sect. D-Biological Crystallogr.*** **2012**, ***68*** (11), 1584–1587.

(23) Alonso-Mori, R.; Kern, J.; Sokaras, D.; Weng, T.-C.; Nordlund, D.; Tran, R.; Montanez, P.; Delor, J.; Yachandra, V. K.; Yano, J.; Bergmann, U. ***Rev. Sci. Instrum.*** **2012**, ***83*** (7).

(24) Hattne, J.; Echols, N.; Tran, R.; Kern, J.; Gildea, R. J.; Brewster, A. S.; Alonso-Mori, R.; Gloeckner, C.; Hellmich, J.; Laksmono, H.; Sierra, R. G.; Lassalle-Kaiser, B.; Lampe, A.; Han, G.; Gul, S.; DiFiore, D.; Milathianaki, D.; Fry, A. R.; Miahnahri, A.; White, W. E.; Schafer, D. W.; Seibert, M. M.; Koglin, J. E.; Sokaras, D.; Weng, T.-C.; Sellberg, J.; Latimers, M. J.; Glatzel, P.; Zwart, P. H.; Grosse-Kunstleve, R. W.; Bogan, M. J.; Messerschmidt, M.; Williams, G. J.; Boutet, S.; Messinger, J.; Zouni, A.; Yano, J.; Bergmann, U.; Yachandra, V. K.; Adams, P. D.; Sauter, N. K. ***Nat. Methods*** **2014**, ***11*** (5), 545–548.

(25) Alonso-Mori, R.; Kern, J.; Gildea, R. J.; Sokaras, D.; Weng, T.-C.; Lassalle-Kaiser, B.; Tran, R.; Hattne, J.; Laksmono, H.; Hellmich, J.; Gloeckner, C.; Echols, N.; Sierra, R. G.; Schafer, D. W.; Sellberg, J.; Kenney, C.; Herbst, R.; Pines, J.; Hart, P.; Herrmann, S.; Grosse-Kunstleve, R. W.; Latimer, M. J.; Fry, A. R.; Messerschmidt, M. M.; Miahnahri, A.; Seibert, M. M.; Zwart, P. H.; White, W. E.; Adams, P. D.; Bogan, M. J.; Boutet, S.; Williams, G. J.; Zouni, A.; Messinger, J.; Glatzel, P.; Sauter, N. K.; Yachandra, V. K.; Yano, J.; Bergmann, U. ***Proc. Natl. Acad. Sci. U. S. A.*** **2012**, ***109*** (47), 19103–19107.

(26) Kern, J.; Alonso-Mori, R.; Hellmich, J.; Tran, R.; Hattne, J.; Laksmono, H.; Gloeckner, C.; Echols, N.; Sierra, R. G.; Sellberg, J.; Lassalle-Kaiser, B.; Gildea, R. J.; Glatzel, P.; Grosse-Kunstleve, R. W.; Latimer, M. J.; McQueen, T. A.; DiFiore, D.; Fry, A. R.; Messerschmidt, M.; Miahnahri, A.; Schafer, D. W.; Seibert, M. M.; Sokaras, D.; Weng, T.-C.; Zwart, P. H.; White, W. E.; Adams, P. D.; Bogan, M. J.; Boutet, S.; Williams, G. J.; Messinger, J.; Sauter, N. K.; Zouni, A.; Bergmann, U.; Yano, J.; Yachandra, V. K. ***Proc. Natl. Acad. Sci. U. S. A.*** **2012**, ***109*** (25), 9721–9726.

(27) Fuller, F. D.; Gul, S.; Chatterjee, R.; Burgie, E. S.; Young, I. D.; Lebrette, H.; Srinivas, V.; Brewster, A. S.; Michels-Clark, T.; Clinger, J. A.; Andi, B.; Ibrahim, M.; Pastor, E.; de Lichtenberg, C.; Hussein, R.; Pollock, C. J.; Zhang, M.; Stan, C. A.; Kroll, T.; Fransson, T.; Weninger, C.; Kubin, M.; Aller, P.; Lassalle, L.; Braeuer, P.; Miller, M. D.; Amin, M.; Koroidov, S.; Roessler, C. G.; Allaire, M.; Sierra, R. G.; Docker, P. T.; Glownia, J. M.; Nelson, S.; Koglin, J. E.; Zhu, D.; Chollet, M.; Song, S.; Lemke, H.; Liang, M.; Sokaras, D.; Alonso-Mori, R.; Zouni, A.; Messinger, J.; Bergmann, U.; Boal, A. K.; Bollinger Jr., J. M.; Krebs, C.; Hoegbom, M.; Phillips Jr., G. N.; Vierstra, R. D.; Sauter, N. K.; Orville, A. M.; Kern, J.; Yachandra, V. K.; Yano, J. ***Nat. Methods*** **2017**, ***14*** (4), 443+.

(28) Kern, J.; Alonso-Mori, R.; Tran, R.; Hattne, J.; Gildea, R. J.; Echols, N.; Gloeckner, C.; Hellmich, J.; Laksmono, H.; Sierra, R. G.; Lassalle-Kaiser, B.; Koroidov, S.; Lampe, A.; Han, G.; Gul, S.; DiFiore, D.; Milathianaki, D.; Fry, A. R.; Miahnahri, A.; Schafer, D. W.; Messerschmidt, M.; Seibert, M. M.; Koglin, J. E.; Sokaras, D.; Weng, T.-C.; Sellberg, J.; Latimer, M. J.; Grosse-Kunstleve, R. W.; Zwart, P. H.; White, W. E.; Glatzel, P.; Adams, P. D.; Bogan, M. J.; Williams, G. J.; Boutet, S.; Messinger, J.;

Zouni, A.; Sauter, N. K.; Yachandra, V. K.; Bergmann, U.; Yano, J. ***Science*** **2013**, ***340*** (6131), 491–495.

(29) Kern, J.; Tran, R.; Alonso-Mori, R.; Koroidov, S.; Echols, N.; Hattne, J.; Ibrahim, M.; Gul, S.; Laksmono, H.; Sierra, R. G.; Gildea, R. J.; Han, G.; Hellmich, J.; Lassalle-Kaiser, B.; Chatterjee, R.; Brewster, A. S.; Stan, C. A.; Gloeckner, C.; Lampe, A.; DiFiore, D.; Milathianaki, D.; Fry, A. R.; Seibert, M. M.; Koglin, J. E.; Gallo, E.; Uhlig, J.; Sokaras, D.; Weng, T.-C.; Zwart, P. H.; Skinner, D. E.; Bogan, M. J.; Messerschmidt, M.; Glatzel, P.; Williams, G. J.; Boutet, S.; Adams, P. D.; Zouni, A.; Messinger, J.; Sauter, N. K.; Bergmann, U.; Yano, J.; Yachandra, V. K. ***Nat. Commun.*** **2014**, ***5***.

(30) Mitzner, R.; Rehanek, J.; Kern, J.; Gul, S.; Hattne, J.; Taguchi, T.; Alonso-Mori, R.; Tran, R.; Weniger, C.; Schroeder, H.; Quevedo, W.; Laksmono, H.; Sierra, R. G.; Han, G.; Lassalle-Kaiser, B.; Koroidov, S.; Kubicek, K.; Schreck, S.; Kunnus, K.; Brzhezinskaya, M.; Firsov, A.; Minitti, M. P.; Turner, J. J.; Moeller, S.; Sauter, N. K.; Bogan, M. J.; Nordlund, D.; Schlotter, W. F.; Messinger, J.; Borovik, A.; Techert, S.; de Groot, F. M. F.; Foehlisch, A.; Erko, A.; Bergmann, U.; Yachandra, V. K.; Wernet, P.; Yano, J. ***J. Phys. Chem. Lett.*** **2013**, ***4*** (21), 3641–3647.

(31) Kubin, M.; Kern, J.; Gul, S.; Kroll, T.; Chatterjee, R.; Loechel, H.; Fuller, F. D.; Sierra, R. G.; Quevedo, W.; Weniger, C.; Rehanek, J.; Firsov, A.; Laksmono, H.; Weninger, C.; Alonso-Mori, R.; Nordlund, D. L.; Lassalle-Kaiser, B.; Glownia, J. M.; Krzywinski, J.; Moeller, S.; Turner, J. J.; Minitti, M. P.; Dakovski, G. L.; Koroidov, S.; Kawde, A.; Kanady, J. S.; Tsui, E. Y.; Suseno, S.; Han, Z.; Hill, E.; Taguchi, T.; Borovik, A. S.; Agapie, T.; Messinger, J.; Erko, A.; Foehlisch, A.; Bergmann, U.; Mitzner, R.; Yachandra, V. K.; Yano, J.; Wernet, P. ***Struct. Dyn.*** **2017**, ***4*** (5).

(32) Lassalle-Kaiser, B. ***PhD Thesis, Univ. Paris-Sud*** **2008**.

(33) El Ghachtouli, S.; Lassalle-Kaiser, B.; Dorlet, P.; Guillot, R.; Anxolabehere-Mallart, E.; Costentin, C.; Aukauloo, A. ***Energy Environ. Sci.*** **2011**, ***4*** (6), 2041–2044.

(34) El Ghachtouli, S.; Guillot, R.; Aukauloo, A.; Dorlet, P.; Anxolabehere-Mallart, E.; Costentin, C. ***Inorg. Chem.*** **2012**, ***51*** (6), 3603–3612.

(35) El Ghachtouli, S.; Ching, H. Y. V.; Lassalle-Kaiser, B.; Guillot, R.; Leto, D. F.; Chattopadhyay, S.; Jackson, T. A.; Dorlet, P.; Anxolabehere-Mallart, E. ***Chem. Commun.*** **2013**, ***49*** (50), 5696–5698.

(36) Cook, S. A.; Borovik, A. S. ***Acc. Chem. Res.*** **2015**, ***48*** (8), 2407–2414.

(37) Borovik, A. S. ***Acc. Chem. Res.*** **2005**, ***38*** (1), 54–61.

(38) MacBeth, C. E.; Gupta, R.; Mitchell-Koch, K. R.; Young, V. G.; Lushington, G. H.; Thompson, W. H.; Hendrich, M. P.; Borovik, A. S. ***J. Am. Chem. Soc.*** **2004**, ***126*** (8), 2556–2567.

(39) Collins, T. J.; Gordonwylie, S. W. ***J. Am. Chem. Soc.*** **1989**, ***111*** (12), 4511–4513.

(40) Collins, T. J.; Powell, R. D.; Slebodnick, C.; Uffelman, E. S. ***J. Am. Chem. Soc.*** **1990**, ***112*** (2), 899–901.

(41) Weng, T. C.; Hsieh, W. Y.; Uffelman, E. S.; Gordon-Wylie, S. W.; Collins, T. J.; Pecoraro, V. L.; Penner-Hahn, J. E. ***J. Am. Chem. Soc.*** **2004**, ***126*** (26), 8070–8071.

(42) Parsell, T. H.; Behan, R. K.; Green, M. T.; Hendrich, M. P.; Borovik, S. ***J. Am. Chem. Soc.*** **2006**, ***128*** (27), 8728–8729.

(43) Taguchi, T.; Stone, K. L.; Gupta, R.; Kaiser-Lassalle, B.; Yano, J.; Hendrich, M. P.; Borovik, A. S. ***Chem. Sci.*** **2014**, ***5*** (8), 3064–3071.

(44) Gupta, R.; Taguchi, T.; Lassalle-Kaiser, B.; Bominaar, E. L.; Yano, J.; Hendrich, M. P.; Borovik, A. S. ***Proc. Natl. Acad. Sci. U. S. A.*** **2015**, ***112*** (17), 5319–5324.

(45) Taguchi, T.; Gupta, R.; Lassalle-Kaiser, B.; Boyce, D. W.; Yachandra, V. K.; Tolman, W. B.; Yano, J.; Hendrich, M. P.; Borovik, A. S. ***J. Am. Chem. Soc.*** **2012**, ***134*** (4), 1996–1999.

(46) Lassalle-Kaiser, B.; Hureau, C.; Pantazis, D. A.; Pushkar, Y.; Guillot, R.; Yachandra, V. K.; Yano, J.; Neese, F.; Anxolabehere-Mallart, E. ***Energy Environ. Sci.*** **2010**, ***3*** (7), 924–938.

(47) Yano, J.; Robblee, J.; Pushkar, Y.; Marcus, M. A.; Bendix, J.; Workman, J. M.; Collins, T. J.; Solomon, E. I.; George, S. D.; Yachandra, V. K. ***J. Am. Chem. Soc.*** **2007**, ***129*** (43), 12989–13000.

(48) Glatzel, P.; Bergmann, U. ***Coord. Chem. Rev.*** **2005**, ***249*** (1–2), 65–95.

(49) Wang, X.; Randall, C. R.; Peng, G.; Cramer, S. P. ***Chem. Phys. Lett.*** **1995**, ***243*** (5–6), 469–473.

(50) Britt, R. D.; Suess, D. L. M.; Stich, T. A. ***Proc. Natl. Acad. Sci. U. S. A.*** **2015**, ***112*** (17), 5265–5266.

(51) Mukhopadhyay, S.; Mandal, S. K.; Bhaduri, S.; Armstrong, W. H. ***Chem. Rev.*** **2004**, ***104*** (9), 3981–4026.

(52) Baldwin, M. J.; Stemmler, T. L.; Riggs-Gelasco, P. J.; Kirk, M. L.; Penner-H; Ahn, J. E.; Pecoraro, V. L. ***J. Am. Chem. Soc.*** **1994**, ***116*** (25), 11349–11356.

(53) Krewald, V.; Lassalle-Kaiser, B.; Boron III, T. T.; Pollock, C. J.; Kern, J.; Beckwith, M. A.; Yachandra, V. K.; Pecoraro, V. L.; Yano, J.; Neese, F.; DeBeer, S. ***Inorg. Chem.*** **2013**, ***52*** (22), 12904–12914.

(54) Lassalle-Kaiser, B.; Boron III, T. T.; Krewald, V.; Kern, J.; Beckwith, M. A.; Delgado-Jaime, M. U.;

Schroeder, H.; Alonso-Mori, R.; Nordlund, D.; Weng, T.-C.; Sokaras, D.; Neese, F.; Bergmann, U.; Yachandra, V. K.; DeBeer, S.; Pecoraro, V. L.; Yano, J. ***Inorg. Chem.*** **2013**, ***52*** (22), 12915–12922.

(55) Pushkar, Y.; Long, X.; Glatzel, P.; Brudvig, G. W.; Dismukes, G. C.; Collins, T. J.; Yachandra, V. K.; Yano, J.; Bergmann, U. ***Angew. Chemie Int. Ed.*** **2010**, ***49*** (4), 800–803.

(56) Smolentsev, G.; Soldatov, A. V; Messinger, J.; Merz, K.; Weyhermueller, T.; Bergmann, U.; Pushkar, Y.; Yano, J.; Yachandra, V. K.; Glatzel, P. ***J. Am. Chem. Soc.*** **2009**, ***131*** (36), 13161–13167.

(57) Lancaster, K. M.; Roemelt, M.; Ettenhuber, P.; Hu, Y.; Ribbe, M. W.; Neese, F.; Bergmann, U.; DeBeer, S. ***Science*** **2011**, ***334*** (6058), 974–977.

(58) Pollock, C. J.; DeBeer, S. ***Acc. Chem. Res.*** **2015**, ***48*** (11), 2967–2975.

(59) Safonova, O. V; Florea, M.; Bilde, J.; Delichere, P.; Millet, J. M. M. ***J. Catal.*** **2009**, ***268*** (1), 156–164.

(60) Safonov, V. A.; Vykhodtseva, L. N.; Polukarov, Y. M.; Safonova, O. V; Smolentsev, G.; Sikora, M.; Eeckhout, S. G.; Glatzel, P. ***J. Phys. Chem. B*** **2006**, ***110*** (46), 23192–23196.

(61) Rutherford, A. W.; Boussac, A. ***Science*** **2004**, ***303*** (5665), 1782–1784.

Chapter 2 : *Operando* studies of electrocatalytic systems using X-ray spectroscopies

2.1 Experimental considerations

In situ or *operando* X-ray experiments have been performed for several decades, with the intent of studying interface phenomena such as those found in heterogeneous catalysis,[1] fuel cells,[2] or batteries.[3] Concerning the coupling of X-ray techniques with electrochemical systems, the main challenge lied so far in the design of the cell and its components. Recent experiments have taken advantage of the commercial availability of very thin (tens of nanometer) silicon nitride membranes. These membranes are almost transparent to X-rays while having very good mechanical and chemical resistance. They can, moreover, be coated with thin films of conductive materials that are suited to the experiment in terms of chemical compatibility, reactivity, or X-ray absorption. Certain materials can even play both the role of a separating membrane and of an electrode, such as glassy carbon films, boron-doped diamond or thin metallic foils. The balance between conductivity, mechanical and chemical resistance and thickness is not always easy to match, and it gets more difficult as the photon energy decreases. From the data collection point of view, the vast majority of experiments consist in applying a constant potential between the reference and working electrodes for a time long enough to record XAS spectra with a sufficient signal to noise (S/N) ratio. Figure 2-1 shows a typical example of an electrochemical cell that has been used by our group and others for *in situ/operando* characterization of electrochemical materials with hard X-ray techniques. To avoid the effects of bubbles that form during the OER and HER reactions as well as to avoid interference of X-rays with electrolyte layers, we used a setup in which the back side of the X-ray transparent window faces the incident X-rays and the conductive, front side of the window with the catalyst faces the electrolyte. The window consists of Si_3N_4 or glassy carbon, with conductive layers, such as ITO (Indium-doped Tin Oxide), FTO (Fluorine-doped Tin Oxide), or Au being used as the working electrode (WE). The counter electrode (CE) is isolated from the main compartment and the reference electrode (RE) is placed close to the WE. In the experimental configuration shown in figure 2-1, X-rays can penetrate into both the catalysts and the electrolyte. All of the electrocatalysts presented in the next section are, however, porous materials that consist of electrolyte-permeable structures. Therefore, spectroscopic changes under applied

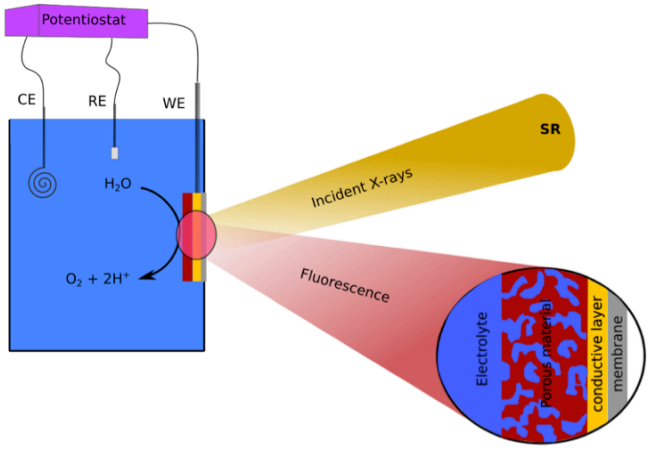

Figure 2-1. Schematic representation of an *in situ/operando* X-ray spectroelectrochemical cell. CE, RE and WE stand for counter, reference and working electrodes, respectively. SR stands for synchrotron radiation.

potentials are noticeable, without requiring more surface-sensitive methods. This was demonstrated, for example, by the study of a manganese oxide catalyst with two different thicknesses (100 and 200 nm). While the electrocatalytic current scaled linearly with the thickness of the material, the spectroscopic signature remained identical. This indicated that the entire thickness of the material was active, and not only the topmost layer.[4] Similarly, Klingan *et al.* showed that the bulk region of CoO_x-based catalysts is active for oxygen evolution owing to the formation of a highly accessible $Co^{III}O(OH)$ layered structure, in which water and electrolyte can efficiently diffuse and intercalate between the different layers.[5]

The work presented in the next sections has been performed for the main part during our post-doctoral stay in the group of Drs. Junko Yano and Vittal Yachandra at the Physical Bioscience Division of the Lawrence Berkeley National Laboratory, but also as a scientist at SOLEIL. The X-ray based experiments were performed at the Stanford Synchrotron Radiation Laboratory (SSRL), at the Advanced Light Source (ALS) or at SOLEIL. This chapter is divided somewhat arbitrarily in two parts describing the oxygen evolving and hydrogen evolving systems we have studied using *in situ* and/or *operando* X-ray techniques, and a third one discussing the perspectives of such experiments.

2.2 Oxygen-evolving systems

During the last decade, while most of the artificial photosynthesis field was focused on mimicking as accurately as possible the active sites of the Oxygen Evolving Center or Hydrogenases, Dr. M. Kanan and Prof. D. G. Nocera published an article that described the electrocatalytic oxidation of water into dioxygen by a cobalt oxide catalyst under benign conditions (pH 7 phosphate buffer).[6] Despite the simplicity of the materials and concepts used, this study had a huge impact on the field. It showed that simple, non-noble transition metal oxides are OER-active and extremely robust towards oxidation (which is a truism), while being very simple and cheap to prepare. Over a few years, most of the field had abandoned molecular water oxidation (except for ruthenium and iridium-based chemistry) and switched to transition metal oxides. In this part, we will describe our contribution to understand such oxide-based systems using *in situ* and *operando* X-ray spectroscopies.

2.2.1 The case of an OER-active nickel borate thin film

In the continuation of a collaboration with the group of Prof. D. G. Nocera at the Massachussets Institute of Technology (now at Harvard University) that focused on the study of an OER-active cobalt-based oxide,[7] we performed similar studies[8] on a related nickel-based system described by the same group.[9] This system consists in a thin film (*ca.* 7 nm), electrodeposited from an $Ni(NO_3)_2$ aqueous borate buffer at pH 9.2. An interesting feature of these films as compared to their cobalt counterparts is the existence of an activation process that turns the material into its most active form. The OER activity of the film indeed shows a first phase, which is not so efficient, and a second phase which occurs after about one hour, with higher efficiency. We have therefore used X-ray absorption spectroscopy at the nickel K-edge to determine the structure of this material just after it is deposited, after its activation and under catalytic conditions. Figure 2-2A shows the consecutive cyclic voltamograms recorded

on a $NiNO_3$ solution in borate buffer at pH = 9.2. The anodic wave at Ep=0.78 V *vs*. SCE corresponds to the oxidation of the deposited $Ni(OH)_2$ film into NiOOH. The increase in intensity observed as a function of scan number is due to the increased amount of material deposited on the electrode after each anodic scan. These voltamograms can be divided into three regions and XANES spectra at the Ni K-edge were recorded for each of them: under resting, pre-catalytic and catalytic states (green, purple and red regions, respectively, on figure 2-2 A). The spectra recorded are shown on figure 2-2 B, together with $Ni(OH)_2$ and NiOOH reference oxides. From their rising edge positions, it can be clearly seen that the resting state of the electrodeposited nickel film (which will be named NiBi from now on) is comparable to Ni(II) hydroxide, while the pre-catalytic and catalytic states are more oxidized, as is the NiOOH reference spectrum. It should be noted that NiOOH has β and γ phases, which are both lamellar. The β phase only has Ni(III) ions, while the γ one has both Ni(III) and Ni(IV) ions, with an average oxidation state of *ca*. +3.6. This overall higher oxidation state is correlated to the insertion of cations between the nickel oxide sheets. In the case of the NiBi film, the pre-catalytic state, which is obtained by applying a constant potential just beyond the Ni(II) to Ni(III) oxidation wave at E_p=0.8 V *vs*. SCE, shows a clear shift in its rising edge position (*ca*. 2 eV). This indicates the formation of the β phase of NiOOH, which is confirmed by EXAFS measurements and fittings (data not shown here). The catalytic form of the NiBi film is obtained by applying a constant potential equal or superior to 1.0 V *vs*. SCE, which corresponds to OER conditions. In this case, the rising edge position is shifted to even higher values (*ca*. + 1.3 eV with respect to the pre-catalytic form) and is also confirmed by the shortening of a fraction of the Ni-O bonds (from 2.10 to 1.90 Å) as determined by EXAFS measurements (data not shown here). EXAFS measurements could only be measured on the catalytic state, the pre-catalytic one being slowly converted into the catalytic form since the potential required to generate it is at the foot of the catalytic process. The analysis of these data showed that i) the lamellar structure of γ NiOOH is the active species during OER and ii) the smallest ordered domain size is *ca*. 2 nm (40 atoms). It also showed to our disguise that the energy resolution provided by most hard X-ray beamlines is not sufficient to observe the slight energy shift expected for the presence of transient Ni(IV) catalytic species.

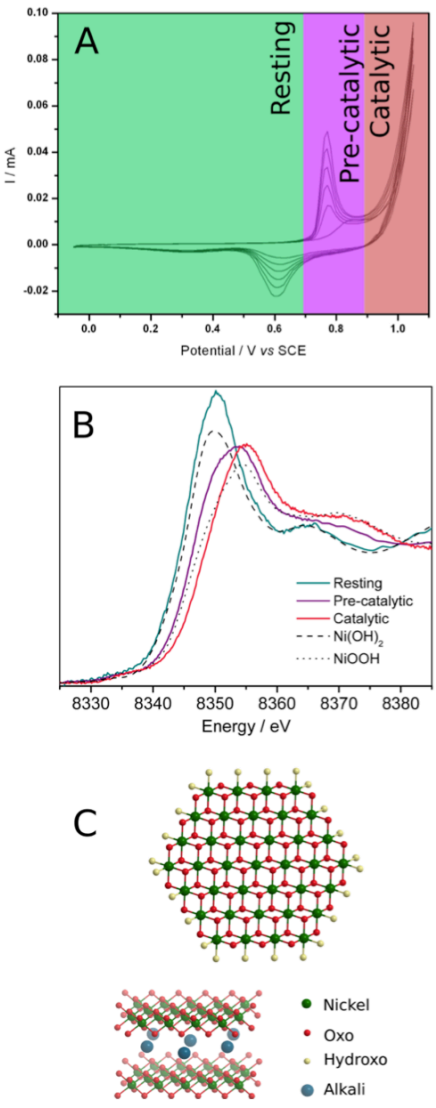

Figure 2-2. Consecutive cyclic voltamograms recorded during the electrodeposition of an NiBi film from an $NiNO_3$/KBi solution (A), XANES spectra at the Ni K-edge of the NiBi film under different in *situ/operando* conditions and of reference compounds (B) and schematic representation of the γ NiOOH phase as a 2 nm disk (top) or a stack of two sheets (bottom) (C).

2.2.2 The case of a bifunctional ORR/OER-active manganese oxide thin film

Following the approach developed by Nocera and Kanan on the use of transition metal oxides produced with low cost and simple techniques, Pr. Thomas Jaramillo and Yelena Gorlin published an article in 2010 about the preparation of an amorphous manganese oxide film that was active both for the water oxidation and dioxygen reduction reactions.[10] This material, prepared by annealing of a manganese oxide thin film deposited from an aqueous solution of a manganese salt, was described as amorphous and lacked detailed structural

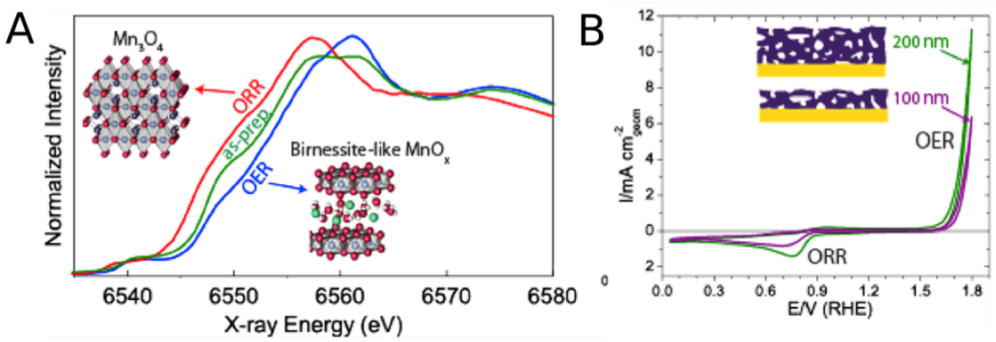

Figure 2-3. XANES spectra of the MnO_x material 'as prepared' (green), under ORR (red) and OER (blue) conditions (A), and cyclic voltamogramms of 100 and 200 nm thick film, showing the linearity of the electrochemical response as a function of thickness (B).

information. We therefore applied *in situ/operando* XAS to this material in order to better describe it and understand its behavior under catalytic conditions.[4] Figure 2-3 shows the XANES spectra recorded on the MnO_x material 'as prepared', under ORR (0.7 V *vs.* RHE) and under OER conditions (1.8 V *vs.* RHE). It appears clearly from these curves that the valence of manganese but also the structure of the starting material is modified under ORR or OER conditions. Analyzing these spectra in more details by comparing them with reference compounds and correlating them with EXAFS fittings, we described the material as a layered birnessite phase under OER conditions, which converts into Mn_3O_4 under ORR conditions. This conversion is not topotactic and should therefore not be favored, but the small size of the domains involved in the conversion (no diffraction was observed and the largest domain size was estimated by EXAFS fittings to be *ca.* 2 nm) may explain this rapid conversion.

This material was further optimized by the group of Jaramillo, by the inclusion of nickel in the oxide matrix. Nickel and manganese oxides being known as good catalysts for OER and ORR, respectively, they surmised that a combination of both metals could combine their respective properties. This is indeed what happened in the $NiMnO_x$ material that they prepared, which has enhanced ORR and OER properties as compared to regular NiO_x and MnO_x, respectively. This material was in turn studied by us, using X-ray absorption and emission spectroscopies.[11] In particular, we used the dispersive X-ray emission spectrometer developed by R. Alonso-Mori and U. Bergmann[12] (mentioned in the previous chapter) in a modified configuration (using 12 Si440 crystals to collect the manganese Kβ fluorescence and 4 Si551 crystals to collect the nickel Kβ fluorescence, see figure 2-4A) to probe both the nickel and manganese elements at the same time. Thanks to this spectrometer configuration, we

measured the energy of the Kβ fluorescence line from both the manganese and nickel ions as a function of applied potential. Using integrated absolute difference (IAD) analysis (see figure 2-4B), we could show that, when the electrochemical potential is increased, the mean oxidation state of manganese first increases from Mn(III) to Mn(IV) while the oxidation state of nickel starts to increase (from Ni(II) to Ni(III)) only when the oxidation state of manganese reaches a plateau. This behavior points to different roles for the two ions, manganese acting more like a reservoir for oxidizing equivalents, while nickel would be the actual active site. This study was, as far as we know, the first example of a dispersive spectrometer used to monitor the oxidation state of two different elements at the same time. Although electrochemical potentials were applied for rather long periods of time in this particular experiment (30 to 120 minutes), the setup used shows great promise for application in time-resolved electrochemistry.

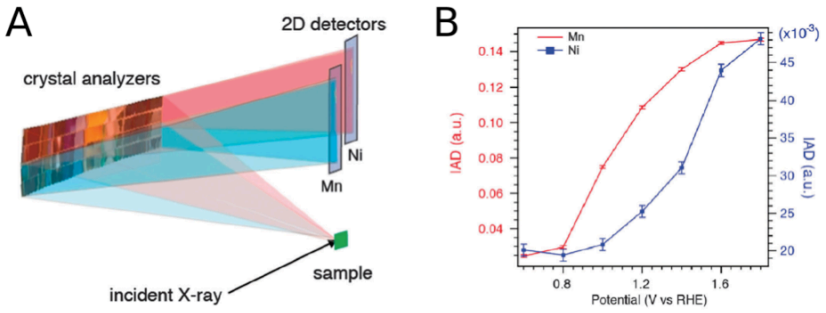

Figure 2-4. Dispersive X-ray emission spectrometer in Von Hamos geometry showing the two sets of crystals and the two detectors to collect both the Mn and Ni Kβ emission lines (A). Integrated Absolute Difference measured on the Kβ emission lines for both the manganese and nickel ions as a function of applied potential (B).

The examples described in this paragraph show that *operando* XAS is critical in determining the structure of oxide-based OER electrocatalysts under functioning conditions. We are currently pursuing similar work on oxides that are photocatalytically active for the OER[13] as well as on other classes of materials such as nickel borides. The study of these materials by *operando* XAS and *operando* TEM has been funded by an ANR grant in collaboration with the groups of Dr. David Portehault (CNRS/Sorbonne Université) and Pr. Ovidiu Ersen (University of Strasbourg).

2.3 Hydrogen-evolving systems

2.3.1 Transition metal sulfides

Transition metal sulfides have been studied for several decades for their catalytic properties, in particular for hydrodesulfurization reactions,[14,15] which are used to remove the sulfur compounds responsible for the poisoning of catalysts at the exhausts of vehicles. This class of compounds were shown to be active for the hydrogen evolving reaction, with a particularly high efficiency for molybdenum sulfides.[14,16] Starting from the years 2010 and the seminal work of Jaramillo and Chorkendorf,[17] a wide variety of molybdenum sulfide-based

compounds were prepared and studied for their HER activity.[18,19] In collaboration with research groups developing HER-active molybdenum sulfide catalysts, we have used X-ray spectroscopy to determine their structure, both under *ex situ* and *operando* conditions.
The first system we studied was developed by the group of Pr. A. Paul Alivisatos at the University of California in Berkeley. It consisted in MoS_x-coated CdS nanorods with a CdSe seed, which were able to perform light-induced HER in water and in the presence of a sacrificial electron donor.[20] The MoS_x layer deposited on the outer shell of the particles was obtained by calcination of a molecular precursor and the structure of the final product was hardly identifiable save for X-ray absorption spectroscopy. We therefore measured the Mo K-edge EXAFS spectra and performed the corresponding fits. By comparing our data and analysis to previous work on the structure of crystalline and amorphous MoS_x materials,[21–23] we showed that the molecular structure of the initial material is not retained after the nanorods decoration, and that the active material is a layer of amorphous MoS_3.

The second system we studied was developed in the team of Pr. Xile Hu at the Ecole Polytechnique Fédérale de Lausanne (EPFL).[24] Inspiring from the simple electrochemical deposition method proposed by Kanan and Nocera for OER-active metal oxides, the Hu group applied this method to the deposition of MoS_x materials from an aqueous solution of $(NH_4)_2MoS_4$. The structure of this material was, however, difficult to unambiguously determine using electrochemical or *ex situ* surface techniques such as XPS. We therefore applied X-ray absorption spectroscopy at the molybdenum K and L-edges and at the sulfur K-edge on this material, under *in situ* and *operando* conditions.[25] Interestingly, the Mo K-edge data did not provide much electronic information, since the XANES spectroscopic features do not present any trend with a clear relationship to the molybdenum oxidation state, which is due to the non-innocent nature of the sulfur ligands. The EXAFS data were, however, very informative and allowed us determining the presence or absence of bridging disulfide units under acidic conditions and under HER operation. Sulfur K-edge and Mo $L_{2,3}$-edges were collected at the 4.3 beamline of SSRL, with a custom-designed electrochemical cell accommodating a helium blanket on the incoming and outgoing X-ray beam path, so as to maximize the count rate. Surprisingly, the data obtained under *operando* conditions (figure 2-5) show that, as the cathodic potential is increased, the molybdenum centers are reduced, while the sulfur ones are oxidized. This behavior was explained by the fact that these measurement describe the state formed just prior to the rate-limiting step, which we described as a molybdenum(III) ion with a terminal disulfide unit bound to it. The mechanism we proposed based on these data is shown on figure 2-5E and is very similar to what has been proposed so far for crystalline MoS_2.[17] It is, however, the first demonstration that amorphous MoS_x materials perform the HER following a mechanism that is ligand-based and involves terminal disulfide units, with a low-valency Mo ion. It is worth mentioning that, after this study was published, a few research groups proposed that other mechanisms, involving highly-valent molybdenum ions such as Mo(V) were occurring in MoS_4 HER-active thin film deposited on gold,[26] or in MoS_2 amorphous nanoparticles.[27] Although such a proposal seems reasonable in the case of MoS_4 thin films on gold (were terminal sulfides are the actual locus of catalysis), it is much more questionable in the case of MoS_2 nanoparticles, especially given that the proposed mechanism involves hydride species with molybdenum in a high oxidation state. We are currently working on *operando* measurements applied to several MoS_x materials in order to disentangle these mechanistic issues and propose a final mechanism for HER-active molybdenum sulfide electrocatalysts.

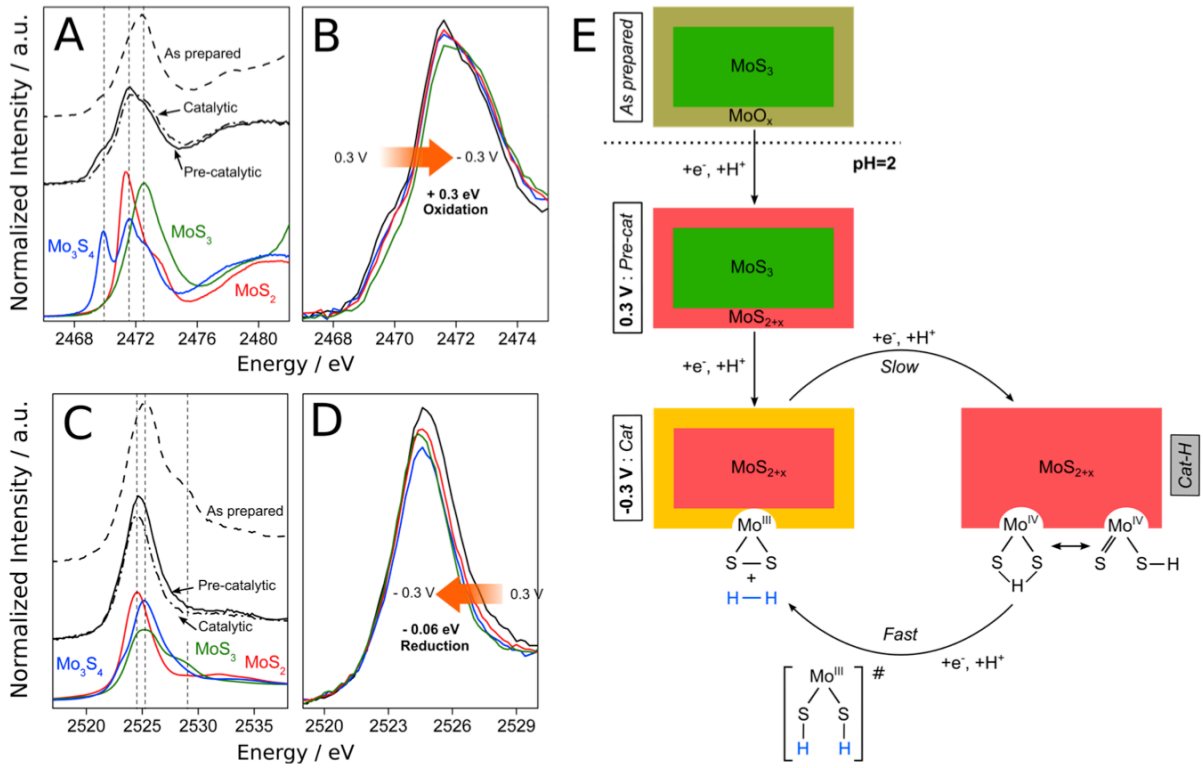

Figure 2-5. Sulfur K-edge (A, B) and Mo L_3-edge (C, D) absorption spectra of the MoS_x material as prepared, under pre-catalytic and catalytic conditions and of reference compounds. The right panels (B, D) show the progressive evolution of the edge position as a function of applied potential. The scheme on the right shows the proposed structure of the MoS_x material under as prepared, pre-catalytic and catalytic conditions. The Cat-H species in grey is only putative.

We are expanding this work on transition metal sulfides through collaborations with the teams of Dr. Marion Giraud at the Université Paris-Diderot (working on iron and cobalt sulfides) and of Dr. Sophie Carenco at the CNRS/Sorbonne Université (working on molybdenum oxysulfides).

2.3.2 Case of a metallic nanocatalyst obtained from a molecular precursor

As mentioned in our general introduction, Artificial Photosynthesis has its roots in the biomimetic synthetic chemistry that tried to reproduce enzyme's actives sites in order to perform natural reactions such as the water oxidation reaction of Photosynthesis or the reduction/oxidation of protons/hydrogen performed by hydrogenases. Although the compounds that reproduced enzyme's active sites most faithfully were not the most active ones, the molecular coordination chemistry developed inspired other architectures for the OER or HER. OER-active systems were rapidly abandoned when it appeared clearly that the organic ligands binding the transition metals were not robust enough given the harsh oxidizing conditions required to form an O-O bond. On the contrary, HER-active molecular systems have been thriving for a good decade until now. One system that was extensively studied was based on glyoxime ligands coordinating a cobalt ion, the so-called cobaloxime family. This molecule was first synthesized by Espenson in the 70's[28] and later revisited by many groups worldwide.[29] In 2012, Fournier *et al.* showed that the HER activity attributed to

cobaloximes was actually coming from nanoparticles deposited on the electrode upon addition of acid and the application of an electrochemical potential.[30] The nature of these nanoparticles was not clearly established and we therefore collaborated with the team of Dr. Elodie Anxolabéhère-Mallart and Pr. Marc Robert at the Laboratoire d'Electrochimie Moléculaire at the Université Paris Diderot to apply *in situ* and *operando* X-ray spectroscopy to determine what material was responsible for the actual catalysis.

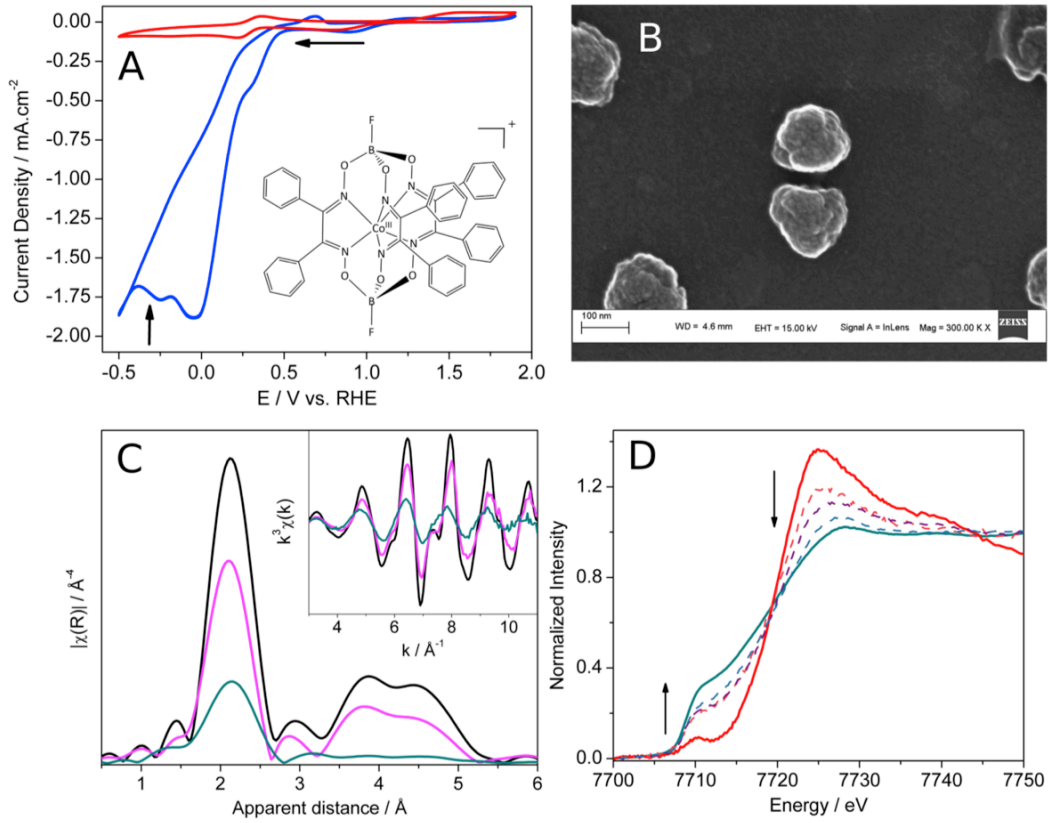

Figure 2-6. Cyclic voltamograms of the $[Co(dpg)_3(BF)_2]^+$ complex in acetonitrile in the absence (red) and presence (blue) of acid, together with its molecular structure (A). Electron micrograph of the nanoparticles formed after applying a constant potential at -0.35 V *vs.* RHE on a 1 mM solution of $[Co(dpg)_3(BF)_2]^+$ in acetonitrile (B). Co K-edge EXAFS Fourier transforms and k-space (insert) of the amorphous Co nanoparticles deposited (cyan) of *fcc*-Co (magenta) and of *hcp*-Co (black) (C). Co K-edge XANES spectra of the *as deposited* amorphous Co NPs (cyan), and in aqueous KPi buffer poised at -0.3 (plain red), -0.5, -0.7 and -0.9 V *vs.* RHE.

Figure 2-6A shows the cyclic voltamograms recorded on the $[Co(dpg)_3(BF)_2]^+$ (where dpg stands for diphenylglyoxime) complex in acetonitrile in the absence and the presence of perchloric acid. It was demonstrated elsewhere[30] that the voltamograms under acidic conditions describe the electrochemical reduction of the glyoxime ligands and the de-coordination of the cobalt ion. The formation of nanoparticles upon constant potential electrolysis at -0.35 V *vs.* RHE in the presence of perchloric acid was evidenced by SEM images of the electrodes surface after electrolysis (see figure 2-6B), which showed ill-defined half-sphere of *ca.* 100 nm in diameter. The electrodeposition process was followed by cobalt K-edge XANES and EXAFS spectra were recorded when the deposition process was

complete. These data show that the nanoparticles formed are amorphous, since neither the XANES nor the EXAFS data match those of the *hcp* or *fcc* allotropes of cobalt (see figure 2-6C). Based on EXAFS fits, we could determine that the smallest ordered domains in the large particles were about 2 nm in size. These particles, once set into an aqueous buffer, are converted for a large fraction (*ca.* 50%) to cobalt (II). Applying a negative potential to reach HER conditions leads to a conversion of this oxidized fraction back to a metallic species (see figure 2-6D). Interestingly, the initial XANES spectra of the purely metallic species formed after deposition in acetonitrile could never be recovered, even at highly cathodic potentials. The remaining oxidized cobalt species was identified by XANES linear combination fittings and EXAFS fittings as cobalt(II) phosphate. It is interesting to note that, even at very highly cathodic potentials, an oxidized form of cobalt remains present at the surface of these nanoparticles.

As a general comment, we would like to point out that *in situ/operando* XAS is an ideal tool to demonstrate the intactness of molecular catalysts that are used for energy-related electrocatalysis, which is a major concern in many of these systems.[31–33]

2.4 An outlook on the use of X-ray spectroscopies for electrocatalysis research

Photon in/photon out X-ray spectroscopies are invaluable techniques for the study of catalysts under working conditions. The high penetration depth of hard X-rays allows complex experimental setups, and the palette of spectroscopies available nowadays provides a wealth of information on low-order systems. There are, however, limitations to the technique in the current state of beamlines and data acquisition methods, which could hopefully be overcome in the near future.

Up to now and as far as we are aware of, *operando* X-ray spectroscopies applied to electrocatalysis have been used to determine the nature of a catalyst under functioning conditions *in the steady state*. The vast majority of the systems studied are based on materials deposited as films on a working electrode (sometimes it is the electrode itself). These electrochemical systems are highly heterogeneous, because of their porosity, the size of the domains or particles and the presence of a solid-liquid interface. Heterogeneities also exist throughout the film during operation, due to the electrochemical potential, access to substrate or electrical conductivity. Several species are therefore present at the same time in such systems, even in the resting state. In the case of the OER, the O-O bond formation in transition metal oxides have been shown to occur at a few, high oxidation state sites, while the others remain in a "spectator", low oxidation state.[34] This is also true for the HER and certainly for the CRR, although it is less documented as of now.
Distinguishing the different species present in such a material in space and time is a challenge that will probably require decades to solve. Indeed, the timescales required to record an XAS or XES spectrum on most current beamlines (on the order of minutes at best), does not allow observing any transient intermediate. Moreover, due to their penetration depth, X-ray techniques probe a volume rather than a surface (with the exception of X-ray photoemission spectroscopy, XPS). In most cases, the information collected therefore describes the "steady state" of a reaction, with a complex distribution of species in time and space. This situation

explains the current limitations in the use of X-ray spectroscopy to access detailed information on catalysts such as the electronic and local structure of transient species prior to bond formation.

The solutions to these issues are multiple, but can be organized in three axes:

i) the use of time-resolved spectroscopy, either at synchrotrons or free electron lasers (XFELs), should allow accessing transient intermediates. The application of time-resolved XAS to electrochemistry is, however, very challenging from an experimental point of view, especially in the case of XFELs. The use of Von Hamos X-ray emission spectrometer can be very helpful to perform time-resolved spectroscopy (no motor is required to move), although it does not provide as much structural information as XAS. The use of Quick-XAS beamlines is very appealing to reach sub-second timescales and we will present in the next chapter our first attempts to use them for energy-related electrochemistry applications. Time-resolved X-ray spectroscopy would nonetheless suffer from the mixture of species that are present at a given moment in an electrocatalytic film.

ii) Surface techniques such as grazing incidence X-ray spectroscopy or XPS could be used to probe the active surface of a catalytic film. The application of these techniques to the *operando* study of electrocatalytic system represents a significant challenge, but Near-ambient pressure XPS has seen tremendous progresses in the last years and several studies of electrochemical systems using these techniques have been published recently.[35]

iii) The study of model systems could be a valuable approach to disentangle the complex mixture of species in an electrocatalytic system. Molecular species or very thin layers of catalysts, which behavior would be easier to control and understand, could be studied as simplified systems to provide information on single sites or interfacial behavior.

References

(1) Grunwaldt, J.-D.; Kimmerle, B.; Baiker, A.; Boye, P.; Schroer, C. G.; Glatzel, P.; Borca, C. N.; Beckmann, F. ***Catal. Today*** **2009**, ***145*** (3–4), 267–278.

(2) Scott, F. J.; Roth, C.; Ramaker, D. E. ***J. Phys. Chem. C*** **2007**, ***111*** (30), 11403–11413.

(3) OGrady, W. E.; Pandya, K. I.; Swider, K. E.; Corrigan, D. A. ***J. Electrochem. Soc.*** **1996**, ***143*** (5), 1613–1616.

(4) Gorlin, Y.; Lassalle-Kaiser, B.; Benck, J. D.; Gul, S.; Webb, S. M.; Yachandra, V. K.; Yano, J.; Jaramillo, T. F. ***J. Am. Chem. Soc.*** **2013**, ***135*** (23), 8525–8534.

(5) Klingan, K.; Ringleb, F.; Zaharieva, I.; Heidkamp, J.; Chernev, P.; Gonzalez-Flores, D.; Risch, M.; Fischer, A.; Dau, H. ***ChemSusChem*** **2014**, ***7*** (5, SI), 1301–1310.

(6) Kanan, M. W.; Nocera, D. G. ***Science*** **2008**, ***321*** (5892), 1072–1075.

(7) Kanan, M. W.; Yano, J.; Surendranath, Y.; Dinca, M.; Yachandra, V. K.; Nocera, D. G. ***J. Am. Chem. Soc.*** **2010**, ***132*** (39), 13692–13701.

(8) Bediako, D. K.; Lassalle-Kaiser, B.; Surendranath, Y.; Yano, J.; Yachandra, V. K.; Nocera, D. G. ***J. Am. Chem. Soc.*** **2012**, ***134*** (15), 6801–6809.

(9) Dinca, M.; Surendranath, Y.; Nocera, D. G. ***Proc. Natl. Acad. Sci. United States Am.*** **2010**, ***107*** (23), 10337–10341.

(10) Gorlin, Y.; Jaramillo, T. F. ***J. Am. Chem. Soc.*** **2010**, ***132*** (39), 13612–13614.

(11) Gul, S.; Ng, J. W. D.; Alonso-Mori, R.; Kern, J.; Sokaras, D.; Anzenberg, E.; Lassalle-Kaiser, B.; Gorlin, Y.; Weng, T.-C.; Zwart, P. H.; Zhang, J. Z.; Bergmann, U.; Yachandra, V. K.; Jaramillo, T. F.; Yano, J. ***Phys. Chem. Chem. Phys.*** **2015**, ***17*** (14), 8901–8912.

(12) Alonso-Mori, R.; Kern, J.; Sokaras, D.; Weng, T.-C.; Nordlund, D.; Tran, R.; Montanez, P.; Delor, J.; Yachandra, V. K.; Yano, J.; Bergmann, U. ***Rev. Sci. Instrum.*** **2012**, ***83*** (7).

(13) Oh, K.; Mériadec, C.; Lassalle-Kaiser, B.; Dorcet, V.; Fabre, B.; Ababou-Girard, S.; Joanny, L.; Gouttefangeas, F.; Loget, G. ***Energy Environ. Sci.*** **2018**, ***11*** (9), 2590–2599.
(14) Riaz, U.; Curnow, O. J.; Curtis, M. D. ***J. Am. Chem. Soc.*** **1994**, ***116*** (10), 4357–4363.
(15) Eijsbouts, S.; Mayo, S. W.; Fujita, K. ***Appl. Catal. A*** **2007**, ***322***, 58–66.
(16) Appel, A. M.; DuBois, D. L.; DuBois, M. R. ***J. Am. Chem. Soc.*** **2005**, ***127*** (36), 12717–12726.
(17) Jaramillo, T. F.; Jorgensen, K. P.; Bonde, J.; Nielsen, J. H.; Horch, S.; Chorkendorff, I. ***Science*** **2007**, ***317*** (5834), 100–102.
(18) Laursen, A. B.; Kegnaes, S.; Dahl, S.; Chorkendorff, I. ***Energy Environ. Sci.*** **2012**, ***5*** (2), 5577–5591.
(19) Merki, D.; Hu, X. ***Energy Environ. Sci.*** **2011**, ***4*** (10), 3878–3888.
(20) Tang, M. L.; Grauer, D. C.; Lassalle-Kaiser, B.; Yachandra, V. K.; Amirav, L.; Long, J. R.; Yano, J.; Alivisatos, A. P. ***Angew. Chemie Int. Ed.*** **2011**, ***50*** (43), 10203–10207.
(21) Hibble, S. J.; Rice, D. A.; Pickup, D. M.; Beer, M. P. ***Inorg. Chem.*** **1995**, ***34*** (21), 5109–5113.
(22) Hibble, S. J.; Walton, R. I.; Pickup, D. M.; Hamon, A. C. ***J. Non. Cryst. Solids*** **1998**, ***232***, 434–439.
(23) Weber, T.; Muijser, J. C.; Niemantsverdriet, J. W. ***J. Phys. Chem.*** **1995**, ***99*** (22), 9194–9200.
(24) Merki, D.; Fierro, S.; Vrubel, H.; Hu, X. ***Chem. Sci.*** **2011**, ***2*** (7), 1262–1267.
(25) Lassalle-Kaiser, B.; Merki, D.; Vrubel, H.; Gul, S.; Yachandra, V. K.; Hu, X.; Yano, J. ***J. Am. Chem. Soc.*** **2015**, ***137*** (1), 314–321.
(26) Chatterjee, S.; Sengupta, K.; Dey, S.; Dey, A. ***Inorg. Chem.*** **2013**, ***52*** (24), 14168–14177.
(27) Tran, P. D.; Tran, T. V; Orio, M.; Torelli, S.; Truong, Q. D.; Nayuki, K.; Sasaki, Y.; Chiam, S. Y.; Yi, R.; Honma, I.; Barber, J.; Artero, V. ***Nat. Mater.*** **2016**, ***15*** (6), 640+.
(28) Chao, T. H.; Espenson, J. H. ***J. Am. Chem. Soc.*** **1978**, ***100*** (1), 129–133.
(29) Dempsey, J. L.; Brunschwig, B. S.; Winkler, J. R.; Gray, H. B. ***Acc. Chem. Res.*** **2009**, ***42*** (12), 1995–2004.
(30) Anxolabehere-Mallart, E.; Costentin, C.; Fournier, M.; Nowak, S.; Robert, M.; Saveant, J.-M. ***J. Am. Chem. Soc.*** **2012**, ***134*** (14), 6104–6107.
(31) Sconyers, D. J.; Blakemore, J. D. ***Chem. Commun.*** **2017**, ***53*** (53), 7286–7289.
(32) El Ghachtouli, S.; Guillot, R.; Brisset, F.; Aukauloo, A. ***ChemSusChem*** **2013**, ***6*** (12), 2226–2230.
(33) Cherdo, S.; El Ghachtouli, S.; Sircoglou, M.; Brisset, F.; Orio, M.; Aukauloo, A. ***Chem. Commun.*** **2014**, ***50*** (88), 13514–13516.
(34) Bediako, D. K.; Surendranath, Y.; Nocera, D. G. ***J. Am. Chem. Soc.*** **2013**, ***135*** (9), 3662–3674.
(35) Lettenmeier, P.; Majchel, J.; Wang, L.; Saveleva, V. A.; Zafeiratos, S.; Savinova, E. R.; Gallet, J.-J.; Bournel, F.; Gago, A. S.; Friedrich, K. A. ***Chem. Sci.*** **2018**, ***9*** (14), 3570–3579.

Chapter 3 : Time-resolved X-ray spectroscopic and microfluidic tools for the study of CO_2 reduction reactions

3.1 Why it is worth working on CO_2 reduction reactions

This chapter will focus on our upcoming projects, some of them being already underway and others being only described on paper. After working for several years on the study of water splitting reactions (HER and OER), we figured that advances in the implementation of noble metal-free technologies may require more engineering than fundamental breakthrough. CO_2 reduction reactions (CRR), on the other hand, are still in their infancy. Because of the wide variety of products that they can form, the mechanism that they can follow and the catalysts that they can use, these reactions offer a fantastic and virtually unlimited playground for he who seeks understanding fundamental aspects of the structure and behavior of catalysts. The potential applications in industrial gas exhaust treatment, synthetic chemistry or energy-related catalysis[1,2] make it a very attractive and important research topic.

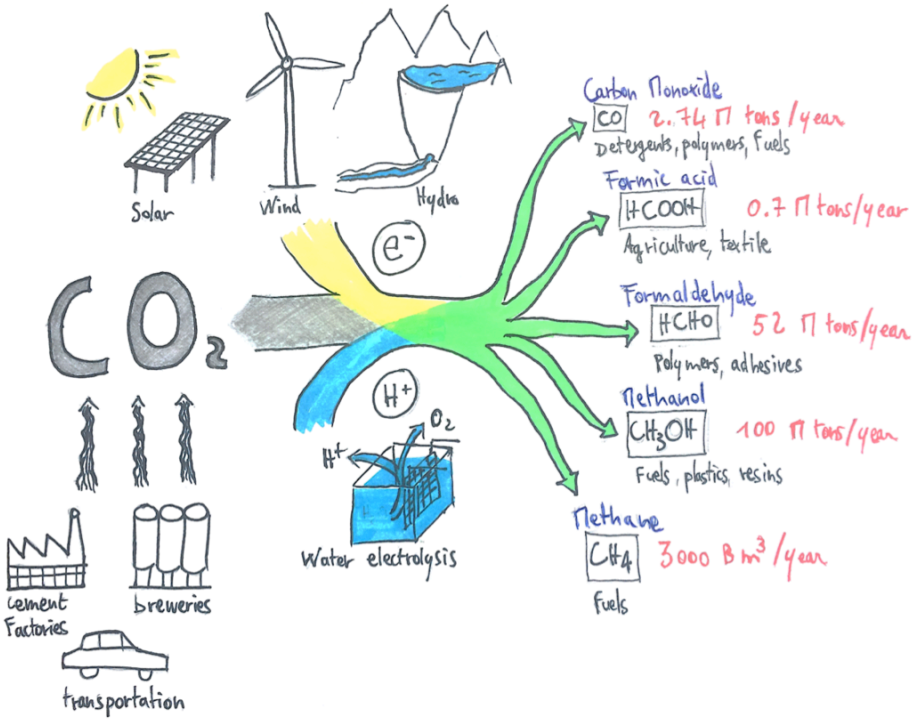

Figure 3-1. Simplified representation of the anthropogenic CO_2 sources and of the C_1 products formed by the direct reduction of CO_2. Their global yearly productions are indicated (in red) as well as their uses in industrial applications. Potential sources of protons (water electrolysis) and renewable energies required for the reduction of CO_2 are also depicted.

Figure 3-1 shows a simplified picture of CO_2 emissions and potential use in industrial societies. Carbon dioxide is produced by many industrial processes such a cement factories, breweries, steam reforming plants (producing hydrogen and CO_2 from methane) or agricultural waste fermenters (producing CH_4 and CO_2 from biomass), but also by land, sea and air transportation and by coal or fossil fuel-based power plants. Some of these CO_2 sources are diluted (about 20% in vehicle exhaust gas), while others are highly concentrated (cement factories, coal power plants). Although utilizing directly the diluted CO_2 expelled by moving vehicles seems too complex, the valorization of concentrated and stationary CO_2 sources should be much more realizable on a technological point of view. The amounts of CO_2 generated are very important (about 40 billion tons in 2010) and the simplest chemicals that can be produced by its reduction all find attractive applications in the industry. The left part of figure 3-1 shows the annual productions and a few application areas of the five C_1 products that can be obtained from the direct reduction of CO_2. All of them account for several millions of tons per year, which should provide enough incentive to master their production from CO_2.
The electrochemical production of carbon monoxide and formic acid from CO_2 has been described through many academic examples,[3,4] but their implementation on industrial scales is just beginning.[5] Formaldehyde, methanol and methane, on the other hand, have only been produced by CO_2 reduction in a handful of cases at the laboratory scale. The five C_1 products that can be directly produced from CO_2 reduction are already used as such in several industrial fields or directly as fuels. But most of them can also be used as synthetic building blocks for more complex chemical syntheses. Being able to reduce CO_2 into these C_1 compounds efficiently and with technological and economical feasibility would be a very important step in the reduction of CO_2 emissions. But beyond that, understanding the fundamental chemical steps of catalysis that lead to these products should allow controlling their reactivity in such a way that C-C bonds could be formed to produce more complex, higher value chemicals. Overall, the production on large scales of a wide variety of chemicals using *reductive chemistry* based on CO_2 rather than an *oxidative chemistry* based on fossil hydrocarbons would completely change the impact of industry and energy production on our societies. A lot of research is clearly required to improve the efficiency and scalability of CO_2 reduction reactions, both from fundamental and applied aspects. Electrochemical reactions, because of the necessity to store electrical energy under the form of chemical bonds, will certainly play an important role in this long-term, global endeavor.[6]

In this context, we have engaged in two parallel projects related to CO_2 reduction, which are described in this chapter. The first one deals with the development of time-resolved X-ray spectroelectrochemistry, which we will apply to CRR-active molecular catalysts. This project has been funded by the Charmmmat (2017, in collaboration with Dr. Zakaria Halime and Dr. Khaled Cheaib, Université Paris-Sud) and Michem (2018, in collaboration with Pr. Marc Robert, Dr. Elodie Anxolabéhère-Mallart, Université Paris Diderot) LABEX and the first experiments were already performed on the ROCK beamline at SOLEIL. The second project is aiming at the application of microfluidic systems to the electrochemical reduction of CO_2 and received its first funding in 2018 (young researcher ANR grant).

3.2 Time-resolved X-ray spectroelectrochemistry for the study of CO_2 reduction reactions

3.2.1 Molecular CO_2 reduction reactions

As mentioned in the introduction of this chapter, the electrochemical reduction of CO_2 can be performed by many different types of catalysts, yielding many different products and following complex reaction routes. Pure metals at the right of the periodic table such as silver, gold or copper show good performances in converting CO_2 into CO (Ag and Au) or more complex products (Cu). Molecular system have also shown interesting performances for the reduction of CO_2 into CO, as shown by the pioneering work of Sauvage and Savéant on nickel cyclams[7] and iron prophyrins[8], respectively. More recently, iron[9] and cobalt[10] macrocycles have received an increased attention, due to their synthetic tunability, their robustness and their high turnover rates and numbers for CRR. Despite detailed electrochemical analysis of their reaction mechanism for the CO_2 to CO reduction,[11] spectroscopic information are still missing to describe intermediates along the catalytic cycle. In the particular case of porphyrins, the electronic structure of the most reduced species – whether the electrons are localized on the central metal or on the porphyrin backbone – is still a matter of debate.[12] Intermediates such as $Fe(I)CO_2^{\cdot-}$ (the adduct formed by addition between the reduced Fe(0) species and CO_2) or Fe(II)CO have been suggested but their precise local and electronic structures remain elusive and lack extensive spectroscopic signatures.[13] Scheme 3-1 shows the molecular structure of a water-soluble iron porphyrin and the putative catalytic cycle associated to it for the CO_2 to CO reduction.

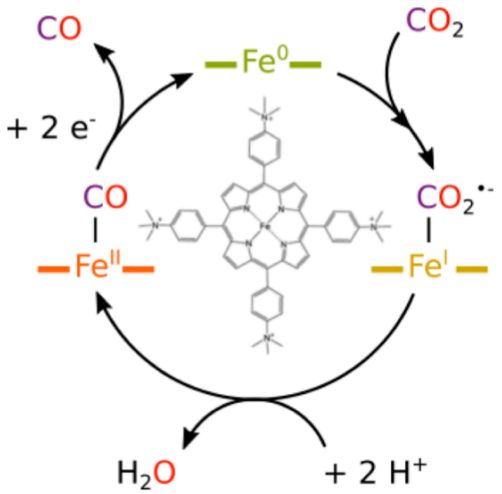

Scheme 3-1. Possible mechanism for the electrocatalytic reduction of CO_2 into CO by FeTTMAPP. The molecular structure of FeTTMAPP is represented at the center of the scheme.

The establishment of the so-called Quick-XAS beamlines (beamline 10.3.2 at the ALS,[14] ROCK beamline in SOLEIL,[15] SuperXAS in SLS[16]) that can record spectra in the ms timescale make this technique a very good choice to study electrocatalysts. Although the lifetime of actual reaction intermediates is even shorter, specific species can be accumulated when tuning the experimental conditions of an electrochemical experiment (*i.e.* scan speed, concentration, temperature). Experimental and methodological developments are, however, required to make it available to the largest number and to access valuable information on a wide variety of systems. Providing a time-resolved method to identify transient species during electrocatalysis would be very valuable for the field of molecular CO_2 reduction, but also for electrocatalysis in general.

3.2.2 Technical developments

In order to collect time-resolved XAS data along a cyclic voltamogram, we have designed a spectroelectrochemical cell for X-ray spectroscopic transmission measurements. A schematic of it is represented on figure 3-2, where the X-ray beam path, the electrodes and the liquid circulation channels are depicted. The main issue lies in the balance between an appropriate path length (too small would prevent a good S/N ratio, while too long would yield a too small edge-jump) and a correct electrochemical behavior. The current configuration of the cell allows recording spectra of a solution while performing a cyclic voltamogram on it. A three-dimensional electrode was used, so that the whole solution was subject to a potential change and that the spectra collected correspond to the complete conversion of a species.

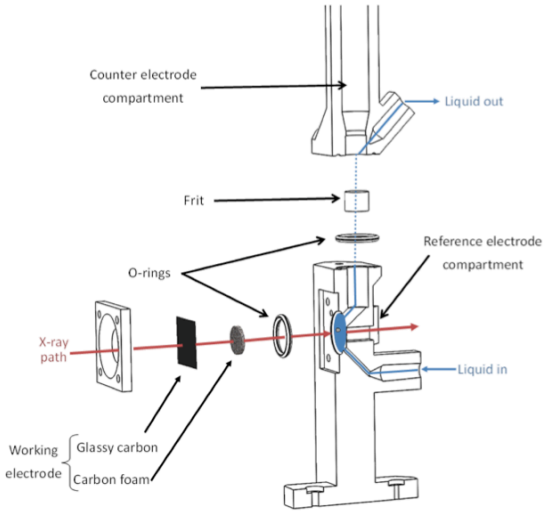

Figure 3-2. Schematic representation of the transmission XAS spectroelectrochemical cell for time-resolved experiments.

3.2.3 Preliminary results

In collaboration with the team of Dr. Zakaria Halime at the Université Paris-Sud, we collected time-resolved data at the ROCK beamline on a model system, Fe(III)Cl_3, using a 2 mm path length and a carbon foam as working electrode. Figure 3-3A shows the cyclic voltamogram recorded within this cell, which shows a chemically irreversible but electrochemically reversible system, which is due to the difference of chloride ligands in the +II (2 Cl) or +III (3 Cl) oxidation states.

Figure 3-3B shows the Fe K-edge XANES spectra of pure $FeCl_2$ and $FeCl_3$ aqueous solutions (20 mM) together with a spectrum measured after a 20 min bulk electrolysis at -0.8 V *vs.* Ag/AgCl. This spectrum is nearly identical to the spectrum measured on a pure $FeCl_2$ solution and linear combination fittings using the solution spectra of $FeCl_2$ and $FeCl_3$ indicate a conversion of 90%. We then collected data along the course of a cyclic voltamogram, with a scanning speed of 20 mV/sec. XAS data were collected with a monochromator oscillation frequency of 2 Hz (only forward data were recorded) and spectra were averaged over 5 seconds (10 spectra, 100mV). Figures 3-3C and D show the series of XAS spectra recorded along this voltamogram. It can be clearly seen that after 100 seconds (E = -1.0 V ± 50 mV) and 190 seconds (E = 0.0 V ± 50 mV), the spectra are almost identical to those of pure $FeCl_2$ and $FeCl_3$ solutions, respectively. Linear combination fittings allowed quantifying the amount of conversion at different points of the voltamogram, which were plotted on figure 3-3E. The profiles observed show a 90% conversion at extreme potentials and are completely in line with what is expected theoretically.[17]

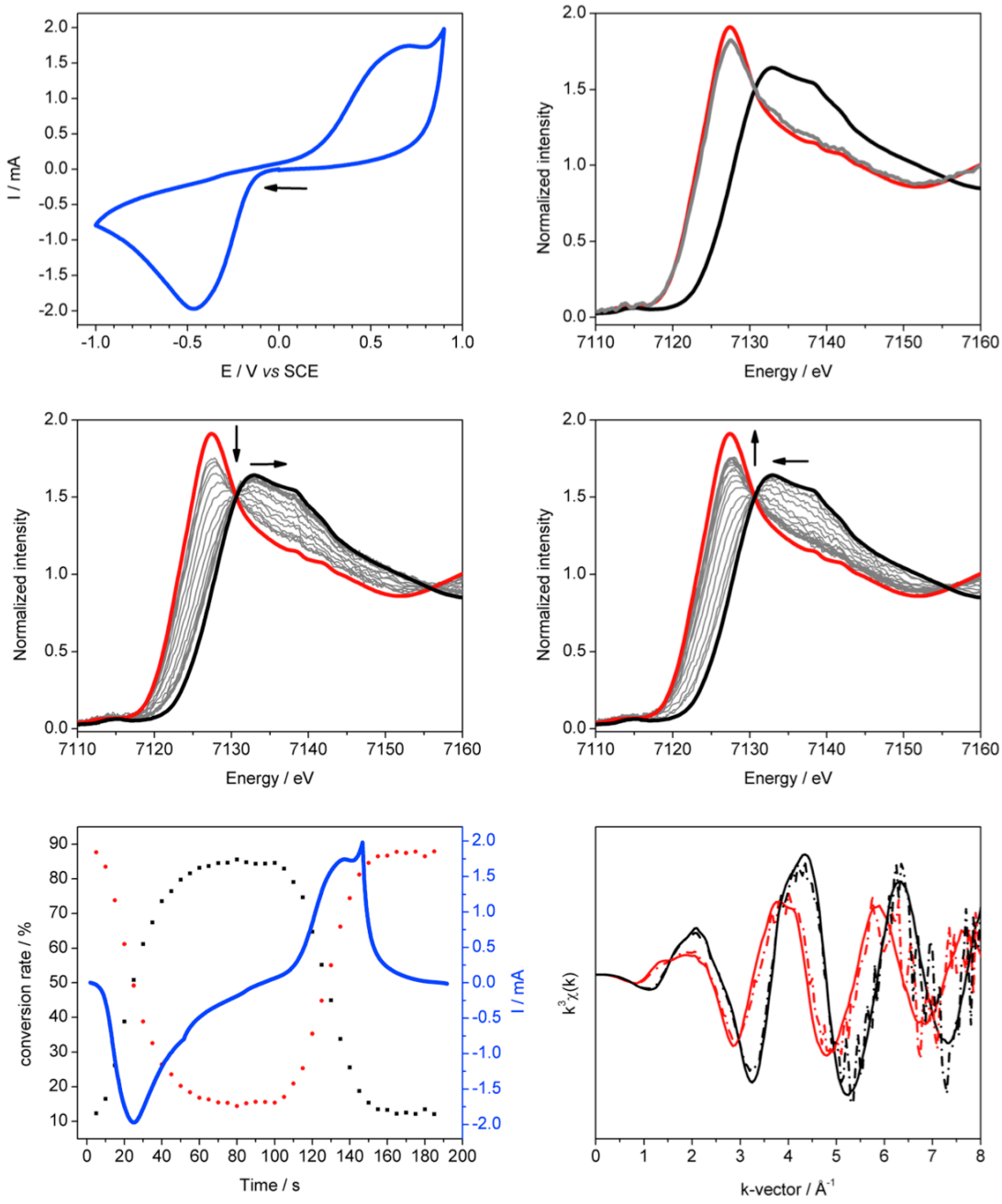

Figure 3-3. Cyclic voltamogram recorded on a 20 mM aqueous $Fe(III)Cl_3$ solution (20mV/s scanning speed) in the X-ray transmission electrochemical cell shown on figure 3-2 (A). Fe K-edge XANES spectra of $Fe(III)Cl_3$ (black) and $Fe(II)Cl_2$ (red) and of an $Fe(III)Cl_3$ solution converted into $Fe(II)Cl_2$ after bulk electrolysis at -0.8 V (gray) (B). Time-resolved Fe K-edge XANES spectra recorded during a cyclic voltamogram (averaged over 5 seconds) (C, D). The reduction and re-oxidation processes are shown on panel (C) and (D), respectively. The reference spectra of the $Fe(III)Cl_3$ (black) and $Fe(II)Cl_2$ (red) solution are shown for comparison. $Fe(III)Cl_3$ (dotted red) and $Fe(II)Cl_2$ (dotted black) concentrations (obtained from XANES linear combination fittings) and current profiles observed during a cyclic voltamogram (E) and EXAFS k-space signal from pure $Fe(III)Cl_3$ (black plain), and $Fe(II)Cl_2$ (red plain) solutions and from time-resolved spectra (averaged over 5 seconds) after 100 (dotted black) and 185 (dotted red) seconds after the start of the voltamogram (F).

EXAFS data were also collected along this voltamogram. Figure 3-3F shows the k^3 weighted EXAFS of reference solutions of $FeCl_3$ and $FeCl_2$ and of the spectra recorded after 100 seconds (E = -1.0 V ± 50 mV) and 190 seconds (E = 0.0 V ± 50 mV). Although the signal-to-noise quality is only sufficient for a crude Fourrier Tranform analysis (not shown here), the changes observed along the voltamogram are clearly in line with the spectra of the pure species.

All together, these results demonstrate the feasibility of time-resolved X-ray spectrolectrochemistry under cyclic voltametry conditions. The time resolution that we have attained is clearly not sufficient to identify intermediates, but we are actively working on the optimization of the setup and data collection methodology in order to access higher scanning speeds. Once achieved, these technical progresses will be applied to the study of CO_2-reducing transition metal macrocycles such as iron porphyrins.

3.3 Microfluidic systems for the sequential reduction of CO_2

3.3.1 Microfluidics as a new discovery tool

In a very simplified approximation, the current research on CRR follows two paths. One of them seeks to optimize the selectivity of catalysts that produce a variety of products (metallic copper is an iconic example of such catalyst), while the other path seeks to improve the performances (turnover numbers and frequency) of catalysts that reduce CO_2 into low added-value molecules, such as CO or CH_4. Molecular transition metal macrocycles are good examples of the second path. A third path has emerged in recent years, which aim is to couple single CO_2 reducing reactions within multicatalytic sequential processes.[18,19] One advantage of this strategy is that it allows optimizing each single catalyst independently from one another. Complex reaction schemes can also be imagined, where the product of a reaction could be used for multiple following ones. Such reaction scheme is, however, difficult to test on many catalysts and reactions when using typical lab-scale reaction flasks. Microfluidics, on the other side, allows manipulating very small amounts of liquids and hence the parallelization of reactions using very small amounts of catalysts. Its application to energy-related topics is barely beginning,[20] but it holds promises as a catalyst screening tool. It has also been proposed as an interesting membraneless approach to avoid product mixing in electrocatalytic systems, thanks to laminar flow conditions.[21]

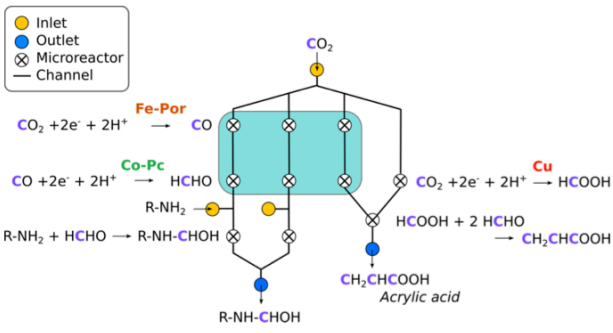

Scheme 3-2. Conceptual representation of the sequential CO_2 reduction into formaldehyde or more complex products in microfluidic reactors. The area highlighted in blue is the primary goal of the project, which will demonstrate the feasibility and interest of this approach.

In order to screen the potential of multicatalysis in short times and with small amounts of catalysts and reactants, we proposed a project where microfluidic reactors will be set in series, so as to perform two or more sequential reduction reactions starting from CO_2. Our primary objective is the formation of formaldehyde from CO_2 through CO, but other reaction schemes can clearly be imagined. Scheme 3-2 describes the concept of microfluidic sequential reactions, which can be complexified at will. The advantage of this approach is that it allows the implementation of tens of parallel systems, in which various reaction conditions (such as the pH, the nature of the buffer or its concentration) can be tested in parallel on the same series of catalysts. Conversely, a series of CO reducing catalysts can be tested in parallel in reactor n°2 using the same CO producing catalysts in reactor n°1, thus avoiding the unsafe use of large volumes of CO.

Another advantage of microfluidic systems is the existence of laminar flow conditions, due to the high Reynolds values obtained in micron-sized channels. These conditions allow performing two electrochemical reactions in the same liquid, without requiring the use of a membrane. CO_2 could thus be reduced at a cathode while H_2O would be oxidized at an anode, without having any mixing issues between the products of each electrode. A face-to-face configuration would allow the anolytes and catholytes to circulate from one microreactor to the next without any mixing (except for the diffusion at the liquid-liquid interface). This concept has already been applied to water splitting, where O_2 and H_2 are produced on the opposite sides of a microfluidic channel and separated using the laminar flow properties of the electrolyte.[21] Figure 3-4 describes such a configuration and shows our first prototype using nickel and copper electrodes as anode and cathode, respectively.

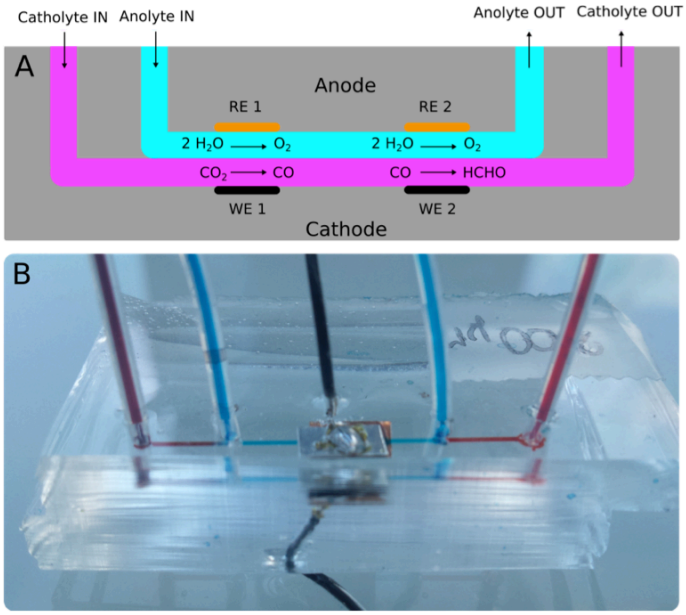

Figure 3-4. Schematic description of a face-to-face setup with two consecutive pairs of electrodes (A). The first pair performs the CO_2 to CO reaction, while the second performs the CO to HCHO reaction. RE and WE stand for reference and working electrodes, respectively. First observation of a laminar flow in a nickel/copper microfluidic system produced in our labs (B).

In order to rapidly evaluate the efficiency of a catalyst, we will develop on-line detection systems for CO and formaldehyde. CO is known for binding to hemoglobin, which color changes as a function of CO concentration (detectable with a sharp peak at 414 nm).[22] Similarly, fluoral is a molecule that has been developed to detect trace amounts of formaldehyde.[23] The reaction of fluoral (colorless, with a peak at 300 nm) with formaldehyde yields 3,5-diacetyl-1,4-dihydrolutidine (yellow, with a peak at 400 nm) quantitatively. Both CO and HCHO can thus be detected qualitatively and quantitatively using these colorimetric agents and a UV-visible detection system. We will thus develop microfluidic systems that will mix the outlet products of a microreactor with one of the colorimetric agents, allow for mixing time and reaction and circulate into a detection chamber set in a UV-visible spectrometer. Scheme 3-3 depicts a microfluidic setup with multiple parallel sequential reaction lines and with online detection tools for the production of CO or HCHO. These online systems are, however, only specific to certain products. Other analytical tools such as gas phase chromatography (GC) or high pressure liquid phase chromatography (HPLC) will therefore be used at the very end of each sequential reaction line.

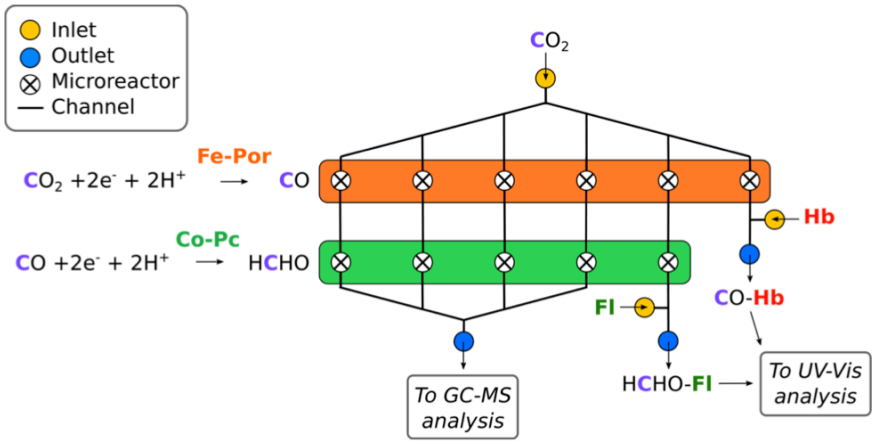

Scheme 3-3. Simplified description of the parallelization possibilities offered by microfluidic microreactors. The orange and green areas indicate microreactors where reactions occur in parallel for the reduction of CO_2 and CO, respectively. 'Hb' stands for Hemoglobin and 'Fl' for Fluoral.

Although this project does not aim at improving the efficiency of each single reaction, the development of microfluidic systems combining sequential reactions with on-line analysis tools will provide a useful platform for the discovery of new catalysts or catalytic conditions. Indeed, the CO reduction reaction is hardly studied, in part because of the safety issues associated with the manipulation of CO. Having a system that allows producing CO in small and controlled amounts will provide a convenient platform to test new catalysts. The development of parallel microreactor arrays implemented with different catalysts could therefore be used for the accelerated testing of catalysts under identical conditions.
In a similar way to the combinatorial approach used for the discovery of water-splitting catalysts,[24] these systems could be used to explore a wide range of catalysts and catalytic conditions in a minimal amount of time.

References

(1) Centi, G.; Quadrelli, E. A.; Perathoner, S. ***Energy Environ. Sci.*** **2013**, ***6*** (6), 1711–1731.
(2) Centi, G.; Perathoner, S. ***Catal. Today*** **2009**, ***148*** (3–4), 191–205.
(3) Leitner, W. ***Angew. Chemie Int. Ed.*** **1995**, ***34*** (20), 2207–2221.
(4) Whipple, D. T.; Kenis, P. J. A. ***J. Phys. Chem. Lett.*** **2010**, ***1*** (24), 3451–3458.
(5) Rumayor, M.; Dominguez-Ramos, A.; Irabien, A. ***Appl. Sci.*** **2018**, ***8*** (6).
(6) Tatin, A.; Bonin, J.; Robert, M. ***ACS Energy Lett.*** **2016**, ***1*** (5), 1062–1064.
(7) Beley, M.; Collin, J. P.; Ruppert, R.; Sauvage, J. P. ***J. Chem. Soc. Commun.*** **1984**, No. 19, 1315–1316.
(8) Bhugun, I.; Lexa, D.; Savéant, J. M. ***J. Am. Chem. Soc.*** **1994**, ***116*** (11), 5015–5016.
(9) Costentin, C.; Drouet, S.; Robert, M.; Saveant, J.-M. ***Science*** **2012**, ***338*** (6103), 90–94.
(10) Shen, J.; Kortlever, R.; Kas, R.; Birdja, Y. Y.; Diaz-Morales, O.; Kwon, Y.; Ledezma-Yanez, I.; Schouten, K. J. P.; Mul, G.; Koper, M. T. M. ***Nat. Commun.*** **2015**, ***6***.
(11) Costentin, C.; Robert, M.; Saveant, J.-M. ***Acc. Chem. Res.*** **2015**, ***48*** (12), 2996–3006.
(12) Romelt, C.; Song, J.; Tarrago, M.; Rees, J. A.; van Gastel, M.; Weyhermueller, T.; DeBeer, S.; Bill, E.; Neese, F.; Ye, S. ***Inorg. Chem.*** **2017**, ***56*** (8), 4745–4750.
(13) Bae, I. T.; Scherson, D. A. ***J. Phys. Chem. B*** **1998**, ***102*** (14), 2519–2522.
(14) Marcus, M. A.; MacDowell, A. A.; Celestre, R.; Manceau, A.; Miller, T.; Padmore, H. A.; Sublett, R. E. ***J. Synchrotron Radiat.*** **2004**, ***11*** (3), 239–247.
(15) Briois, V.; La Fontaine, C.; Belin, S.; Barthe, L.; Moreno, T.; Pinty, V.; Carcy, A.; Girardot, R.; Fonda, E. ***J. Phys. Conf. Seires*** **2016**, ***712***, 12149.
(16) Mueller, O.; Nachtegaal, M.; Just, J.; Luetzenkirchen-Hecht, D.; Frahm, R. ***J. Synchrotron Radiat.*** **2016**, ***23*** (1), 260–266.
(17) Saveant, J.-M. In ***Elements of Molecular and Biomolecular Electrochemistry***; Wiley-Blackwell, 2006; pp 1–77.
(18) Jensen, M. T.; Ronne, M. H.; Ravn, A. K.; Juhl, R. W.; Nielsen, D. U.; Hu, X.-M.; Pedersen, S. U.; Daasbjerg, K.; Skrydstrup, T. ***Nat. Commun.*** **2017**, ***8***.
(19) Gotico, P.; Del Vecchio, A.; Audisio, D.; Quaranta, A.; Halime, Z.; Leibl, W.; Aukauloo, A. ***ChemPhotoChem 2*** (8), 715–719.
(20) Modestino, M. A.; Rivas, D. F.; Hashemi, S. M. H.; Gardeniers, J. G. E.; Psaltis, D. ***Energy Environ. Sci.*** **2016**, ***9*** (11), 3381–3391.
(21) Hashemi, S. M. H.; Modestino, M. A.; Psaltis, D. ***Energy Environ. Sci.*** **2015**, ***8*** (7), 2003–2009.
(22) Wang, S.; Yuan, F.; Chen, G.; Tu, K.; Wang, H.; Wang, L.-Q. ***RSC Adv.*** **2014**, ***4*** (95), 52940–52948.
(23) de Oliveira, F. S.; Sousa, E. T.; de Andrade, J. B. ***Talanta*** **2007**, ***73*** (3), 561–566.
(24) Neyerlin, K. C.; Bugosh, G.; Forgie, R.; Liu, Z.; Strasser, P. ***J. Electrochem. Soc.*** **2009**, ***156*** (3), B363–B369.

Perspective : Reflexions on the future of Artificial Photosynthesis

The early days of artificial water-splitting were driven by the progresses made in our understanding of the active sites of Photosystem II or hydrogenases. In that regard, the first crystallographic structures of these enzymes had a very high impact, which directed chemists in their synthetic strategies. Generally speaking, the field believed that biomimetic chemistry could faithfully reproduce the active sites of enzymes and have them function in the same way enzymes do. Complex molecular architectures were developed to generate photochemical charge separations and funnel them into catalytic processes. Soon enough, issues such as charge recombination, kinetic mismatch between single photon events and multi-electronic catalysis occurred, not to mention the instability of catalysts on the long term. In order to face the challenge of the availability of renewable energy, the field naturally reoriented itself towards more stability and compatibility with existing devices.

We have shown in Chapter 1 that the study of natural photosynthesis is still going on, more exciting than ever. The molecular mechanistic models that have been produced and studied in search for biomimetic counterparts to the active site of the OEC have greatly improved our knowledge of the structure and reactivity of high-valent manganese complexes. The description of the water oxidation catalytic mechanism in PS II is probably reaching its climax and provides great inspiration for the design of artificial catalysts, suggesting that radical character on the oxygen is key, that the presence of calcium or a similar lewis-acid is beneficial and that a flexible structure to accommodate for bond length changes is critical.
We mentioned in Chapter 2 that the field of artificial photosynthesis evolved towards the use of materials for artificial photosynthetic processes. Understanding the structure of these catalysts – which are amorphous in their large majority – under functioning conditions has been made possible by the use of *in situ* and/or *operando* X-ray spectroscopy. Although the technique only allows probing these materials in their steady state today, we can expect that in the near future, time-resolved and surface sensitive techniques should allow catching more fugacious species.
Finally, we have presented in Chapter 3 our current projects on the development of time-resolved X-ray absorption spectroelectrochemistry and its application to study the CO_2 reduction reaction by molecular macrocycles. We have also described our current development of microfluidic devices for the sequential reduction of CO_2 into valuable products. These two aspects of our future work should benefit from each other and strengthen our understanding and control of the CO_2 reduction reactions.

Although artificial photosynthesis has its roots in natural photosynthesis and respiration, it spans nowadays through many different fields of chemistry, going from molecular biology to nanomaterials through photo- and electrocatalysis. The conceptual and practical advances gathered in both natural and artificial water-splitting in the last ten years has tremendously moved the field. Economical and political pressure is obviously part of the equation, not only by the amount of funding directed to scientific and technological research, but also by the ability of governments to promote clean and renewable technologies rather than fossil fuels or nuclear-based ones. The fundamental knowledge that scientist will be able to collect on the basic steps of the activation of small molecules such as water, dioxygen or carbon dioxide will nonetheless eventually impact the wide-spread use of environmentally friendly energy systems.

Annex I : List of abbreviations

ADP: Adenosine diphosphate
ATP: Adenosine triphosphate
ANR: Agence nationale pour la recherche
BUEA: tris[(N′-tert -butylureaylato)-N -ethylene]aminato
CE: Counter electrode
CRR: CO_2 reduction reactions
DFT: Density functional theory
DPG: Diphenyl glyoxime
EPR: Electron paramagnetic resonance
EXAFS: Extended X-ray absorption fine structure
FCC: face centered cubic
FTO: fluorine-doped tin oxide
GDVN: Gas driven virtual nozzle
HCP: hexagonal cubic packed
HER: Hydrogen evolving reaction
IAD: Integrated absolute difference
ITO: Idinum-doped tin oxide
NADH: Nicotinamide adenine dinucléotide
NADPH: Nicotinamide adenine dinucleotide phosphate
LUMO: Lowest unoccupied molecular orbital
OEC: Oxygen evolving complex
OER: Oxygen evolving reaction
ORR: Oxygen reducing reaction
ORTEP: Oak ridge thermal ellipsoid plot program
PS II: Photosystem II
RE: Reference electrode
RHE: Reference hydrogen electrode
SALPN: N,N′-bis(salicylidene)-1,2-propanediamine
SCE: Saturated calomel electrode
SEM: Scanning electron microscope
SXR: Soft X-ray beamline
TEM: Transmission electron microscope
TEY: Total electron yield
WE: Working electrode
XANES: X-ray absorption near edge spectroscopy
XAS: X-ray absorption spectroscopy
XES: X-ray emission spectroscopy
XFEL: X-ray free electron laser
XPS: X-ray photoemission spectroscopy
XRD: X-ray diffraction

Annex II: Curriculum Vitae

Born in Saint-Jean d'Angély (France) on July 12th 1980.
Married, one child

1.1 Career

Jan. 2015 – Present	Head of the Microfluidics Laboratory Synchrotron SOLEIL, Gif-sur-Yvette, France
Apr. 2014 – Present	Beamline Scientist on the LUCIA beamline Synchrotron SOLEIL, Gif-sur-Yvette, France
Nov. 2012 – May 2014	Post-doctoral fellow on the GALAXIES beamline Synchrotron SOLEIL, Gif-sur-Yvette, France
Nov. 2009 – Oct. 2012	Post-doctoral fellow, Physical Bioscience Division Lawrence Berkeley National Laboratory, Berkeley, USA
Nov. 2008 – Oct. 2009	Post-doctoral fellow at the iBiTeC-S Commissariat à l'Energie Atomique, Gif-sur-Yvette, France

1.2 Education

Oct. 2008 PhD in Chemistry
Institut de Chimie Moléculaire et des Matériaux d'Orsay
Supervisors: Pr. Ally Aukauloo, Dr. Elodie Anxolabéhère-Mallart
Université Paris-Sud, Orsay

Sep. 2005 2nd year Master in Chemistry
Université Paris-Sud, Orsay

July 2004 1st year Master in Chemistry
Université de Strasbourg

July 2003 Licence in Chemistry
Université d'Aix-Marseille

July 2002 University Technological Diploma in Chemistry
Université de Strasbourg

1.3 Dissemination of research

1.3.1 Bibliometric indicators (Web of Science)

Researcher ID: I-3748-2015; ORCID: 000-0003-2141-2496

- 42 peer-reviewed publications
- 2000 citations
- h-index: 20
- average publication IF: 10.31

1.3.2 Peer-reviewed publications

Publications related to the PhD

1. Dissymmetric binucleating ligands containing a salophen and bisoxamato cavities.
   B. Lassalle-Kaiser, R. Guillot, A. Aukauloo.*
   Tetrahedron Letters, **2007**, 48, 7004-7006. IF : 2.12

2. Imidazole containing ligands for the modulation of physical properties of metal complexes upon (de)protonation.
   B. Lassalle-Kaiser, R. Guillot, E. Anxolabéhère-Mallart, A. Aukauloo.*
   Tetrahedron Letters, **2006**, 47, 3379-3382. IF : 2.12

3. Artificial systems related to light driven electron transfer processes in PS II.
   C. Herrero, B. Lassalle-Kaiser, W. Leibl, A. W. Rutherford, A. Aukauloo.*
   Coordination Chemistry Reviews, **2008**, 252, 3-4, 456-468. IF : 12.10

4. Proton-Mediated Redox Control in a Nickel(II)-Bisimidazolate Complex: Spectroscopic Characterisation and Density Functional Analysis.
   B. Lassalle-Kaiser, R. Guillot, J. Sainton, M.-F. Charlot, A. Aukauloo.*
   Chemistry A European Journal, **2008**, 14, 14, 4307. IF : 5.16

5. Structural and spectroscopic properties of Ru(II) complexes of 4-(aryl)thiosemicarbazones of thiophen-2-carbaldehyde.
   S. Naskar, S. Naskar, M. G. B. Drew, S. I. Gorelsky, B. Lassalle-Kaiser, A. Aukauloo, M. Dipankar, S. K. Chattopadhyay.*
   Polyhedron, **2009**, ***28***, 18, 4101-4109. IF : 2.06

6. Activation of a water molecule using a mononuclear Mn complex: from Mn-aquo, to Mn-hydroxo, to Mn-oxyl via charge compensation.
   B. Lassalle-Kaiser, C. Hureau, D. A. Pantazis, Y. Pushkar, R. Guillot, V. K. Yachandra, J. Yano, F. Neese*, E. Anxolabéhère-Mallart.*
   Energy and Environmental Science, **2010**, 3, 7, 924-938. IF : 30.07

7. Implications of remote water molecules on the electron transfer coupled processes at a nonporphyrinic Mn(III)-hydroxido complex.
   S. El Ghachtouli, B. Lassalle-Kaiser, P. Dorlet, R. Guillot, E. Anxolabehere-Mallart*, C. Costentin*, A. Aukauloo.*
   Energy and Environmental Science, **2011**, 4, 6, 2041-2044. IF : 30.07

8. Reversible Double Oxidation and Protonation of the Non-Innocent Bridge in a Nickel(II)-Salophen Complex.
   D. de Bellefeuille, M. Askari, B. Lassalle-Kaiser, Y. Journaux, A. Aukauloo, M. Orio, F. Thomas*, X. Ottenwaelder.*
   Inorganic Chemistry, **2012**, 51, 23, 12796-12804. IF : 4.70

9. Electrochemical formation of Mn(III)-peroxo complexes supported by pentadentate amino pyridine and imidazole ligands.
   S. El Ghachtouli, H. Y. V. Ching, B. Lassalle-Kaiser, R. Guillot, D. F. Leto, S. Chattopadhyay, T. A. Jackson,* P. Dorlet* and E. Anxolabéhère-Mallart.*
   Chemical Communication, **2013**,49, 5696-5698. IF : 6.29

10. Electrochemical Implication of a Hydrogen-Bonded Imidazole on a Redox-Active-Bound Phenolate Group.
    S. El Ghachtouli, B. Lassalle-Kaiser, R. Guillot and A. Aukauloo.*
    European Journal of Inorganic Chemistry, **2014**, 28, 4750-4755. IF : 2.96

Publications related to post-doctoral appointments

11. Structural and Electronic Study of an Amorphous MoS_3 Hydrogen-Generating Catalyst on a Quantum-Controlled Photosensitizer.
    M. L. Tang, D. C. Grauer, B. Lassalle-Kaiser, V. K. Yachandra, L. Amirav, J. R. Long, J. Yano and A. Paul Alivisatos.*
    Angewandte Chemie International Edition, **2011**, 50, 10203-10207. IF : 12.10

12. A High-Spin Iron(IV)−Oxo Complex Supported by a Trigonal Nonheme Pyrrolide Platform.
    J. P. Bigi, W. H. Harman, B. Lassalle-Kaiser, D. M. Robles, T. A. Stich, J. Yano, R. D. Britt, C. J. Chang.*
    Journal of the American Chemical Society, **2012**, 134, 1536-1542. IF : 14.35

13. Preparation and Properties of a Monomeric High-Spin MnV−Oxo Complex.
    T. Taguchi, R. Gupta, B. Lassalle-Kaiser, D. W. Boyce, V. K. Yachandra, W. B. Tolman, M. P. Hendrich, A.S. Borovik.*
    Journal of the American Chemical Society, **2012**, 134, 1996-1999. IF : 14.35

14. Structure–Activity Correlations in a Nickel–Borate Oxygen Evolution Catalyst.
    D. K. Bediako, B. Lassalle-Kaiser, Y. Surendranath, J. Yano, V. K. Yachandra, and D. G. Nocera.*
    Journal of the American Chemical Society, **2012**, 134, 15, 6801-6809. IF : 14.35

15. Room Temperature Femtosecond X-ray Diffraction of Photosystem II Microcrystals.
J. Kern, R. Alonso-Mori, J. Hellmich, R. Tran, J. Hattne, H. Laksmono, C. Glöckner, N. Echols, R. Sierra, J. Sellberg, B. Lassalle-Kaiser, R. J. Gildea, P. Glatzel, R. W. Grosse-Kunstleve, M. J. Latimer, T. A. McQueen, D. DiFiore, A. R. Fry, M. Messerschmidt, A. Miahnahri, D. W. Schafer, M. M. Seibert, D. Sokaras, T.-C. Weng, P. H. Zwart, W. E. White, P. D. Adams, M. J. Bogan, S. Boutet, G. J. Williams, J. Messinger, N. K. Sauter, A. Zouni, U. Bergmann*, J. Yano*, V. K. Yachandra.*
Proc. Nat. Acad. Sci. USA, **2012**, 109, 25, 9721-9726. IF : 9.50

16. Nanoflow Electrospinning Serial Femtosecond Crystallography.
R. G. Sierra, H. Laksmono, J. Kern, R. Tran, J. Hattne, R. Alonso-Mori, B. Lassalle-Kaiser, C. Glöckner, J. Hellmich, D. W. Schafer, N. Echols, R. J. Gildea, R. W. Grosse-Kunstleve, J. Sellberg, T. A. McQueen, A. R. Fry, M. M. Messerschmidt, A. Miahnahri, M. M. Seibert, C. Y. Hampton, D. Starodub, N. D. Loh, D. Sokaras, T.-C. Weng, P. H. Zwart, P. Glatzel, D. Milathianaki, W. E. White, P. D. Adams, G. J. Williams, S. Boutet, A. Zouni, J. Messinger, N. K. Sauter, U. Bergmann, J. Yano, V. K. Yachandra, M. J. Bogan.*
Acta Crystallographica, section D, **2012**, D68, 1584-1587. IF : 3.09

17. Energy-Dispersive X-ray Emission Spectroscopy Using an X-ray Free Electron Laser in a shot-by-shot mode.
R. Alonso-Mori, J. Kern, R. J. Gildea, D. Sokaras, T-C. Weng, B. Lassalle-Kaiser, R. Tran, J. Hattne, Hartawan Laksmono, J. Hellmich, C. Glöckner, N. Echols, R. G. Sierra, D. W. Schafer, J. Sellberg, C. Kenney, R. Herbst, J. Pines, P. Hart, S. Herrmann, R. W. Grosse-Kunstleve, M. J. Latimer, A. R. Fry, M. M. Messerschmidt, A. Miahnahri, M. M. Seibert, P. H. Zwart, W. E. White, P. D. Adams, M. J. Bogan, Boutet, G. J. Williams, A. Zouni, J. Messinger, P. Glatzel, N. Sauter, V. K. Yachandra*, J. Yano*, U. Bergmann.*
Proc. Nat. Acad. Sci. USA, **2012,** 109, 47, 19103-19107. IF : 9.81

18. Simultaneous Femtosecond X-ray Spectroscopy and Diffraction of Photosystem II at Room Temperature.
J. Kern, R. Alonso-Mori, R. Tran, J. Hattne, R. J. Gildea, N. Echols, C. Glöckner, J. Hellmich, H. Laksmono, R. G. Sierra, B. Lassalle-Kaiser, S. Koroidov, A. Lampe, G. Han, S. Gul, D. DiFiore, D. Milathianaki, A. R. Fry, A. Miahnahri, D. W. Schafer, M. Messerschmidt, M. M. Seibert, J. E. Koglin, D. Sokaras, T.-C. Weng, J. Sellberg, M. J. Latimer, R. W. Grosse-Kunstleve, P. H. Zwart, W. E. White, P. Glatzel, P. D. Adams, M. J. Bogan, G. J. Williams, S. Boutet, J. Messinger, A. Zouni, N. K. Sauter, V. K. Yachandra,* U. Bergmann* and J. Yano.*
Science, **2013**, 340, 6131, 491-495. IF : 32.45

19. In-situ X-Ray Absorption Spectroscopy Investigation of a Bifunctional Manganese Oxide Catalyst with High Activity for Electrochemical Water Oxidation and Oxygen Reduction.
Y. Gorlin, B. Lassalle-Kaiser, J. D. Benck, S. Gul, S. Webb, V. K. Yachandra, J. Yano*, T. Jaramillo.*
Journal of the American Chemical Society, **2013**, 135, 23, 8525-8534. IF : 14.35

20. L-Edge X-ray Absorption Spectroscopy of Dilute Systems Relevant to Metalloproteins Using an X-ray Free-Electron Laser.
R. Mitzner, J. Rehanek, J. Kern, S. Gul, J. Hattne, T. Taguchi, R. Alonso-Mori, R. Tran, C. Weniger, H. Schröder, W. Quevedo, H. Laksmono, R. G. Sierra, G. Han, B. Lassalle-Kaiser, S. Koroidov, K. Kubicek, S. Schreck, K. Kunnus, M. Brzhezinskaya, A. Firsov, M. P. Minitti, J. J. Turner, S. P. Moeller, N. K. Sauter, M. J. Bogan, D. Nordlund, W. F. Schlotter, J. Messinger, A. S. Borovik, S. A. Techert, F. M. F. de Groot, A. Foehlisch, A. Erko, U. Bergmann,* V. K. Yachandra,* P. Wernet* and Junko.*
Journal of Physical Chemistry Letters, **2013**, 4, 21, 3641-2647 IF : 8.70

21. Experimental and Computational X-ray Emission Spectroscopy as a Direct Probe of Protonation States in Oxo-Bridged MnIV-Dimers Relevant to Redox-active Metalloproteins.
B. Lassalle-Kaiser, T. T. Boron, III, V. Krewald, J. Kern, M. Beckwith, H. Schroeder, R. Alonso-Mori, D. Nordlund, T.-C. Weng, D. Sokaras, F. Neese, U. Bergmann, V. K. Yachandra, S. DeBeer*, V. L. Pecoraro*, J. Yano.*
Inorganic Chemistry, **2013**, 52, 22, 12915-12922 IF : 4.70

22. The Protonation States of Oxo-Bridged MnIV-Dimers Resolved by Experimental and Computational Mn K Pre-Edge X-Ray Absorption Spectroscopy.
V. Krewald, B. Lassalle-Kaiser, T. T. Boron, III, J. Kern, M. Beckwith, V. K. Yachandra, V. L. Pecoraro*, J. Yano*, F. Neese*, S. DeBeer.*
Inorganic Chemistry, **2013**, 52, 22, 12904-12914 IF : 4.70

23. Preparation and properties of a Mn^{IV}-OH complex: proton and electron transfer at a mononuclear manganese site and its relationship to the oxygen evolving complex within photosystem II.
T. Taguchi, K. L. Stone, R. Gupta, B. Lassalle-Kaiser, J. Yano, M. P. Hendrich and A. S. Borovik.*
Chemical Science, **2014**, 5, 3064. IF : 9.06

24. Accurate macromolecular structures using minimal measurements from X-ray free-electron lasers.
J. Hattne, N. Echols, R. Tran, J. Kern, R. J. Gildea, A. S. Brewster, R. Alonso-Mori, C. Glöckner, J. Hellmich, B. Lassalle-Kaiser, A. Lampe, G. Han, S. Gul, D. DiFiore, D. Milathianaki, A. R. Fry, A. Miahnahri, W. E. White, D. W. Schafer, M. M. Seibert, J. E. Koglin, D. Sokaras, T.-C. Weng, J. Sellberg, M. J. Latimer, P. Glatzel, P. H. Zwart, R. W. Grosse-Kunstleve, M. J. Bogan, M. Messerschmidt, G. J. Williams, S. Boutet, J. Messinger, A. Zouni, J. Yano, U. Bergmann, V. K. Yachandra, P. D. Adams & N. K. Sauter.*
Nature Methods, **2014**, 5, 545-548. IF : 26.91

25. Taking snapshots of photosynthetic water oxidation using femtosecond X-ray diffraction and spectroscopy.
J. Kern, R. Tran, R. Alonso-Mori, S. Koroidov, N. Echols, J. Hattne, M. Ibrahim, S. Gul, H. Laksmono, R. G. Sierra, R. J. Gildea, G. Han, J. Hellmich, B. Lassalle-Kaiser, R. Chatterjee, A. S. Brewster, C. A. Stan, C. Glöckner, A. Lampe, D. DiFiore,

D. Milathianaki, A. R. Fry, M. M. Seibert, J. E. Koglin, E. Gallo, J. Uhlig, D. Sokaras, T.-C. Weng, P. H. Zwart, D. E. Skinner, M. J. Bogan, M. Messerschmidt, P. Glatzel, G. J. Williams, S. Boutet, P. D. Adams, A. Zouni, J. Messinger, N. K. Sauter, U. Bergmann,* J. Yano* & V. K. Yachandra.*
Nature Communications, **2014**, 5, 4371. IF : 11.47

26. Evidence from in situ X-ray Absorption Spectroscopy for the Involvement of Terminal Disulfide in the Reduction of Protons by an Amorphous Molybdenum Sulfide Electrocatalyst.
B. Lassalle-Kaiser,* D. Merki, H. Vrubel, S. Gul, V. K. Yachandra, X. Hu* and J. Yano.*
Journal of the American Chemical Society, **2015**, 137, 1, 314-321. IF : 14.35

27. Simultaneous detection of electronic structure changes from two elements of a bifunctional catalyst using wavelength-dispersive X-ray emission spectroscopy and in situ electrochemistry.
S. Gul, J. W. D., Ng, R. Alonso-Mori, J. Kern, D. Sokaras, E. Anzenberg, B. Lassalle-Kaiser, Y. Gorlin, T. C. Weng, P. H. Zwart, J. Z. Zhang, U. Bergmann, V. K. Yachandra, T. F. Jaramillo* and J. Yano.*
Physical Chemistry Chemical Physics, **2015**, 17, 14, 8901-8912. IF : 3.90

28. High-spin Mn-oxo complexes and their relevance to the oxygen-evolving complex within photosystem II.
R. Gupta, T. Taguchi, B. Lassalle-Kaiser, E. L. Bominaar, J. Yano, M. P. Hendrich and A. S. Borovik.*
Proc. Nat. Acad. Sci. USA, **2015**, 112, 17, 5319-5324. IF : 9.50

29. X-ray Absorption spectroscopy using a self-seed soft X-ray free-electron laser
T. Kroll, J. Kern, M. Kubin, D. Ratner, S. Gul, F. D. Fuller, H. Löchel, J. Krzywinski, A. Lutman, Y. Ding, G. L. Dakovski, S. Moeller, J. J. Turner, R. Alonso-Mori, D. L. Nordlund, J. Rehanek, C. Weniger, A. Firsov, M. Brzhezinskaya, R. Chatterjee, B. Lassalle-Kaiser, R. G. Sierra, H. Laksmono, E. Hill, A. Borovik, A. Erko, A. Föhlisch, R. Mitzner, V. K. Yachandra, J. Yano, P. Wernet and U. Bergmann.*
Optics Express, **2016**, 24, 20, 22469-22480. IF : 3.35

30. Soft x-ray absorption spectroscopy of metalloproteins and high-valent metalcomplexes at room temperature using free-electron lasers.
M. Kubin, J. Kern, S. Gul, T. Kroll, R. Chatterjee, H. Löchel, F. D. Fuller, R. G. Sierra, W. Quevedo, C. Weniger, J. Rehanek, A. Firsov, H. Laksmono, C. Weninger, R. Alonso-Mori, D. L. Nordlund, B. Lassalle-Kaiser, J. M. Glownia, J. Krzywinski, S. Moeller, J. J. Turner, M. P. Minitti, G. L. Dakovski, S. Koroidov, A. Kawde, J. S. Kanady, E. Y. Tsui, S. Suseno, Z. Han, E. Hill, T. Taguchi, A. S. Borovik, T. Agapie, J. Messinger, A. Erko, A. Föhlisch, U. Bergmann, R Mitzner, V. K. Yachandra, J. Yano* and P. Wernet.*
Structural Dynamics, **2017**, 4, 054307, 1-15. IF: 3.96

31. *In situ/operando* Studies of Electrocatalysts Using Hard X-ray Spectroscopies.
B. Lassalle-Kaiser, S. Gul, J. Kern, V. K. Yachandra and J. Yano.*
Journal of electron spectroscopy and related Phenomena, **2017**, 221, 18-27.IF: 1.60

Publications at SOLEIL

Publications as local contact are marked with #

32. The GALAXIES beamline at the SOLEIL synchrotron: inelastic X-ray scattering and photoelectron spectroscopy in the hard X-ray range.
J.-P. Rueff,* J. M. Ablett, D. Céolin, D. Prieur, T. Moreno, V. Balédent, B. Lassalle-Kaiser, J. E. Rault, M. Simon and A. Shukla.
Journal of Synchrotron Radiation, **2015**, 22, 175-179. IF : 3.23

33. The LUCIA Beamline at SOLEIL.
D. Vantelon,* N. Trcera, D. Roy, T. Moreno, D. Mailly, S. Guilet, E. Metchalkov, F. Delmotte, B. Lassalle-Kaiser, P. Lagarde and A.-M. Flanck.
Journal of Synchrotron Radiation, **2016**, 23, 635-640. IF : 3.02

34. 1s3p resonant inelastic X-ray scaterring of cobalt oxides and sulfides
M. Al Samarai, M. U. Delgado-Jaime, H. Ishii, N. Hirakao, K.-D. Tsuei, J.–P. Rueff, B. Lassalle-Kaiser, B. M. Weckhuysen, F. M.F. de Groot.*
The Journal of Physical Chemistry – C, **2016**, 120, 24063-24069. IF : 4.50

35. Trace-Element Incorporation into Intracellular Pools Uncovers Calcium-Pathways in a Coccolithophore.
A. Gal, S. Sviben, R. Wirth, A. Schreiber, B. Lassalle-Kaiser, # D. Faivre, and A. Scheffel.*
Advanced Science, **2017**, 4, 1700088. 1-8. IF: 9.03

36. *In Situ* Observation of the Formation and Structure of Hydrogen-Evolving Amorphous Cobalt Electrocatalysts.
B. Lassalle-Kaiser,* A. Zitolo, E. Fonda, M. Robert, E. Anxolabéhère-Mallart.*
ACS Energy Letters, **2017**, 2, 2545-2551. IF: 12.27

37. Synthesis of Ce_2O_2S and $Gd_{2(1-y)}Ce_{2y}O_2S$ Nanoparticles and Reactivity from in Situ X‑ray Absorption Spectroscopy and X‑ray Photoelectron Spectroscopy.
C. Larquet, A.-M. Nguyen, M. Avila-Gutierrez, L. Tinat, B. Lassalle-Kaiser, J.-J. Gallet, F. Bournel, A. Gauzzi, C. Sanchez
and S. Carenco.*
Inorganic Chemistry, **2017**, 56, 14227-14236. IF: 4.70

38. Multiple Binding Modes of an Unconjugated Bis(pyridine) Ligand Stabilize Low-valent [Cp*Rh] Complexes.
D. Lionetti, V. W. Day, B. Lassalle-Kaiser* and J. D. Blakemore.*
Chemical Communications, **2018**, 54, 1694-1697. IF: 6.29

39. A fuly Noble Metal-Free Photosystem Based on Cobalt-Polyoxometalates Immobilized in a Porphyrinic Metal-Organic framework for Water Oxidation.
G. Paille, M. Gomez-Mingot, C. Roch-Marchal, B. Lassalle-Kaiser, P. Mialane, M. Fontecave,* C. Mellot-Draznieks* and A. Dolbecq.*
Journal of the American Chemical Society, **2018**, 140, 3613-3618. IF : 14.35

40. Interplay of Complex Decay Processes after Argon 1s Ionization.
R. Guillemin, K. Jankälä, B. C. de Miranda, T. Marin, L. Journel, T. Marchenko, O. travnikova, G. Goldsztejn, I. Ismail, R. Püttner, D. Ceolin, B. Lassalle-Kaiser, # M. N. Piancastelli and M. Simon.*
Physical Review A, **2018**, 97, **DOI:** 10.1103/PhysRevA.97.013418 IF: 2.90

41. Elucidating the performance and unexpected stability of partially coated water-splitting silicon photoanodes.
K. Oh, C. Meriadec, B. Lassalle-Kaiser, V. Dorcet, B. Fabre, S. Ababou-Girard, L. Joanny, F. Gouttefangeas and G. Loget.*
Energy and Environmental Science, **2018**, 11, 9, 2590-2599. IF : 30.07

42. The Hebeloma cylindrosporum HcPT2 Pi transporter plays a key role in ectomycorrhizal symbiosis.
A. Becquer, K. Garcia, L. Amenc, C. Rivard, J. Doré, C. Trives-Segura, W. Szponarski, S. Russet, Y. Baeza, B. Lassalle-Kaiser,# G. Gay, S. D. Zimmermann and C. Plassard.*
New Phytologist, **2018**. https://doi.org/10.1111/nph.15281 IF : 7.33

1.3.3 Communications

Invited seminars in conferences and laboratories

1. 2010, December 6, Paris, France: *Ecole Normale Supérieure de Paris, France: Laboratoire des biomolecules*.
Molecular models for the activation of water by manganese.

2. 2013, January 6, Toulouse, France*: Laboratoire de Chimie de Coordination*
X-ray spectroscopy as a tool for the study of water-splitting catalysts.

3. 2013, July 19, Strasbourg, France: *Laboratoire de bioélectrochimie et spectroscopie*.
X-ray spectroscopy as a tool for the study of water-splitting catalysts.

4. 2014, January 7, Orsay, France: *Institut de Chimie Moléculaire et des Matériaux d'Orsay*.
X-ray spectroscopy as a tool for the study of water-splitting catalysts.

5. 2015, January 23, Paris, France: *Laboratoire d'Electrochimie Moléculaire*.
X-ray spectroscopy of water-splitting catalysts.

6. 2016, March 11, Utrecht, the Netherlands: *Laboratory of Inorganic Chemistry and Catalysis*.
   In Situ X-ray spectroscopic investigation of oxygen and hydrogen evolving electrocatalysts.

7. 2017, May 24, Strasbourg, France: *E-MRS, ALTEC Symposium*
   Probing the local and electronic structure of nanomaterials at the solid-liquid interface.

8. 2018, February 6, Lawrence, Kansas, USA: *University of Kansas, Chemistry Department*.
   X-ray spectroscopy of Photosystem II and related mechanistic model compounds.

9. 2018, September 10, Didcot, United Kingdom: *Diamond Light Source upgrade workshop*.
   Microfluidic developments and applications at the SOLEIL Synchrotron.

Oral communications in conferences and meetings

10. 2007, September 21-22, Orsay, France: *Réunion annuelle de l'école doctorale de l'Université Paris-Sud*.
    Activation électrochimique d'une molécule d'eau coordonnée à un complexe de manganèse.
    B. Lassalle-Kaiser, A. Aukauloo, E. Anxolabéhère-Mallart

11. 2008, March 16-19, Fréjus, France: *Réunion annuelle du Club des Métaloprotéines et Modèles*.
    Activation électrochimique d'une molécule d'eau coordonnée à un complexe de manganèse.
    B. Lassalle-Kaiser, J. Yano, D. Pantazis, Y. Pushkar, C. Hureau, R. Guillot, F. Neese, V. K. Yachandra, E. Anxolabéhère-Mallart.

12. 2008, June 25-28, Camaret, France: *4th ECHEMS International Meeting*
    Activation of a water molecule: electrochemical preparation of a mononuclear Mn(IV)-O complex.
    B. Lassalle-Kaiser, C. Hureau, D. A. Pantazis, R. Guillot, V. K. Yachandra, F. Neese, J. Yano, E. Anxolabéhère-Mallart.

13. 2009, June 24-29, Strasbourg, France: *GECOM-CONCOORD*
    Spectroscopic and theoretical investigations of an electrochemically prepared mononuclear Mn(IV)-O complex.
    B. Lassalle-Kaiser, C. Hureau, D. A. Pantazis, R. Guillot, V. K. Yachandra, F. Neese, J. Yano, E. Anxolabéhère-Mallart.

14. 2010, January 7-10, Asilomar, California: 19th Western Photosynthesis Conference
    Electrochemical studies of Photosystem II – A photoelectrochemical approach.
    B. Lassalle-Kaiser, W. Leibl and A. W. Rutherford.

15. 2010, October 13-15 , Berkeley, California: *Advanced Light Source Users Meeting*
    X-ray spectroscopy of water oxidizing electrocatalysts.
    B. Lassalle-Kaiser, J. Kern, R. Tran, J. Yano, V. K. Yachandra

16. 2010, December 5-6, Autrans, France: *Réunion annuelle du Club des Métaloprotéines et Modèles*.
    Soft X-ray spectroscopy as a tool for the study of electrocatalysts.
    B. Lassalle-Kaiser, W-C. Wang, J-L. Chen, J. Guo, J. Yano, V. K. Yachandra

17. 2011, October 2-5, Berkeley, California: *Advanced Light Source Users Meeting*.
    Soft X-ray spectroscopy of water oxidizing electrocatalysts.
    B. Lassalle-Kaiser, J. Kern, H. Schroeder, R. Tran, J. Yano, V. K. Yachandra

18. 2012, January 7-10, Asilomar, California: *19th Western Photosynthesis Conference*.
    X-ray spectroscopic studies of water-splitting catalysts.
    B. Lassalle-Kaiser, J. Kern, R. Tran, S. Gul, R. Alonso Mori, U. Bergmann, J. Yano, V. K. Yachandra

19. 2013, July 8-11, Paris, France: *16èmes Journées d'électrochimie*
    In Situ analysis of electrocatalytic reactions by X-ray absorption spectroscopy.
    B. Lassalle-Kaiser, Y. Gorlin, J. Benck, S. Gul, V. K. Yachandra, J. Yano, T. Jaramillo

20. 2013, October 9-11, Lille, France: *Groupement de Recherche C(RS)2 Catalyse, Réactivité de Surface et Rayonnement Synchrotron*.
    In Situ X-ray absorption study of a water-oxidizing electrocatalyst.
    B. Lassalle-Kaiser, Y. Gorlin, J. D. Benck, S. Gul, V. K. Yachandra, T. F. Jaramillo, J. Yano.

21. 2014, January 19, Ventura, California: *Gordon Research Seminar on Renewable Energy: Solar Fuels*.
    In Situ X-ray Absorption Spectroscopy Investigation of a Bifunctional Water Oxidizing / Dioxygen Reducing Manganese Oxide Electrocatalyst.
    B. Lassalle-Kaiser, Y. Gorlin, J. Benck, S. Gul, V. K. Yachandra, J. Yano, T. Jaramillo

22. 2016, January 19, Saclay, France: *High Resolution Spectroscopy for Applied Research Workshop (HI-SPEAR)*.
    In situ detection of electronic structure changes in a bifunctional electrocatalyst using a wavelength-dispersive X-ray emission spectrometer.
    B. Lassalle-Kaiser, S. Gul, R. Alonso-Mori, D. SOkaras, J. Kern, Y. Gorlin, J. Benck, S. Gul, V. K. Yachandra, J. Yano, T. Jaramillo.

23. 2016, January 22, Saclay, France: *SOLEIL's Users Meeting*.
    In situ X-ray spectroscopic investigation of a hydrogen-evolving cobalt nanoelectrocatalyst.
    B. Lassalle-Kaiser, A. Zitolo, E. Fonda, M. Robert, E. Anxolabéhère-Mallart.

24. 2016, May 31, Strasbourg, France: *Annual meeting of the French Solar Fuels network*.
    Spectroscopic opportunities for Solar Fuels research at the synchrotron SOLEIL.
    B. Lassalle-Kaiser, A; Zitolo, F. Wien.

25. 2018, January 18, Saclay, France: *ivMX (in vivo Macromolecular Crystallography), SOLEIL's Users Meeting satellite workshop*.
    Trace element incorporation into intracellular pools uncovers calcium-pathways in a coccolithophore.
    B. Lassalle-Kaiser, A. Gal, S. Sviben, R. Wirth, A. Schreiber, D. Faivre and André Scheffel.

Poster communications

1. 2004, September 21-24, Carry-Le-Rouet, France: Réunion annuelle du Club des Métaloprotéines et Modèles.
   Synthèse et caractérisation de complexes de manganèse(II). Réactivité en oxydation.
   B. Lassalle-Kaiser, L. Sabater, C. Hureau, C. Philouze, F. Gonnet, G. Blain, G. Blondin, E. Anxolabéhère-Mallart.

2. 2005, June 5-10, Autrans, France : *GECOM-CONCOORD*.
   Synthèse et caractérisation d'un complexe de Ni^{II}. Modulation de son potentiel d'oxydation par déprotonation.
   B. Lassalle-Kaiser, R. Guillot and A. Aukauloo.

3. 2005, October 14-16, Carry-Le-Rouet, France: *Réunion annuelle du Club des Métaloprotéines et Modèles*.
   Modulation du potentiel d'oxydation d'un complexe de Ni^{II} par déprotonation.
   B. Lassalle-Kaiser, R. Guillot and A. Aukauloo.

4. 2006, July 2-7, Uppsala, Sweden: *International Conference on Conversion and Storage of Solar Energy*.
   Chemical models of the Fourth Manganese of the OEC.
   B. Lassalle-Kaiser, R. Guillot, C. Hureau, A. Aukauloo and E. Anxolabéhère-Mallart.

5. 2007, January 27 – February 1st, Ventura, California: *Gordon Research Conference Metals in Biology*.
   Electrochemical Access to an OxoManganese(IV) Complex ?
   B. Lassalle-Kaiser, R. Guillot, C. Hureau, A. Aukauloo and E. Anxolabéhère-Mallart.

6. 2007, April 23-24, London, UK: *Royal Society Discussion: Revealing how nature uses sunlight to split water*.
   Electrochemical Access to an OxoManganese(IV) Complex.
   B. Lassalle-Kaiser, R. Guillot, C. Hureau, A. Aukauloo and E. Anxolabéhère-Mallart.

7. 2011, January 25-30, Ventura, California: *Gordon Research Conference Renewable Energy: Solar Fuels*.
   Water Activation: Charge Compensation at a Mononuclear Mn(II) Complex.
   B. Lassalle-Kaiser, C. Hureau, R. Guillot, D. A. Pantazis, F. Neese, E. Anxolabehere-Mallart, J. Yano, and V. K. Yachandra.

8. 2012, March 20-22, Berkeley, California: *Young Engineers and Scientists Symposium*
   X-ray spectroscopy as a tool to study water-splitting catalysts.
   B. Lassalle-Kaiser, J. Kern, S. Gul, R. Tran, J. Yano, and V. K. Yachandra.

9. 2012, March 27-29, Mittelwihr, France: *Réunion annuelle du Club des Métaloprotéines et Modèles*.
   X-ray spectroscopy as a tool to study water-splitting catalysts.
   B. Lassalle-Kaiser, J. Kern, S. Gul, R. Tran, J. Yano, and V. K. Yachandra.

10. 2012, May 13-18 , Lucca, Italy: *Gordon Research Conference Renewable Energy: Solar Fuels*.
    X-ray spectroscopy as a tool to study water-splitting catalysts.
    B. Lassalle-Kaiser, J. Kern, S. Gul, R. Tran, J. Yano, and V. K. Yachandra.

11. 2014, January 21-24, Ventura, California: *Gordon Research Conference Renewable Energy: Solar Fuels*.
    In Situ X-ray Absorption Spectroscopy as a tool for the study of Water Oxidizing and Proton Reducing Electrocatalysts.
    B. Lassalle-Kaiser, Y. Gorlin, J. Benck, H. Vrubel, D. Merki, S. Gul, T. Jaramillo, X. Hu, V. K. Yachandra and J. Yano.

12. 2015, August 23-28, Karlsruhe, Germany: *16th XAFS conference*.
    Opportunities for Energy research at LUCIA: Probing the solid-liquid interface in the tender X-ray range.
    B. Lassalle-Kaiser, P. Lagarde, D. Roy, N. Trcera, D. Vantelon.

13. 2016, February 28-March 4, Lucca, Italy: *Gordon Research Conference on Renewable Energy: Solar Fuels*.
    Probing the role of sulfur in HER-active transition metal electrocatalysts.
    B. Lassalle-Kaiser and J. Imbao.

14. 2016, September 5-7, Berlin, Germany: *NanoGe Solar Fuels international conference*.
    On the formation and structure of HER-active cobalt nanoelectrocatalysts using operando X-ray absorption spectroscopy.
    B. Lassalle-Kaiser, A. Zitolo, E. Fonda, M. Robert, E. Anxolabéhère-Mallart.

15. 2018, Januray 28-February 2, Ventura, California: *Gordon Research Conference on Renewable Energy: Solar Fuels*.
    On the use of Operando X-ray spectroscopy for the study of electrocatalysts.
    B. Lassalle-Kaiser, M. Han, T.-H. C. Chan-Chang, C. Sanchez, D. Portehault, A. Zitolo, E. Fonda, M. Robert, E. Anxolabéhère-Mallart.

1.3.4 Peer-reviewing

- Research articles:
  - Journal of the American Chemical Society
  - Nature Materials
  - Nature Energy
  - Journal of Physical Chemistry Letters
  - ACS Applied Energy Materials
  - Journal of Synchrotron Radiation

- ANR international collaborative project (2018)

- SSRL proposals reviewing (2017-present)

1.4 Research funding and scientific activities

1.4.1 Funded projects as principal investigator at SOLEIL.

*: project coordinator

- 2016 collaborative ANR grant "In situ electrochemistry applied to energy-related catalysis" (InSiChem).
  Ovidiu Ersen,* Université de Strasbourg, Clément Sanchez, Collège de France / Université Pierre & Marie Curie and B. Lassalle (PI for SOLEIL).
  Allocated funds: 511 945 €

- 2017 collaborative ANR grant " Time-resolved cryo-EM studies of translation initation" (TREMTI).
  Yves Mechulam* and Thomas Simonson, Ecole Polytechnique, B. Lassalle (PI for SOLEIL).
  Allocated funds: 479 000 €

- 2018 Charmmmat LABEX post-doctoral grant "Heterobimetallic bioinspired complexes for the reduction of CO_2: synthesis, electrochemistry and spectroscopy"
  Zakaria Halime,* Université Paris-Sud and B. Lassalle (PI for SOLEIL).
  Allocated funds: 105 000 €

- 2018 SOLEIL Michem LABEX doctoral fellowship " Time-resolved X-ray spectroelectrochemistry for the detection of reaction intermediates in the reduction of CO_2 by iron porphyrins". (CO_2-TRIP)
  Marc Robert, Université Paris Diderot and B. Lassalle.*
  Allocated funds: 120 000 €

- 2018 Young investigator ANR grant "microfluidic devices for the sequential reduction of CO_2 into light hydrocarbons" (MF-CO_2)
  B. Lassalle.*
  Allocated funds: 237 600 €

1.4.2 Students training at SOLEIL

- 3 Undergraduate engineers:
  - *Jordan Priam, Sep. – July 2016 : Microfluidic trapping systems for serial crystallography.*
  - *Tiphaine Mateo, Sep. 2016 – present : Microfluidic systems for the sequential electrochemical reduction of CO2.*
  - *Baptiste Maurice, Sep. 2018 – present : Microfluidic systems for in vivo crystal detection using a second-harmonic generator microscope.*

- 2 Master students:
  - *Jerrick Imbao, Feb. – July 2015* : Synthesis and spectroscopic characterization of Mo_xS_y molecular clusters.
  - *Madeleine Han, Feb. – July 2017* : Synthesis and characterization of nano-sized cobalt spinels for electrocatalytic water-splitting (InSiChem project).
- 2 PhD students currently under supervision:
  - *Madeleine Han, Sep. 2017 – present* : Synthesis and characterization of nano-sized cobalt spinels for elcectrocatalytic water-splitting (InSiChem project).
  - *Daniela Mendoza, Oct. 2018 – present* : Time-resolved X-ray spectroscopic studies of CO_2-reducing iron porphyrin electrocatalysts. (CO_2-TRIP project).

- 2 Post-doc currently under supervision:
  - *Dr. Khaled Cheaib, Feb. 2018 – present* : Time-resolved X-ray spectroscopic studies of CO_2-reducing iron porphyrin electrocatalysts.
  - *Dr. YuanYuan Liao, Apr. 2018 – present* : development of microfluidic mixers and sprayers for the preparation of biological time-resolved cryo-EM samples. (TREMTI project)

1.4.3 Teaching activities

- 2014 – present : Lecture on the current trends in artificial photosynthesis.
  SERP+ Erasmus Mundus international master program, Université Paris-Sud, Orsay.
  5 hours / year

1.4.4 Organization of conferences and seminars

- 2012 : Co-chair (with Dr. Maria-Eirini Pandelia) for the *Gordon Research Seminar on Renewable Energy: Solar Fuels* in Lucca, Italy.

- 2012-2014 : Initiator and responsible of a student and post-doc monthly meting at SOLEIL.

- 2019 : Organization of the French Solar Fuels network annual meeting in SOLEIL.

1.4.5 Collaborations

- Since 2014 : Pr. Marc Robert and Dr. Elodie Anxolabéhère-Mallart
  Université Paris Diderot, Paris, France
  In situ/operando spectroscopy of energy-related electrocatalysts
  Publication n° 36 and Michem LABEX CO_2-TRIP project.

- Since 2015 : Drs. Cédric Tard, Jennifer Peron, Marion Giraud
  Université Paris Diderot / CNRS, Paris, France.
  Transition metal chalcogenide nanoparticles for hydrogen evolution electrocatalysis.

- Since 2016 : Drs. David Portehault, Sophie Carenco and Clément Sanchez.
  Université Pierre & Marie Curie / CNRS / Collège de France, Paris, France.
  Nanoparticles synthesis for energy research electrocatalysis.
  Publication n°37, manuscript in preparation and InSiChem ANR project.

- Since 2014 : Pr. Xile Hu
  Ecole Polytechnique Fédérale de Lausanne, Lausanne, Switzerland.
  Electrodeposition of transition metal catalytic materials
  Publication n°26, manuscript submitted.

- Since 2017: Pr. James D. Blakemore
  University fo Kansas, Lawrence, USA
  Spectroscopy of organometallic complexes.
  Publication n° 38

- Since 2017: Dr. Gabriel Loget
  Université de Rennes / CNRS, Rennes, France
  In situ/operando spectroscopy of nickel-based photoelectrocatalysts.
  Publication n° 41

- Since 2017: Dr. Zakaria Halime
  Université Paris-Sud / CNRS
  Time-resolved spectroscopy of CO_2-reducing macrocycles.
  Manuscript in preparation and Charmmmat LABEX project.

- Since 2017: Dr. Yves Mechulam
  Ecole Polytechnique, Palaiseau, France
  Microfluidic systems for time-resolved cryo-EM sample preparation.
  TREMTI ANR project

- Since 2018 : Pr. Gary F. Moore
  Arizona State University, Tempe, USA
  Operando spectroscopy of HER-active macrocycles.

1.4.6 Administrative duties at SOLEIL

- 2014-2016: Secretary for the Proposal Review Committee n°4 (chemistry and soft condensed matter)
- 2014-2015: Member of the panel for the reorganization of SOLEIL
- 2018: Member of the Safe and Sustainable Energy and Environment prospective panel for the Upgrade of SOLEIL
- 2016-present: Point of contact at SOLEIL for the French Solar Fuels network.

Annex III: Selected articles

Selected article no. 1 XX

Experimental and Computational X-ray Emission Spectroscopy as a Direct Probe of Protonation States in Oxo-Bridged MnIV-Dimers Relevant to Redox-active Metalloproteins.
B. Lassalle-Kaiser, T. T. Boron, III, V. Krewald, J. Kern, M. Beckwith, H. Schroeder, R. Alonso-Mori, D. Nordlund, T.-C. Weng, D. Sokaras, F. Neese, U. Bergmann, V. K. Yachandra, S. DeBeer*, V. L. Pecoraro*, J. Yano.*
Inorganic Chemistry, **2013**, 52, 22, 12915-12922

This paper was the first demonstration that X-ray emission valence-to-core spectra, together with DFT calculations, allows distinguishing between oxo, hydroxo and aquo bridging ligands in a dinuclear manganese complex. This demonstration has significant implications for the use of X-ray emission valence-to-core spectroscopy for the study of metalloenzymes and transition metal complexes.

Selected article no. 2 XXIX

Evidence from in situ X-ray Absorption Spectroscopy for the Involvement of Terminal Disulfide in the Reduction of Protons by an Amorphous Molybdenum Sulfide Electrocatalyst.
B. Lassalle-Kaiser,* D. Merki, H. Vrubel, S. Gul, V. K. Yachandra, X. Hu* and J. Yano.*
Journal of the American Chemical Society, **2015**, 137, 1, 314-321.

This paper has shown, using *in situ* and *operando* X-ray absorption spectroscopies, that amorphous molybdenum sulfide electrocatalysts reduce protons into hydrogen via terminal disulfide unit. The development and use of an *in situ* spectroelectrochemical cell in the tender X-ray range has proved instrumental in the measurement of molybdenum L and sulfur K-edge data.

Selected article no. 3 XXXVII

In Situ Observation of the Formation and Structure of Hydrogen-Evolving Amorphous Cobalt Electrocatalysts.
B. Lassalle-Kaiser,* A. Zitolo, E. Fonda, M. Robert, E. Anxolabéhère-Mallart.*
ACS Energy Letters, **2017**, 2, 2545-2551.

This article provides X-ray spectroscopic evidence for the decomposition of a molecular precursor into amorphous metallic cobalt, which is in turn active for the HER in aqueous conditions. We also showed that, even under highly reducing electrochemical potential, a layer of oxidized cobalt remains present at the solid-liquid interface.

Inorganic Chemistry

Article

pubs.acs.org/IC

Experimental and Computational X-ray Emission Spectroscopy as a Direct Probe of Protonation States in Oxo-Bridged Mn^{IV} Dimers Relevant to Redox-Active Metalloproteins

Benedikt Lassalle-Kaiser,[†] Thaddeus T. Boron III,[‡] Vera Krewald,[§] Jan Kern,[†,∥] Martha A. Beckwith,[§,⊥] Mario U. Delgado-Jaime,[§] Henning Schroeder,[†] Roberto Alonso-Mori,[∥] Dennis Nordlund,[∥] Tsu-Chien Weng,[∥] Dimosthenis Sokaras,[∥] Frank Neese,[§] Uwe Bergmann,[∥] Vittal K. Yachandra,[†] Serena DeBeer,*[,§,⊥] Vincent L. Pecoraro,*[,‡] and Junko Yano*[,†]

[†]Physical Biosciences Division, Lawrence Berkeley National Laboratory, Berkeley, California 94720, United States

[‡]Department of Chemistry, University of Michigan, Ann Arbor, Michigan 48109, United States

[§]Max Planck Institute for Chemical Energy Conversion, Stiftstrasse 34-36, 45470 Mülheim an der Ruhr, Germany

[∥]SLAC National Accelerator Laboratory, Menlo Park, California 94025, United States

[⊥]Department of Chemistry and Chemical Biology, Cornell University, Ithaca, New York 14853, United States

Supporting Information

ABSTRACT: The protonation state of oxo bridges in nature is of profound importance for a variety of enzymes, including the Mn_4CaO_5 cluster of photosystem II and the Mn_2O_2 cluster in Mn catalase. A set of dinuclear bis-μ-oxo-bridged Mn^{IV} complexes in different protonation states was studied by Kβ emission spectroscopy to form the foundation for unraveling the protonation states in the native complex. The valence-to-core regions (valence-to-core XES) of the spectra show significant changes in intensity and peak position upon protonation. DFT calculations were performed to simulate the valence-to-core XES spectra and to assign the spectral features to specific transitions. The K$\beta_{2,5}$ peaks arise primarily from the ligand 2p to Mn 1s transitions, with a characteristic low energy shoulder appearing upon oxo-bridge protonation. The satellite Kβ'' peak provides a more direct signature of the protonation state change, since the transitions originating from the 2s orbitals of protonated and unprotonated μ-oxo bridges dominate this spectral region. The energies of the Kβ'' features differ by ~3 eV and thus are well resolved in the experimental spectra. Additionally, our work explores the chemical resolution limits of the method, namely, whether a mixed (μ-O)(μ-OH_2) motif can be distinguished from a symmetric (μ-OH)$_2$ one. The results reported here highlight the sensitivity of Kβ valence-to-core XES to single protonation state changes of bridging ligands, and form the basis for further studies of oxo-bridged polymetallic complexes and metalloenzyme active sites. In a complementary paper, the results from X-ray absorption spectroscopy of the same Mn^{IV} dimer series are discussed.

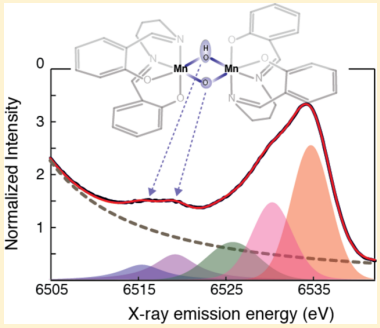

INTRODUCTION

Protonation states of oxo-bridging and terminal ligands (O^{2-}, OH^-, OH_2) often control catalytic function in inorganic and bioinorganic catalysts, by modulating the charge density distribution between the metals and ligands, the pK_a of bound water/hydroxide, and the covalency between metals and ligands. Examples of such systems include catalysts involved in O_2 association and dissociation reactions. In the hydrogen peroxide disproportionation reaction, catalyzed by Mn catalase, oxo bridges undergo protonation and deprotonation events that are essential to their physiological function, and certain protonation states are known to inhibit the catalytic reaction.[1,2] In the water-oxidation reaction catalyzed by the Mn_4CaO_5 cluster in photosystem II, protonation state changes in the bridging oxygen (μ-oxo or μ-hydroxo) and/or a terminal substrate water as aqua or hydroxo have been proposed during the four electron redox chemistry.[3−5]

More generally, protonation/deprotonation reactions of metal centers in biology are now recognized as important processes that moderate reaction chemistry. For example, copper oxo/hydroxo/peroxo complexes play vital roles in respiration, such as in hemocyanin,[6] in biological metabolic pathways such as catechol oxidase activity[7] or activation of aliphatic C−H bonds by dopamine β-monooxygenase, peptidylglycine α-amidating enzyme, and particulate methane monooxygenase.[8] Another important reaction is the reduction of ribonucleotides to the deoxy form in ribonucleotide reductase catalyzed by the FeFe or FeMn cluster, in which the O_2 activation by the FeMn cluster may be accompanied by the protonation state changes at the bridging oxygen.[9] It is also known that FeFe clusters in soluble methane monooxygenase

Received: April 3, 2013
Published: October 25, 2013

catalyze the hydroxylation of methane to methanol.[10−14] Understanding these events requires techniques that are sensitive enough to differentiate species that differ only by a single proton.

Numerous small molecule mimics exist in the literature for these biological systems.[15] Model compounds assessing the properties and reactivities of Mn^{IV}−OH and Mn^{IV}=O as well as Fe^{IV}−OH and Fe^{IV}=O species have been reported by several groups.[16−21] Que and co-workers have examined Fe complexes that are remarkable for their H-atom abstraction capabilities.[22,23] In some systems, it is possible to resolve the protonation state of oxo-bridged species through single-crystal X-ray crystallography[6] where unusually long or short M−O and M−OH bonds have been reported.[14,24] However, the chemical assignment of these unusual bond distances and associated protonation states is not always straightforward and could be further strengthened using a technique that has more direct sensitivity to the protonation event.

Several techniques have the potential to detect a single protonation event, while few of them can directly and selectively probe the protons in the first coordination sphere of a transition metal ion. Potential methods include vibrational spectroscopy[25] and ligand sensitive EPR techniques such as ENDOR (electron nuclear double resonance), ESEEM (electron spin echo envelope modulation), and HYSCORE (hyperfine sublevel correlation).[26,27] The advantage of X-ray-based methods over EPR techniques is their element specificity and that they are not restricted by the spin states of the compounds.

In two complementary papers[28] we explore the sensitivity of both X-ray absorption (XAS) and X-ray emission spectroscopy (XES) to changes in ligand protonation state. XAS can serve as an indirect probe of the protonation state through changes in local symmetry and metal−ligand bond distances at the catalytic site.[29] The assignment of protonation states by XAS is further strengthened by close correlation to theory, as explored in the preceding paper.[28]

XES is complementary to XAS and provides a direct probe of the filled molecular orbitals. In a Kβ XES spectrum, the "main line" features, K$\beta_{1,3}$ and Kβ', correspond to a transition from a metal 3p orbital to a metal 1s hole (Figure 1). Due to a strong contribution from 3p−3d exchange contribution, this region of the spectrum is dominantly influenced by the number of unpaired spins of the metal and hence its oxidation and/or spin state. To higher energy is the valence-to-core region (or also called K$\beta_{2,5}$ and Kβ'' features, Figure 1). These features correspond primarily to transitions from ligand 2p and 2s orbitals, respectively, and as such contain direct information about the ligand identities.[30−36]

In this work, the use of XES as a sensitive probe of single protonation events at bridging oxygen atoms is explored. A set of homologous dinuclear Mn^{IV} complexes that were initially synthesized by Baldwin et al.,[29] in which the protonation state of the bridging oxygen atoms was changed systematically, is used as a test set (see Figure 2, Chart 1). This series serves as a model system to study the nature of protonation state changes in oxo bridges. A combination of XES data and DFT calculations provides a detailed understanding of the origin of valence-to-core emission peaks, making XES an important tool to resolve protonation states of bridging oxygen atoms in biological catalysts. The technique also allows us to differentiate between two possible structures for the doubly protonated species, namely, a bis-μ-hydroxo vs a μ-oxo-μ-aqua bridged

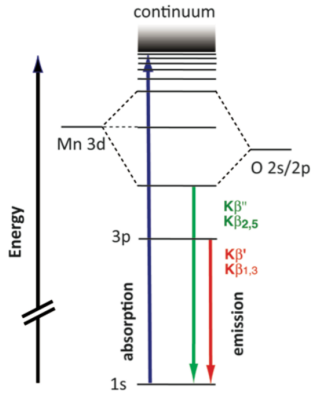

Figure 1. Energy diagram representing the X-ray absorption and emission preocesses at the K-edge of Mn. Blue arrow: absorption of a photon, exciting a 1s-electron into the continuum, leaving a 1s-hole. Green arrow: relaxation of ligand 2s/2p electron into the 1s-hole, emitting a photon in the Kβ'' or K$\beta_{2,5}$ energy range. Red arrow: relaxation of a metal 3p electron into the 1s-hole, emitting a photon in the Kβ' or K$\beta_{1,3}$ energy range.

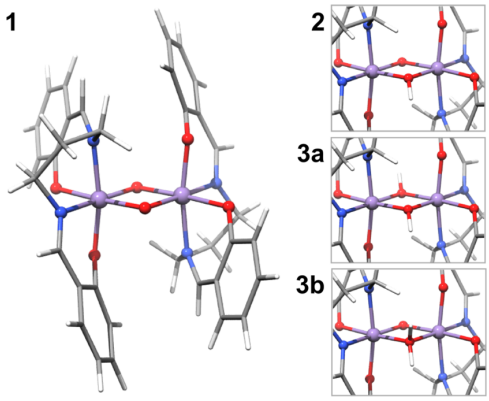

Figure 2. Fully optimized structure of **1** and details of the protonated cores of **2**, **3a** and **3b**. Color code for the atoms as follows: Mn purple, O red, N blue, C gray, H white.

Chart 1. Representation of the Dinuclear $[LMn^{IV}O]_2H_x$ (x = 0−2) Compounds, Their Total Charges and the Selected Core Bond Distances from DFT Geometry Optimization[28a]

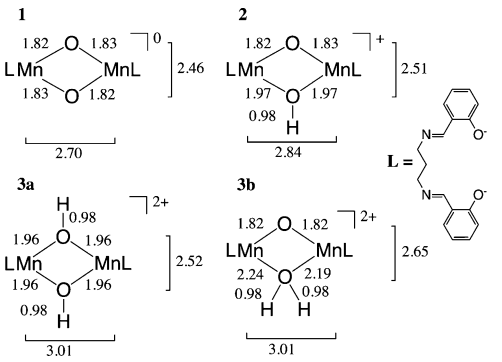

[a]L stands for the salpn ligand.[29] Comparison with EXAFS data[29] and bond angles are given in Chart S1 in the Supporting Information.

dx.doi.org/10.1021/ic400821g | Inorg. Chem. 2013, 52, 12915−12922

complex (Chart 1). Although a symmetric doubly protonated bridging motif is chemically more reasonable, we wish to explore the ability of valence-to-core XES and the accompanying DFT calculations to distinguish between these isomers. Such aquo units have been formulated recently as bridging motifs for the Mn_4CaO_5 core of the oxygen evolving complex (OEC).[37]

MATERIALS AND METHODS

XES Measurements. XES measurements were performed on beamline 6-2 at SSRL, with an operating ring current of 300 mA. The beamline monochromator, using two cryogenically cooled Si crystals in (111) reflection, was used to set the incident photon energy to 10.4 keV. The X-ray beam was focused to 0.6 (V) × 0.5 (H) mm (fwhm) by means of vertical and horizontal focusing mirrors. The X-ray flux at 10.4 keV was 3.0×10^{12} photons × s^{-1} × mm^{-2}. Multiple spots were used for collecting each XES spectrum, and the total amount of photons deposited on each sample spot was 2.7×10^{12} photons, which is below the threshold of radiation damage determined by XAS (ref 28). Samples were kept at a temperature of 10 K in a liquid helium flow cryostat.

Emission spectra were recorded by means of a high-resolution crystal-array spectrometer, using the 440 reflection of 14 spherically bent Si(110) crystals (100 mm diameter, 1 m radius of curvature), aligned on intersecting Rowland circles.[30] An energy-resolving Si drift detector (Vortex) was positioned at the focus of the 14 diffracting elements. A helium-filled polyethylene bag was placed between the cryostat and the spectrometer to minimize signal attenuation due to air absorption.

The fluorescence signal from the sample was divided by the incident flux (I_0), as monitored by a helium-filled ionization chamber. Spectra were calibrated using MnO as a reference. The first moments of the K$\beta_{1,3}$ and K$\beta_{2,5}$ peaks of a MnO spectrum were calibrated to 6491.00 and 6534.25 eV, respectively.[36] Data were collected at 10 K in a continuous flow liquid helium cryostat (Oxford Instruments CF1208) under helium exchange gas atmosphere.

Analysis of XES Spectra. The XES spectra were fit using the program BlueprintXAS.[38] For each compound, ~100 fits of the Kβ main line and valence to core regions were generated, and at least 90 reasonable fits were included for a statistically significant average (results are reported in Table 1, see Figure S2 in the Supporting Information for second derivatives). All of the emission spectra are normalized to a total integrated area of 1000. Reported experimental areas are based on the average of all good fits. Due to errors in normalization, background subtraction and fitting, a 10% error in the reported areas is estimated.[35] To appropriately and quantitatively compare the calculated XES spectra with the experimental data, the valence-to-core regions were analyzed in a comparable fashion, yielding intensity-weighted average energies (IWAE) and areas of fit or calculated peaks. The direct comparability of these parameters was established in ref 39. The reported experimental peak areas and IWAEs are those of the best-fit averages.

Table 1. Experimental and Calculated Intensity Weighted Average Energies (eV) and Areas for Total Valence-to-Core Regions[a]

	experiment		calculation	
calculation	area	IWAE (eV)	area	IWAE (eV)
1	45.40	6529.2	19.13	6530.8
2	41.28	6528.5	19.76	6530.6
3a	43.94	6528.7	18.70	6531.0
3b			18.28	6530.7

[a]Calculated areas correspond to the sums of the oscillator strengths of the predicted transitions and are multiplied with 1000, but otherwise unscaled. Calculated IWAEs are shifted by 59.2 eV.

Computation of XES Spectra. Valence-to-core X-ray emission spectra were calculated with the one-electron DFT approach implemented in the ORCA program package.[40] The geometries for these calculations were obtained from full relaxations of the crystal structure for compound **1**, with the correct number of protons added in the appropriate positions. These calculations used the BP86 functional[41,42] with the scalar-relativistically recontracted[43] Karlsruhe triple-ζ def2-TZVP(-f) basis set.[44] More details on the geometry optimization are given in ref 28. The method for calculating XES spectra has been published and tested.[35,36] The present paper follows the latter publication in correcting the molecular orbitals for spin–orbit coupling, with the spin–orbit mean-field approximation (SOMF) for the SOC operator.[44,45] The functional BP86 with def2-TZVP(-f) and def2-TZV/J basis sets and the conductor like screening model (COSMO[46]) for dichloromethane (ε = 9.08) was used here. The resulting computed spectra were energy-shifted by 59.2 eV to higher energy and broadened by 3.5 eV as discussed in ref 36. Additionally, the intensity of the calculated spectra was divided by two, since contributions from two donor sites are considered in the calculations, but the experimental normalization procedures result in spectra normalized to only one donor site. To understand the character of the calculated spectral features, it is sufficient to analyze the donor orbital character, since a one-electron picture was employed.

RESULTS AND DISCUSSION

When the $[Mn^{IV}(salpn)(O)]_2$ dimer was originally reported, X-ray crystal structures of the protonated species were not available.[29] The protonation states of the oxo bridges were inferred from IR and UV–visible spectroscopy as well as XAS techniques. Using the changes in Mn–ligand and Mn–Mn distances, it was deduced that the protonation of the oxo bridges proceeded from a bis-μ-oxo through a μ-oxo-μ-hydroxo and finally to a bis-μ-hydroxo complex. To test the sensitivity of valence-to-core XES to different types of oxo-bridge protonation patterns, not only a bis-μ-hydroxo complex was considered in the calculations but also a μ-oxo-μ-aquo species. With the complementary approaches of XES and XAS data (in the preceding paper[28]), combined with spectral calculations, it is possible to identify the protonation states of the bridges definitively as described below.

XES Spectra. The Kβ emission spectra consist of the Kβ' and K$\beta_{1,3}$ features, that together are called the main line, and the significantly less intense valence-to-core region at higher energy. The main line extends from 6472 to 6500 eV and is shown in Figure 3. There is a small shift of the K$\beta_{1,3}$ highest energy fit component maximum to higher energy upon

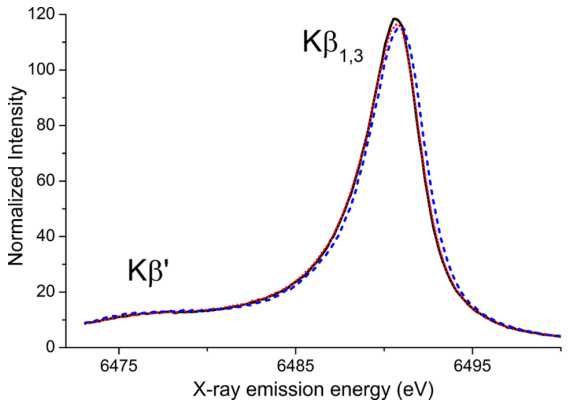

Figure 3. Main line of the X-ray emission spectra of compounds **1** (solid black), **2** (dotted red) and **3** (dashed blue).

dx.doi.org/10.1021/ic400821g | Inorg. Chem. 2013, 52, 12915–12922

protonation of the bridging oxygen atoms, however the magnitude is less than 0.25 eV and thus not sufficiently significant to correspond to changes in the Mn oxidation states. These small changes are consistent with the lack of XAS edge energy changes.[28] It was shown previously that the dominant factor increasing the K$\beta_{1,3}$ energy for Mn monomers is an increased 3p−3d exchange interaction.[36] Since the 3p−3d exchange interaction can be linked to covalency, it is worthwhile to consider the changes in covalency across the series. At each protonation step, the covalency of the Mn−O bonds in the core decreases: the bis-μ-O core is the most covalent and the bis-μ-OH core the least covalent. The decrease in covalency of the bridging motifs should increase the 3p−3d exchange interaction across the series, which may explain the slightly larger splitting of the Kβ' and K$\beta_{1,3}$ features upon protonation and hence the small shifts observed in the K$\beta_{1,3}$ features.

The valence-to-core XES region shows two characteristic peaks, the Kβ'' at 6511−6522 eV and the K$\beta_{2,5}$ at 6522−6540 eV (Figure 4a). Clear changes were observed for the three compounds with different protonation states (**1**−**3** in Chart 1): both K$\beta_{2,5}$ and Kβ'' features shift to lower energy upon protonation, accompanied by a decrease in peak intensity. For compounds **2** and **3**, a shoulder at the lower-energy side of the K$\beta_{2,5}$ peak grows in (~6530 eV). To emphasize the differences between the spectra for the three models, Figure S1 in the Supporting Information shows the difference spectra of **2** with **1** and **3** with **1**.

The fits to the XES data are composed of a background, which is the sum of the contributions from the Kβ main line features (Kβ' and K$\beta_{1,3}$), and four to six features in the valence-to-core region (see Figure 4b−d). The total areas and IWAEs from the fits are given in Table 1.

Kβ″ Region. The Kβ'' peaks are due to transitions from molecular orbitals of primarily ligand *n*s character. As ligand *n*s orbitals minimally participate in bonding with the metal, these features serve as excellent probes of ligand identity.[30−36] Focusing on the spectral shape in the 6511−6522 eV spectral range of Figure 4a, one can visually observe an intense and relatively narrow signal for compound **1** at 6519 eV (solid black), a less intense and broad signal for compound **2** between 6516 and 6519 eV (dotted red), and again a relatively narrow signal with the lowest intensity of the series for compound **3** at 6516 eV (dashed blue). The fits in this spectral region distinguish two peaks for compounds **1** and **2**, while for compound **3**, only a single peak component is observed (see Figure 4). For the bis-μ-O bridged complex **1**, the feature at higher energy has a smaller area than the one at lower energy. In compound **2**, there are two features at similar energies to those for compound **1**, but here the higher energy component is less intense while the lower energy component is of comparable intensity. In contrast, a single feature is observed for complex **3**, which has a lower intensity than the combined intensities of the two components in **1** and is shifted toward lower energies compared to the peaks with larger areas of compounds **1** and **2**.

For the three compounds, the ligands are either oxygen-based (bridging oxo and hydroxo, salpn O) or nitrogen-based (salpn N). The protonation of the oxo bridges has a larger influence on the equatorial Mn−O/N$_{salpn}$ bond lengths than on the axial metal−ligand distances: here, the change is 0.11 Å for O$_{salpn}$ and 0.10 Å for N$_{salpn}$ between **1** and **3a**. The axial bond lengths change much less (0.06 Å for O$_{salpn}$, 0.01 Å for N$_{salpn}$

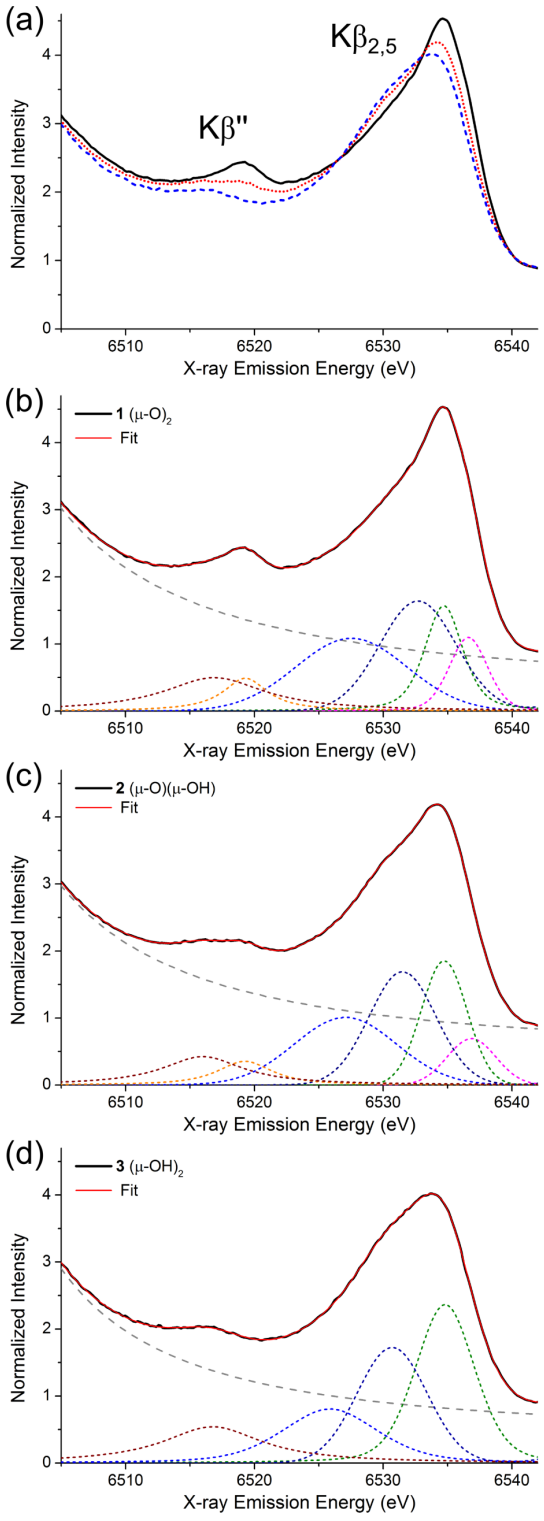

Figure 4. (a) Valence-to-core region of the X-ray emission spectra of compounds **1** (solid black), **2** (dotted red), and **3** (dashed blue). (b−d) Fits to the spectra of compounds **1**−**3**. Second derivatives of the background-subtracted normalized data are given as Figure S2 in the Supporting Information.

dx.doi.org/10.1021/ic400821g | *Inorg. Chem.* 2013, 52, 12915−12922

between **1** and **3a**). Since the equatorial distance changes are relatively large, one cannot necessarily expect the ligand contributions to be constant, but for extensive ligand systems, the contributions in the valence-to-core region are expected to be relatively small.[35,36] It can thus be expected that the fit component at higher energies is due to transitions from O_{bridge} 2s orbitals, whereas the one at lower energies is due to transitions from OH_{bridge} 2s and N/O_{salpn} 2s orbitals. We assign the spectra with the help of DFT calculations (*vide infra*).

Kβ$_{2,5}$ Region. Here, in the 6522–6540 eV energy range, the main change upon protonation is a systematic decrease in intensity of the main feature at ~6535 eV and a concomitantly increasing shoulder at its lower energy side, ~6530 eV. In the fits, the Kβ$_{2,5}$ region consists of three to four components (see Figure 4b–d). The intensity increase of the low energy shoulder with each protonation event is due to the decrease in the one or two components at highest energy and a shift of the components displayed in light and dark blue to lower energy. Thus, the whole Kβ$_{2,5}$ region becomes broader with successive protonation of the bridging oxo groups.

Upon protonation of the bridging oxygen atoms, the IWAE of the total valence-to-core region increases slightly, from 6529.2 eV (**1**: bis-μ-O) to 6528.5 eV (**2**: (μ-O)(μ-OH)) and to 6528.7 eV (**3**: bis-μ-OH). The peak areas change more significantly, from 45.40 (**1**: bis-μ-O) to 41.28 (**2**: (μ-O)(μ-OH)) and to 43.94 (**3**: bis-μ-OH).

Calculated XES. The calculated valence-to-core XES spectra for models **1**, **2**, **3a** and **3b** are shown in Figure 5,

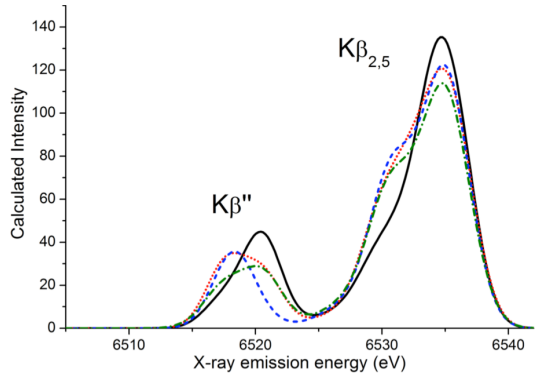

Figure 5. Calculated valence-to-core spectra of compounds **1** (solid black), **2** (dotted red), **3a** (dashed blue), and **3b** (dashed-dotted green). Calculated spectrum is shifted by 59.2 eV.

and the IWAEs and peak positions are summarized in Table 1. The general trends in both the Kβ″ (6511–6525 eV) and the Kβ$_{2,5}$ (6525–6540 eV) regions are well-reproduced. The Kβ″ feature in the calculated spectrum of compound **1** is located at the highest energy compared to the other features in the series (6520.4 eV, black in Figure 5) and is predicted to have an asymmetric narrow peak in agreement with experiment. The calculated spectrum of the doubly protonated species **3a** shows a similarly narrow but symmetric feature appearing at the lowest energy of this series (~6518.5 eV, blue in Figure 5), reproducing the experimental trend. Most importantly, the width of the Kβ″ peak of compound **2** is the broadest in this region, which is in excellent agreement with the experimental data. In fact, the broad calculated Kβ″ peak of compound **2** extends from the lower energy end of compound **3a** to nearly the higher energy end of compound **1**. This is also predicted to be the case for the spectrum of the putative complex **3b**. To higher energies, in the Kβ$_{2,5}$ region between 6524 and 6540 eV, the intensity of the main feature at ~6535 eV decreases upon protonation. Just as in the experimental spectra, the shoulder at ~6530 eV increases in intensity between the unprotonated and the protonated complexes.

Regarding the ability of XES to distinguish the symmetric (**3a,** dihydroxo) vs the asymmetric (**3b**, oxo-aqua) doubly protonated species, we note that the spectra of complexes **3a** and **3b** differ in the intensity distribution of the Kβ″ region. The spectrum of **3a** reproduces a narrow, intense feature shifted to lower energies compared to that of **1**, whereas the spectrum of **3b** is broad and of low intensity. Thus, the spectrum of **3a** yields a better match with experiment than that of **3b**. This is also in line with the calculated energetic and magnetic data for both structural proposals.[28]

The fact that the Kβ″ regions of **2** and **3** are clearly distinguished by experiment and the demonstration that models **2**, **3a**, and **3b** are computationally distinct give confidence in the ability of valence-to-core XES to differentiate not only between complexes in different protonation states (bis-μ-oxo, μ-oxo-μ-hydroxo, bis-μ-hydroxo) but also between complexes of the same nuclearity with different bridging motifs (bis-μ-hydroxo, μ-oxo-μ-aquo).

Assignments of the Kβ″ Region. Figure 6 shows the origin of the Kβ″ and Kβ$_{2,5}$ regions of the valence-to-core spectra, determined on the basis of the calculated spectra. The Kβ″ feature arises from electronic transitions from O and N 2s into Mn 1s orbitals. The O_{salpn} 2s and N_{salpn} 2s contributions appear at the same energies in all spectra, and thus can serve as reference points. For compound **1**, the transitions appear in the order O_{salpn} 2s, N_{salpn} 2s, O_{bridge} 2s from lower to higher energy, where the O_{bridge} 2s components are the most intense. The O_{bridge} 2s and O_{salpn} 2s transitions are separated by ~3 eV according to the calculations. Upon single protonation, yielding **2**, no energetic shifts are observed for transitions from the O_{bridge} 2s orbitals with respect to their positions in the spectrum of **1**, whereas the transitions from the single-protonated bridging oxygen atoms (OH_{bridge} 2s) are shifted into the energy region of the O_{salpn} 2s transitions. Inspection of the isosurfaces representing the donor orbitals of these transitions reveals that the orbitals have mixed O_{salpn} 2s/O_{bridge} 2s character (see Figure 7). The broad feature of the Kβ″ peak in compound **2** can thus be explained by the distinct energy separation of ~3 eV between the protonated and unprotonated oxo-bridge 2s orbitals. In the doubly protonated compound **3a**, the OH_{bridge} 2s components appear at energies between the O_{salpn} 2s and N_{salpn} 2s ones, their close energy levels making the Kβ″ feature appear as a single peak. For compound **3b**, the H_2O_{bridge} 2s components are found at energies lower than those of O_{salpn} 2s, which increases the asymmetry of the Kβ″ feature and broadens it relative to the peak of compound **3a**. The O_{bridge} 2s position is the same as those observed in the compounds **1** and **2**.

In short, the Kβ″ region of Mn^{IV} dimers with protonated or unprotonated oxo bridges can be attributed to transitions from O_{bridge} 2s, O_{salpn} 2s and N_{salpn} 2s orbitals. The energetic positions of the O_{bridge} 2s transitions shift by more than 3 eV upon protonation, significantly broadening the spectra. Regarding the relative intensities, the approximate order is calculated to be O_{bridge} 2s ≫ OH_{bridge} 2s > O_{salpn} 2s > N_{salpn} 2s ≫ H_2O_{bridge} 2s. The reason for the strong contribution of transitions from O_{bridge} 2s orbitals to the envelope intensity is

dx.doi.org/10.1021/ic400821g | *Inorg. Chem.* 2013, 52, 12915–12922

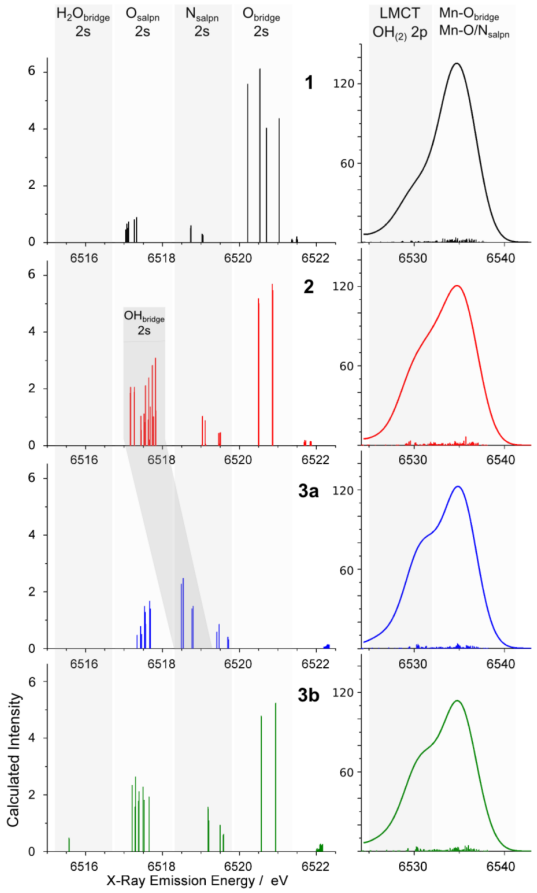

Figure 6. Assignments of the calculated XES valence-to-core region based on the orbital character corresponding to the individual transitions for compounds **1** (a), **2** (b), **3a** (c) and **3b** (d). The left side shows the Kβ'' region, and the right side shows the K$\beta_{2,5}$ region with different intensity scales. Gray areas where transitions of different donor orbital character appear; from left to right: H_2O_{bridge} 2s, O_{salpn} 2s, N_{salpn} 2s, O_{bridge} 2s in the left half; OH/OH_2 2p and LMCT, Mn–O/N_{salpn} and Mn–O_{bridge} in the right half. Transitions from orbitals with OH_{bridge} 2s character are found either in the O_{salpn} 2s region (mixed with O_{salpn} 2s character) or separately in the N_{salpn} 2s energy region (darkest gray). Representative donor orbitals for each of the spectral regions are shown in Figure 7.

attributed to the shorter Mn–O_{bridge} than Mn–O_{salpn} distances. Mn–O_{bridge} distances of 1.81–1.82 Å were obtained from the crystal structure in compound **1**, whereas Mn–O_{salpn} and Mn–N_{salpn} distances in this complex are much longer (1.91–1.93 Å and 2.00–2.06 Å, respectively). This trend is reproduced in the DFT calculations, where Mn–O_{bridge} distances of 1.82–1.83 Å and longer Mn–O_{salpn} and Mn–N_{salpn} distances (1.93–1.95 Å, 2.00–2.05 Å) were obtained for **1**.[28] Upon protonation of the bridging oxygen atoms, the Mn–OH_{bridge} distance is expected to increase to ~1.97 Å based on the DFT optimized geometry. The elongation of the bridging oxygen atoms upon protonation is consistent with the EXAFS results (for details, see the Supporting Information and the preceding XAS paper[28]). The Kβ'' components of these protonated oxo bridges have lower intensities due to the lower overlap of the donor with the acceptor orbitals, which is linked to the distance between donor site and acceptor site. Based on the distance argument only, one would then expect lower intensities for transitions originating from OH_{bridge} 2s orbitals than for those from O_{salpn} 2s orbitals (Mn–O distances of 1.97 Å and 1.84–1.87 Å in **3a**, respectively). The slightly higher intensities found in the calculations (Figure 6, **3a** panel) can be explained with the more localized O 2s character in ligands of smaller size,[48] leading to more intense transitions from the OH bridge than from the O atoms in the salpn ligand. For a bridging aquo ligand, the Mn–H_2O_{bridge} distance will be further elongated (~2.2 Å) and the donor orbital less localized, and indeed these transitions are computed to be the least intense (Figure 6, **3b** panel).

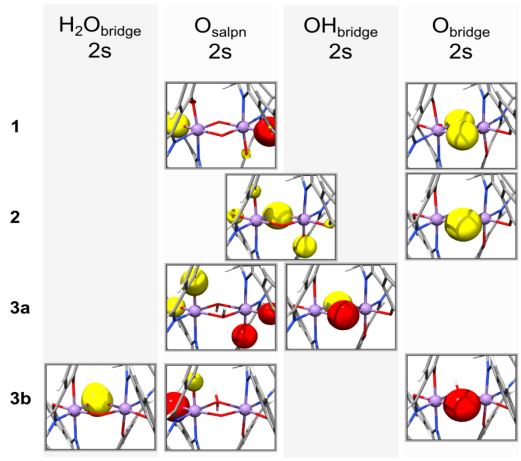

Figure 7. Representative donor orbitals corresponding to each of the assigned regions of the Kβ'' peak in Figure 6 (except "N_{salpn} 2s", instead "OH_{bridge} 2s" is shown in a separate panel); from top to bottom: bis-μ-oxo (**1**), μ-oxo-μ-hydroxo (**2**), bis-μ-hydroxo (**3a**), μ-oxo-μ-aquo (**3b**).

Assignments of the K$\beta_{2,5}$ Region. The calculated K$\beta_{2,5}$ main features of the three compounds exhibit no major energy shifts, whereas the decrease in peak intensity upon protonation is significant. In agreement with experiment, the area of the total K$\beta_{2,5}$ region shows little variation. In compound **1**, the shoulder at ~6530 eV originates from transitions of LMCT (ligand–metal charge transfer) character from the salpn ligand. The increase in the shoulder intensity in compounds **2** and **3** stems from additional transitions out of hydroxo-bridge orbitals of p-character, that fall into the same energy region. The most intense peak is largely due to transitions from Mn–O/N_{salpn} 2p and Mn–O_{bridge} 2p based molecular orbitals (see Figure 6).

Correlation of Experimental and Calculated Valence-to-Core Regions. Although, from visual inspection only, the agreement of calculation and experiment is good, it is worthwhile to quantify the agreement by correlating the experimental and calculated areas. The X-ray emission spectra are compared to a previously published set of monomer data that includes Mn(II) as well as Mn(III) and Mn(IV) data.[36] Figure 8 shows the correlation, where the trendline based on all data points is forced through 0 and follows $y = 0.477x$. The adjusted R value of 0.992 indicates good agreement between experiment and calculation. More details on the monomer data and the error bars are given in the Supporting Information.

Based solely on this correlation, it is not possible to discriminate between the bridging motifs of **3a** and **3b**. However, the differences in the Kβ'' intensity distributions in

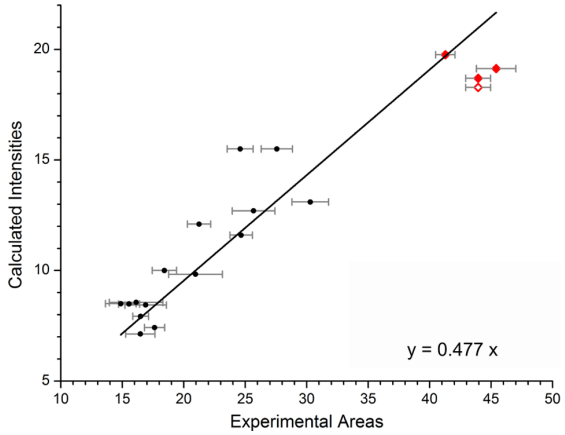

Figure 8. Correlation of experimental and calculated areas. Red diamonds correspond to the areas of the dimers; the unfilled red diamond corresponds to data for dimer **3b**. Monomer data are shown as black circles. The linear regression line is based on both the monomer and the dimer data and forced through 0. It follows the equation $y = 0.477x$ with an adjusted R value of 0.992.

the 6511−6522 eV spectral region clearly show that, for the symmetric compounds **1** and **3**, narrow signals at different energies are observed whereas, for the asymmetric compound **2**, a broad Kβ'' feature is observed. Thus, the envelopes help to understand the differences between the calculated spectra of **3a** and **3b** compared to the experimental one. For lower-resolution data, it is however crucial to make use of the complementarity of X-ray absorption and emission spectroscopy. As is presented in ref 28, the pre-edge areas for compound **3b** are clearly outside the correlation range.

CONCLUSION

In this study, we have demonstrated that XES valence to core spectra probe the ligand environment of metals with great sensitivity, including single protonation events. In particular, the Kβ'' satellite peaks can be used to discriminate among a set of three Mn^{IV} dimers in which the protonation states of bridging oxygen atoms are changed systematically. The limits of structure discrimination were further explored by comparison to calculated spectra for the two isomers $[Mn^{IV}_2(salpn)_2(\mu\text{-}OH)_2]^{2+}$ and $[Mn^{IV}_2(salpn)_2(\mu\text{-}OH)(\mu\text{-}OH_2)]^{2+}$. We find that even such fine differences can be reliably evaluated by DFT calculations, and given the size of these spectral changes they should also be experimentally observable. The application of these methods to metalloprotein active sites will certainly pose greater challenges. However, the observation of single light atoms from valence-to-core XES has already been demonstrated for both nitrogenase and the OEC.[32,33] The determination of more subtle changes, such as single protonation events within the OEC active site, may be addressed by utilizing difference spectra to highlight the changes between different S states. The Mn_4CaO_5 complex has a ligation sphere that may be composed of oxygen-derived ligands (including O^{2-}, OH^-, and/or H_2O), carboxylate ligands and histidine ligands. While all of these ligands will contribute to the K$\beta_{2,5}$ region of the spectrum, the most significant intensity in the Kβ'' region will derive from OH^- or O^{2-} ligands. As the present study shows, the changes between oxo and hydroxo groups should result in clear spectral changes, which may be highlighted by examining spectral differences. The observation of such (de)protonation events at manganese-bound oxo bridges should provide fundamental insights toward understanding of the catalytic cycle of the OEC, as well as other enzymes featuring dinuclear, high-valent manganese ions in their active sites, such as manganese RnR or manganese catalase.[2,47]

The assignments of the valence-to-core region show that the transitions of largest intensity in the Kβ'' region are due to transitions from the oxo-bridge 2s orbitals, which are significantly more intense than transitions from salpn-N/O 2s or hydroxo/aquo-bridge 2s orbitals. This is attributed to the shorter Mn−O distance and more localized donor orbital character in the unprotonated bridges, leading to larger overlap of donor and acceptor orbitals and hence more intense transitions. In the K$\beta_{2,5}$ region, a shoulder in the lower energy range is shown to be indicative of bridging hydroxo 2p contributions which are only present in protonated species, leading to increased intensity in this region across the series.

The data presented here demonstrate the exquisite chemical sensitivity of valence-to-core XES, which is further strengthened when combined with X-ray absorption spectroscopy.[28] Together these two techniques provide powerful element-specific tools to monitor changes in the ligand environment in metalloproteins, possibly during catalysis, by neglecting the overwhelming number of surrounding light atoms. A further challenge will be to detect protonation state changes that occur at terminal ligands in multinuclear complexes, and such studies are underway.

ASSOCIATED CONTENT

Supporting Information

Full geometry details (Chart S1). Experimental valence-to-core difference spectra (Figure S1). 2nd derivatives of the valence-to-core background-subtracted spectra (Figure S2). Examples of input files for XES calculations. Reference monomer data including standard deviations (Table S1). This material is available free of charge via the Internet at http://pubs.acs.org.

AUTHOR INFORMATION

Corresponding Authors

*E-mail: serena.debeer@cec.mpg.de.
*E-mail: vlpec@umich.edu.
*E-mail: jyano@lbl.gov.

Present Addresses

B.L.-K.: Synchroton SOLEIL, L'Orme des Merisier, BP 48 Saint-Aubin, 91192 Gif sur Yvette, France.
T.T.B.: Department of Chemistry, Slippery Rock University, 272 Advanced Technology and Science Hall #264, Slippery Rock, PA 16057, United States.
H.S.: Helmholtz-Zentrum Berlin für Materialien and Energie GmbH, Albert-Einstein-Strasse 15, 12489 Berlin, Germany. Institut für Physik and Astronomie, Universität Potsdam, Karl-Liebknecht-Strasse 24/25, 14476 Potsdam, Germany.

Author Contributions

B.L.-K., T.T.B., and V.K. contributed equally to the manuscript.

Notes

The authors declare no competing financial interest.

ACKNOWLEDGMENTS

This work was supported by the Director, Office of Science, Office of Basic Energy Sciences (OBES), Division of Chemical

Sciences, Geosciences, and Biosciences (CSGB) of the Department of Energy (DOE) under Contract DE-AC02-05CH11231 (J.Y. and V.K.Y.) for instrumentation development and NIH Grant GM 55302 (V.K.Y) for Mn inorganic chemistry. Experiments were carried out at Stanford Synchrotron Radiation Lightsource (SSRL), BL 6-2 in Stanford. SSRL is supported by DOE OBER. We thank the staff at SSRL for their support. V.K., M.A.B., S.D. and F.N. thank the Max Planck Society for funding. Also S.D. acknowledges Cornell University and the Alfred P. Sloan Foundation for fellowship. Christopher J. Pollock and Eleanor R. Hall are acknowledged for assistance with fits to the experimental spectra.

REFERENCES

(1) Whittaker, M. M.; Barynin, V. V.; Igarashi, T.; Whittaker, J. W. *Eur. J. Biochem.* **2003**, *270*, 1102−1116.
(2) Barynin, V. V.; Whittaker, M. M.; Antonyuk, S. V.; Lamzin, V. S.; Harrison, P. M.; Artymiuk, P. J.; Whittaker, J. W. *Structure* **2001**, *9*, 725−738.
(3) Sproviero, E. M.; Gascon, J. A.; McEvoy, J. P.; Brudvig, G. W.; Batista, V. S. *Coord. Chem. Rev.* **2008**, *252*, 395−415.
(4) Siegbahn, P. E. M. *Acc. Chem. Res.* **2009**, *42*, 1871−1880.
(5) Yamanaka, S.; Kanda, K.; Saito, T.; Umena, Y.; Kawakami, K.; Shen, J.-R.; Kamiya, N.; Okumura, M.; Nakamura, H.; Yamaguchi, K. In *Advances in Quantum Chemistry*; Elsevier: 2012; Vol. *64*, pp 121−187.
(6) Mahapatra, S.; Halfen, J. A.; Wilkinson, E. C.; Pan, G. F.; Wang, X. D.; Young, V. G.; Cramer, C. J.; Que, L.; Tolman, W. B. *J. Am. Chem. Soc.* **1996**, *118*, 11555−11574.
(7) Berreau, L. M.; Mahapatra, S.; Halfen, J. A.; Houser, R. P.; Young, V. G.; Tolman, W. B. *Angew. Chem., Int. Ed.* **1999**, *38*, 207−210.
(8) Mahapatra, S.; Halfen, J. A.; Wilkinson, E. C.; Que, L.; Tolman, W. B. *J. Am. Chem. Soc.* **1994**, *116*, 9785−9786.
(9) Bollinger, J. M.; Jiang, W.; Green, M. T.; Krebs, C. *Curr. Opin. Struct. Biol.* **2008**, *18*, 650−657.
(10) Lee, S. K.; Nesheim, J. C.; Lipscomb, J. D. *J. Biol. Chem.* **1993**, *268*, 21569−21577.
(11) Lee, S. K.; Fox, B. G.; Froland, W. A.; Lipscomb, J. D.; Munck, E. *J. Am. Chem. Soc.* **1993**, *115*, 6450−6451.
(12) Hsu, H. F.; Dong, Y. H.; Shu, L. J.; Young, V. G.; Que, L. *J. Am. Chem. Soc.* **1999**, *121*, 5230−5237.
(13) Stubna, A.; Jo, D. H.; Costas, M.; Brenessel, W. W.; Andres, H.; Bominaar, E. L.; Munck, E.; Que, L. *Inorg. Chem.* **2004**, *43*, 3067−3079.
(14) Kryatov, S. V.; Taktak, S.; Korendovych, I. V.; Rybak-Akimova, E. V.; Kaizer, J.; Torelli, S.; Shan, X. P.; Mandal, S.; MacMurdo, V. L.; Payeras, A. M. I.; Que, L. *Inorg. Chem.* **2005**, *44*, 85−99.
(15) Mukhopadhyay, S.; Mandal, S. K.; Bhaduri, S.; Armstrong, W. H. *Chem. Rev.* **2004**, *104*, 3981−4026.
(16) Parsell, T. H.; Behan, R. K.; Green, M. T.; Hendrich, M. P.; Borovik, A. S. *J. Am. Chem. Soc.* **2006**, *128*, 8728−8729.
(17) Yin, G.; Danby, A. M.; Kitko, D.; Carter, J. D.; Scheper, W. M.; Busch, D. H. *J. Am. Chem. Soc.* **2008**, *130*, 16245−16253.
(18) Lassalle-Kaiser, B.; Hureau, C.; Pantazis, D. A.; Pushkar, Y.; Guillot, R.; Yachandra, V. K.; Yano, J.; Neese, F.; Anxolabehere-Mallart, E. *Energy Environ. Sci.* **2010**, *3*, 924−938.
(19) Martinho, M.; Banse, F.; Bartoli, J.-F.; Mattioli, T. A.; Battioni, P.; Horner, O.; Bourcier, S.; Girerd, J.-J. *Inorg. Chem.* **2005**, *44*, 9592−9596.
(20) Bigi, J. P.; Harman, W. H.; Lassalle-Kaiser, B.; Robles, D. M.; Stich, T. A.; Yano, J.; Britt, R. D.; Chang, C. J. *J. Am. Chem. Soc.* **2012**, *134*, 1536−1542.
(21) Yin, G. C.; Danby, A. M.; Kitko, D.; Carter, J. D.; Scheper, W. M.; Busch, D. H. *J. Am. Chem. Soc.* **2007**, *129*, 1512−1513.
(22) Fiedler, A. T.; Que, L. *Inorg. Chem.* **2009**, *48*, 11038−11047.
(23) Jensen, M. P.; Costas, M.; Ho, R. Y. N.; Kaizer, J.; Payeras, A. M. I.; Munck, E.; Que, L.; Rohde, J. U.; Stubna, A. *J. Am. Chem. Soc.* **2005**, *127*, 10512−10525.
(24) MacMurdo, V. L.; Zheng, H.; Que, L. *Inorg. Chem.* **2000**, *39*, 2254−2255.
(25) Noguchi, T. *Philos. Trans. R. Soc., B* **2008**, *363*, 1189−1194.
(26) Milikisiyants, S.; Chatterjee, R.; Lakshmi, K. V. *J. Phys. Chem. B* **2011**, *115*, 12220−12229.
(27) Su, J. H.; Cox, N.; Ames, W.; Pantazis, D. A.; Rapatskiy, L.; Lohmiller, T.; Kulik, L. V.; Dorlet, P.; Rutherford, A. W.; Neese, F.; Boussac, A.; Lubitz, W.; Messinger, J. *Biochim. Biophys. Acta, Bioenerg.* **2011**, *1807*, 829−840.
(28) Krewald, V.; Lassalle-Kaiser, B.; Boron, T. T., III; Pollock, C. J.; Kern, J.; Beckwith, M. A.; Yachandra, V. K.; Pecoraro, V. L.; Yano, J.; Neese, F.; DeBeer, S. *Inorg. Chem.* **2013**, DOI: 10.1021/ic4008203.
(29) Baldwin, M. J.; Stemmler, T. L.; Riggs-Gelasco, P. J.; Kirk, M. L.; Penner-Hahn, J. E.; Pecoraro, V. L. *J. Am. Chem. Soc.* **1994**, *116*, 11349−11356.
(30) Glatzel, P.; Bergmann, U. *Coord. Chem. Rev.* **2005**, *249*, 65−95.
(31) Bergmann, U.; Bendix, J.; Glatzel, P.; Gray, H. B.; Cramer, S. P. *J. Chem. Phys.* **2002**, *116*, 2011−2015.
(32) Pushkar, Y.; Long, X.; Glatzel, P.; Brudvig, G. W.; Dismukes, G. C.; Collins, T. J.; Yachandra, V. K.; Yano, J.; Bergmann, U. *Angew. Chem., Int. Ed.* **2010**, *49*, 800−803.
(33) Lancaster, K. M.; Roemelt, M.; Ettenhuber, P.; Hu, Y. L.; Ribbe, M. W.; Neese, F.; Bergmann, U.; DeBeer, S. *Science* **2011**, *334*, 974−977.
(34) Smolentsev, G.; Soldatov, A. V.; Messinger, J.; Merz, K.; Weyhermuller, T.; Bergmann, U.; Pushkar, Y.; Yano, J.; Yachandra, V. K.; Glatzel, P. *J. Am. Chem. Soc.* **2009**, *131*, 13161−13167.
(35) Lee, N.; Petrenko, T.; Bergmann, U.; Neese, F.; DeBeer, S. *J. Am. Chem. Soc.* **2010**, *132*, 9715−9727.
(36) Beckwith, M. A.; Roemelt, M.; Collomb, M. N.; DuBoc, C.; Weng, T. C.; Bergmann, U.; Glatzel, P.; Neese, F.; DeBeer, S. *Inorg. Chem.* **2011**, *50*, 8397−8409.
(37) Gatt, P.; Petrie, S.; Stranger, R.; Pace, R. J. *Angew. Chem.* **2012**, *124*, 12191−12194.
(38) Delgado-Jaime, M. U.; Mewis, C. P.; Kennepohl, P. *J. Synchrotron Radiat.* **2010**, *17*, 132−137.
(39) DeBeer George, S.; Petrenko, T.; Neese, F. *J. Phys. Chem. A* **2008**, *112*, 12936−12943.
(40) Neese, F. In *ORCA program*; Version 2.8; Univ. Bonn.
(41) Becke, A. D. *Phys Rev A* **1988**, *38*, 3098−3100.
(42) Perdew, J. P. *Phys. Rev. B* **1986**, *33*, 8822−8824.
(43) Pantazis, D. A.; Chen, X. Y.; Landis, C. R.; Neese, F. *J. Chem. Theory Comput.* **2008**, *4*, 908−919.
(44) Weigend, F.; Ahlrichs, R. *Phys. Chem. Chem. Phys.* **2005**, *7*, 3297−3305.
(45) Hess, B. A.; Marian, C. M.; Wahlgren, U.; Gropen, O. *Chem. Phys. Lett.* **1996**, *251*, 365−371.
(46) Klamt, A.; Schüürmann, G. *J. Chem. Soc., Perkin Trans.* **1993**, *2*, 799−805.
(47) Tomter, A. B.; Zoppellaro, G.; Andersen, N. H.; Hersleth, H.-P.; Hammerstad, M.; Røhr, Å. K.; Sandvik, G. K.; Strand, K. R.; Nilsson, G. E.; Bell, C. B., III; Barra, A.-L.; Blasco, E.; Le Pape, L.; Solomon, E. I.; Andersson, K. K. *Coord. Chem. Rev.* **2013**, *257*, 3−26.
(48) Pollock, C. J.; DeBeer, S. *J. Am. Chem. Soc.* **2011**, *133*, 5594−5601.

JACS
JOURNAL OF THE AMERICAN CHEMICAL SOCIETY

Article

pubs.acs.org/JACS

Evidence from *in Situ* X-ray Absorption Spectroscopy for the Involvement of Terminal Disulfide in the Reduction of Protons by an Amorphous Molybdenum Sulfide Electrocatalyst

Benedikt Lassalle-Kaiser,*[,‡,§] Daniel Merki,[†] Heron Vrubel,[†] Sheraz Gul,[‡] Vittal K. Yachandra,[‡] Xile Hu,*[,†] and Junko Yano*[,‡]

[‡]Physical Biosciences Division, Lawrence Berkeley National Laboratory, Berkeley, California 94720, United States

[§]Synchrotron SOLEIL, L'Orme des Merisiers, Saint-Aubin, 91191 Gif-sur-Yvette, France

[†]Laboratory of Inorganic Synthesis and Catalysis, Institute of Chemical Sciences and Engineering, Ecole Polytechnique Fédérale de Lausanne (EPFL), EPFL-ISIC-LSCI, BCH 3305, Lausanne, CH 1015, Switzerland

Supporting Information

ABSTRACT: The reduction of protons into dihydrogen is important because of its potential use in a wide range of energy applications. The preparation of efficient and cheap catalysts for this reaction is one of the issues that need to be tackled to allow the widespread use of hydrogen as an energy carrier. In this paper, we report the study of an amorphous molybdenum sulfide (MoS_x) proton reducing electrocatalyst under functional conditions, using *in situ* X-ray absorption spectroscopy. We probed the local and electronic structures of both the molybdenum and sulfur elements for the as prepared material as well as the precatalytic and catalytic states. The as prepared material is very similar to MoS_3 and remains unmodified under functional conditions (pH = 2 aqueous HNO_3) in the precatalytic state (+0.3 V vs RHE). In its catalytic state (−0.3 V vs RHE), the film is reduced to an amorphous form of MoS_2 and shows spectroscopic features that indicate the presence of terminal disulfide units. These units are formed concomitantly with the release of hydrogen, and we suggest that the rate-limiting step of the HER is the reduction and protonation of these disulfide units. These results show the implication of terminal disulfide chemical motifs into HER driven by transition-metal sulfides and provide insight into their reaction mechanism.

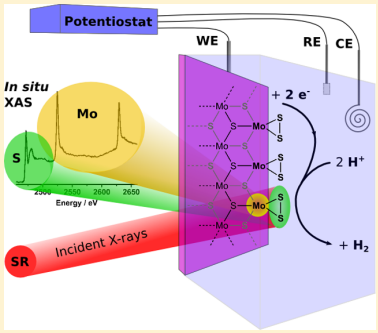

1.0. INTRODUCTION

One of the most important challenges many societies are currently facing is the supply of fuel for their increasing energy needs.[1,2] The extensive use of fossil fuels during the past century is reaching its limits, mostly because of the deleterious effects their combustion is causing to the environment. In this context, the search for alternative energy sources is of critical significance. Among various solutions, solar light is very important, because of its accessibility in most parts of the globe and the power it delivers on the surface of the earth. It is, however, only available during a certain portion of the day and in some places during certain times of the year. An optimal use of this energy source therefore requires its efficient storage. A very promising energy carrier that is able to fulfill this role is hydrogen.[3] A tremendous amount of work has been carried out in the past decades to develop systems capable of sustainably producing hydrogen from water electrolysis.[4−8] A class of compounds that meets both the technical and economical requirements of large-scale hydrogen production is molybdenum sulfides (MoS_x).[9] These inorganic materials have been extensively studied and used as natural gas hydrodesulfurization (HDS) catalysts.[10,11] More recently, they have been shown to catalyze the hydrogen evolution reaction (HER) in their molecular,[12−14] nanoparticulate[15−18] and amorphous[13,19−21] forms. In particular, some of us have reported on the preparation of electrodeposited amorphous MoS_x thin films that are catalytically active for the reduction of protons into hydrogen in acidic water.[19] These films have been extensively studied by X-ray photoelectron spectroscopy (XPS) to determine their electronic structure.[22] Although very informative, this technique only probes the very first nanometers of a surface and is very difficult to perform under functional conditions. In the current paper, we investigate the structure of an amorphous, HER-active MoS_x film observed under catalytic conditions using *in situ* X-ray spectroscopic techniques. An *in situ* electrochemical cell was developed and applied in the tender X-ray energy region (∼2−3 keV) to the study of an MoS_x HER catalyst under functional conditions. This method allowed us to probe the local and electronic structure of the molybdenum centers and sulfur ligands of the film under precatalytic and catalytic conditions. By comparing the data obtained on the catalytic film poised at constant potentials with those of reference compounds (see Table 1), we propose a

Received: October 15, 2014
Published: November 26, 2014

dx.doi.org/10.1021/ja510328m | J. Am. Chem. Soc. 2015, 137, 314−321

Table 1. Formal Oxidation States, Sulfur Chemical Units, and Structure of the MoS_x Reference Compounds Used in This Study

Sample	Formal oxidation states Mo	Formal oxidation states S	Sulfur chemical motifs	Structure[a]
$[Mo_3S_4]^{4+}$	Mo^{IV}	S^{-II}	μ-η^3 S^{2-}, μ-η^2 S^{2-}	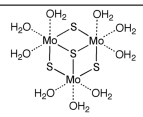
MoS_2	Mo^{IV}	S^{-II}	μ-η^3 S^{2-}	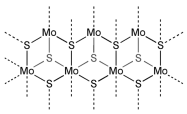
MoS_3[b]	Mo^{V}	S^{-II}, S^{-I}	μ-η^2 S^{2-}, μ-η^2:η^2 S_2^{2-}	
MoS_3[c]	Mo^{IV}	S^{-II}, S^{-I}	μ-η^2 S^{2-}, μ-η^3 S^{2-} μ-η^2:η^2 S_2^{2-}, η^2 S_2^{2-}	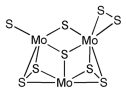
Chemical motif				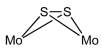
Name	μ-η^2 S^{2-}	μ-η^3 S^{2-}	η^2 S_2^{2-}	μ-η^2:η^2 S_2^{2-}

[a]The structures of $[Mo_3S_4(OH_2)_9]^{4+}$ and MoS_2 have been determined previously by XRD. [b]Structural and electronic information according to the model of Hibble et al.[24] [c]Structural and electronic information according to the model of Weber et al.[25] Only one structural model out of four possible is shown here. For more structural models see ref 25.

structural model for the catalyst film as prepared and under functional conditions in its precatalytic and catalytic states. The results provide evidence for the presence of terminal disulfide units in the MoS_x film and demonstrate their involvement in the catalytic cycle. Although the role of disulfide units in the reduction of protons into dihydrogen by MoS_x materials has often been suggested,[16,23] it is, to the best of our knowledge, the first time that this chemical motif is experimentally observed during the HER. We also suggest on a spectroscopic basis that the rate-limiting step of the reaction is the reductive breaking of the S–S bond. These mechanistic insights will be important in designing hydrogen-evolving catalysts with better performances.

2.0. EXPERIMENTAL SECTION

2.1. Model Compounds. HNO_3 (90%), MoS_2 (99%), $MoS_4(NH_4)_2$ (>99.9%), and $NaClO_4$ (>98%) were purchased from Aldrich, and $MoS_3{\cdot}2H_2O$ was purchased from Alfa-Aesar. $[Mo_3S_4(H_2O)_9]Cl_4$ was synthesized according to a published procedure.[26] All compounds were used as received without further purification. Deionized water was used for all experiments.

2.2. Electrodeposition of MoS_x Electrocatalyst. Prior to electrodeposition of the MoS_x catalyst film, a 500 nm thick silicon nitride (Si_3N_4, purchased from Silson Ltd.) membrane was sputter coated with a 150 nm layer of indium-doped tin oxide (ITO) to produce a suitable X-ray transparent conductive surface. The ITO surface was connected from the front with copper tape to ensure electrical contact. The deposition of MoS_x was carried out in a glovebox under nitrogen. The ITO electrode was immersed into a 2 mM solution of $(NH_4)_2MoS_4$ in 0.1 M $NaClO_4$ in water (8 mL). Consecutive cyclic voltammograms (typically 25) were carried out using an Ivium Stat potentiostat (Ivium Technologies) with a saturated silver/silver chloride reference electrode (separated by a porous Vycor tip) and a titanium wire counter electrode. The cyclic voltammograms were performed between +0.7 and −0.4 V vs reversible hydrogen electrode (RHE) and a scan rate of 0.05 V/s was employed. The modified electrode was rinsed with distilled water.

2.3. X-ray Absorption Data Collection. X-ray absorption data were collected at the Stanford Synchrotron Radiation Lightsource (SSRL) on beamline 7-3 (Mo K-edge) and 4-3 (S K-edge and Mo L-edge) at an electron energy of 3.0 GeV with an average current of 300 mA. At beamline 7-3, the radiation was monochromatized by a Si(220) double-crystal monochromator. The intensity of the incident X-ray was monitored by an Ar-filled ion chamber (I_0) in front of the sample. Solid samples were diluted in boron nitride (1% w/w) and placed in an aluminum sample holder sealed with kapton tape. Data were collected as fluorescence excitation spectra with a Ge 30 element detector (Canberra). Energy was calibrated by the first peak maximum of the first derivative of a molybdenum foil (20003.9 eV), placed between two Ar-filled ionization chambers (I_1 and I_2) after the sample. All data were collected at room temperature. At beamline 4-3, the incoming X-rays were monochromatized by a Si(111) double-crystal monochromator. The intensity of the incident X-rays was monitored by a He-filled ion chamber (I_0) in front of the sample. Solid sample spectra were collected from a thin layer of the sample smeared on sulfur-free tape. Data were collected as fluorescence excitation spectra with a Vortex 4 element silicon drift detector (SII NanoTechnology). Monochromator energy was calibrated to the first peak of thiosulfate reference sample, which was assigned at 2470.8 eV. The sample environment was kept under He gas atmosphere with an He-filled bag to reduce air absorption of incoming X-rays and fluorescence signals. The data were collected at room temperature. Additional data on reference samples were also collected at the LUCIA Beam line at SOLEIL, at an electron energy of 2.7 GeV and an average ring current of 430 mA. The incoming photons were selected with a Si (111) double crystal monochromator. Samples were compressed as pellets in 1:10 (w/w) mixture with cellulose and fixed on a copper sample holder with conductive carbon tape. The S K-edge and Mo L-edges were measured as fluorescence spectra with a grazing angle (<2°) for the outgoing photons in order to avoid self-absorption phenomena. Energy ranges for the first moment calculation are as follow: S K-edge: 2465–2475 eV; Mo L_3-edge: 2520–2535 eV; Mo L_2-edge: 2623–2640 eV.

2.4. *In Situ* Electrochemical XAS Measurements. A glass electrochemical cell consisting of two compartments separated by a porous frit was employed for *in situ* spectroscopic experiments, as previously reported.[27,28] The working compartment has flat walls (~1.5 cm wide) with a single circular hole of 0.8 cm in diameter. An MoS_x-coated ITO/Si_3N_4 membrane as described above was in contact with a slip of copper tape and fixed with epoxy glue to the exterior of the wall of the cell, over the 0.8 cm hole, with the MoS_x layer facing inward. A nitric acid solution adjusted to pH 2 was placed in both compartments. The solutions were not stirred during the experiment. The cell was connected to a potentiostat by making electrical contact to the copper tape slip that protruded from the side of the working compartment. A Teflon cap fitted with a reference electrode (Ag/AgCl) was used to cover the working compartment and to ensure a fixed distance between working and reference electrodes for all experiments. A platinum gauze was placed in the second compartment separated by a frit from the first one and used as a counter electrode. X-ray absorption spectra were recorded at different positions on the electrode to check the materials for homogeneity. The same electrodes were used to measure the Mo K-edge (BL 7-3) and L-edges (BL 4-3) and the S K-edge (BL 4-3) spectra. For Mo K-edge measurements, the spectra were recorded in air. For S K-edge and Mo L-edge measurements, the electrochemical cell was placed in a He-filled bag with a polypropylene membrane placed as close as possible to the Si_3N_4 membrane to maximize the penetration of X-rays into and from the MoS_x film. Spectra were recorded on the dry electrodeposited MoS_x films at first and then in pH 2 nitric acid solution at 0.3, 0.1, −0.1, and −0.3 V vs RHE. All references hereafter are given vs RHE. The experiments were conducted at pH = 2 since the ITO layer deposited on the Si_3N_4 membrane could not withstand lower pH

values. The open-circuit potential measured prior to applying a potential was 0.8 V. At each potential, 10 scans were recorded for the Mo K-edge and 4 scans for the S K-edge and Mo L-edge. After each potential change, the system was allowed to equilibrate for 10 min before recording a spectrum. No noticeable change was observed between the first and last spectra recorded at a given potential. The current density measured for the potentials of interest (see Figure S1) was similar to those recorded on a regular ITO electrode under identical conditions (room temperature, pH 2 in nitric acid). A polarization curve of the film on a rotating disk carbon electrode at pH = 2 is also shown in Figure S2.

2.5. XAS Data Reduction and Analysis. Data reduction of the Mo K-edge extended X-ray absorption fine structure (EXAFS) spectra was performed using EXAFSPAK (Drs. Graham George and Ingrid Pickering, SSRL). Pre-edge and post-edge backgrounds were subtracted from the XAS spectra, and the results were normalized with respect to edge height. Background removal in *k*-space was achieved through a five-domain cubic spline. Curve fitting was performed with Artemis and IFEFFIT software using ab initio calculated phases and amplitudes from the program FEFF 8.2.[29,30] The details of curve fitting are discussed in the SI. For the S K-edge spectra, an E_0 value of 2470.8 eV was used, and normalization was performed over the range 2488.8−2510.8 eV. For the Mo L_3-edge and L_2-edge, E_0 values of 2523.6 and 2627.0 eV were used, and normalization was performed over the ranges 2545.3−2591.6 eV and 2648.7−2666.7 eV, respectively.

3.0. RESULTS

We use the notation precatalytic and catalytic states for the MoS_x film poised at 0.3 and −0.3 V in a nitric acid solution at pH = 2, respectively. These states were measured *in situ*, while the as prepared film was measured *ex situ*.

3.1. MoS_x Film Deposition. The deposition and characterization of MoS_x films under various conditions were described in a recent publication.[19] The as prepared MoS_x film studied in this work corresponds to the MoS_3-CV film before activation in ref 19.

3.2. Mo K-edge XANES of MoS_x Films and Reference Compounds. The films deposited did not show any X-ray diffraction (XRD) signal, which indicates that they are amorphous. We therefore used X-ray absorption spectroscopy to study the structure of these films. The Mo K-edge X-ray absorption near edge spectroscopy (XANES) spectra were recorded *ex situ* on the MoS_x film as prepared and *in situ* in the precatalytic and catalytic states (Figure 1A) using a custom-made X-ray spectroelectrochemical cell described in the Electrodeposition of MoSx Electrocatalyst Section. For comparison, the XANES spectra of MoS_3, MoS_2, and $[Mo_3S_4(H_2O)_9]Cl_4$ are shown in Figure 1B. No clear trend reflecting the formal oxidation state of Mo is observed in the Mo rising edge energy of the reference compounds, which is largely due to the charge delocalization between the molybdenum ion and the sulfur ligands. For the MoS_x film, changes at the peak top are observed, while the rising edge energy remains identical when changing the potential applied to the film. None of these spectra present a good match with those of the reference compounds, suggesting a mixed composition for the MoS_x film.

3.3. Mo K-edge EXAFS of MoS_x Films and Reference Compounds. The Mo K-edge EXAFS spectra were recorded *ex situ* on the MoS_x film (as prepared) and *in situ* in the precatalytic and catalytic states (Figure 1C). For comparison, the EXAFS spectra of the MoS_3, MoS_2, and $[Mo_3S_4(H_2O)_9]Cl_4$ are shown in Figure 1D. The *k*-space spectra of these compounds are also compared on Figure S3. The EXAFS

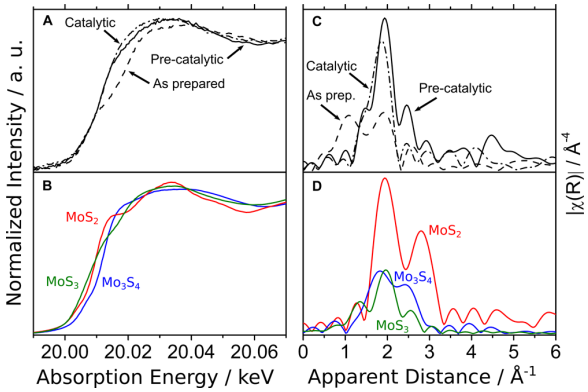

Figure 1. (A) Mo K-edge XANES spectra of the MoS_x film as prepared and in the precatalytic and catalytic states. (B) Mo K-edge XANES spectra of Mo_3S_4, MoS_2 and MoS_3. (C) Mo K-edge Fourier transform EXAFS (k^3-weighted) of the MoS_x film as prepared and in the precatalytic and catalytic states. (D) Mo K-edge Fourier transform EXAFS (k^3-weighted) of Mo_3S_4, MoS_2, and MoS_3.

spectrum of as prepared film shows two peaks at R' = 1.2 and 1.9 Å (R' being the apparent distance and R the actual distance), corresponding to Mo−O and Mo−S interactions, respectively (*vide infra*). When poised at 0.3 V, the short-distance peak (R' = 1.2 Å) disappears, and the spectrum of the precatalytic state shows similarities with that of MoS_3, with a high intensity peak at ca. R' = 2.0 Å and a small intensity peak at ca. R' = 2.5 Å. Under catalytic conditions, the main peak shifts to a lower apparent distance (R' = 1.86 Å), suggesting a shortening of the Mo−S bond. In addition, the small intensity peak at R' = 2.5 Å disappears, suggesting the breaking of the Mo−Mo bond.

Prior to fitting the EXAFS spectra of MoS_x films, the EXAFS spectra of three model compounds were fit using structural data derived from their crystal structures to extract the EXAFS fitting parameters. The final fitting parameters are listed in Table 2. In the case of MoS_3, two distances are required to fit the spectrum, one accounting for 6 Mo−S bonds at 2.42 Å and another one for 1 Mo−Mo bond at 2.77 Å. Two competing structural models have been proposed for MoS_3 by Hibble et al.[24,31] and Weber et al.[25] The Hibble structure for MoS_3 consists of chains of molybdenum ions alternatively bridged by three sulfides (μ-η^2 S^{2-}) or one sulfide and one disulfide (μ-η^2:η^2 S_2^{2-}) ligands (see Table 1).[32] The formula for this material is thus $Mo^{V}(S^{2-})_2(S_2^{2-})_{0.5}$. Several authors[33,34] have shown that the EXAFS spectrum of MoS_3 is indeed best fit with a single Mo−Mo interaction because Mo ions only interact with neighboring Mo through the short bridge containing a disulfide unit but not through the long one containing sulfide groups only. The Weber structure consists of a random arrangement of four isostructural Mo_3S_9 clusters, which are linked to each other by one or two μ-η^2 sulfide bridge(s). Each cluster contains three sulfide and three disulfide ligands, which can be either bridging or terminal. The formulation for this structure is thus $Mo^{IV}(S^{2-})(S_2^{2-})$. The fitting parameters are in agreement with the literature for both proposed structures, and we cannot discriminate one from the other. In the Weber structure, each molybdenum center is surrounded by 5, 6, or 7 sulfur ligands. This is compatible with the quite large Debye−Waller factor (0.010) found for the Mo−S interaction in the MoS_3 EXAFS fit (see Table 2). The spectrum of MoS_2 (which

Table 2. EXAFS Fitting Parameters for MoS_3, MoS_2, Mo_3S_4, and the MoS_x Film As Prepared, Under Pre-Catalytic (0.3 V), and Catalytic State (−0.3 V)[a]

		R, Å				
sample	shell	XRD	EXAFS	N	σ^2	R, %
MoS_3[b]	Mo−S	–	2.42	**6**	0.010	0.06
	Mo−Mo	–	2.77	**1**	0.005	
MoS_2[c]	Mo−S	2.41	2.41	**6**	0.001	0.4
	Mo−Mo	3.15	3.17	**6**	0.003	
Mo_3S_4[d]	Mo−O	2.18	2.13	**3**	0.002	1.3
	Mo−S	2.30	2.23	**3**	0.010	
	Mo−Mo	2.73	2.72	**2**	0.003	
MoS_x as prepared[e]	Mo−O	–	1.74	1.2	**0.002**	0.01
	Mo−S	–	2.44	3.0	**0.010**	
	Mo−Mo	–	2.76	0.8	**0.005**	
MoS_x 0.3 V[b]	Mo−S	–	2.40	6.4	**0.010**	1.6
	Mo−Mo	–	2.74	1.1	**0.003**	
MoS_x 1	Mo−S	–	2.36	6.2	**0.010**	2.2
-0.3 V[b] 2	Mo−S	–	2.37	6.1	**0.010**	2.1
	Mo−Mo	–	2.69	0.2	**0.003**	

[a]Bold numbers indicate fixed values. R is the apparent distance in Å from the central atom to the scatterer, k is the wave vector describing the trajectory of the scattered photoelectron, N is the number of scatterers, R^2 is the Debye−Waller factor, and R is the goodness of fit in %. [b]Fitting range: $3.10 \leq k$ (/Å) ≤ 11.5 and $1.57 \leq R$ (Å) ≤ 2.82. [c]Fitting range: $3.10 \leq k$ (/Å) ≤ 11.5 and $1.15 \leq R$ (Å) ≤ 3.20. [d]Fitting range: $3.10 \leq k$ (/Å) ≤ 11.5 and $1.15 \leq R$ (Å) ≤ 2.82. [e]Fitting range: $3.10 \leq k$ (/Å) ≤ 10.5 and $1.15 \leq R$ (Å) ≤ 2.82.

is microcrystalline) shows two well-separated peaks at ca. R' = 1.95 and R' = 2.80 Å that can be fit with Mo−S and Mo−Mo interactions at 2.41 and 3.17 Å with N values of 6 for each interaction. These values are in very good agreement with the XRD distances reported for MoS_2 (2.40 and 3.15 Å).[35] The spectrum of $[Mo_3S_4(OH_2)_9]^{4+}$ shows two peaks at ca. R' = 1.80 and R' = 2.40 Å. The low R' peak was fit with Mo−O and Mo−S interactions at 2.13 and 2.23 Å, respectively, with N values of 3 for both interactions. The higher R' peak is due to a single Mo−Mo vector at R = 2.72 Å with an N value of 2. These values are in very good agreement with the XRD structure of $[Mo_3S_4(H_2O)_9]Cl_4$.[36]

The EXAFS curve fitting results of the MoS_x film as prepared and in the precatalytic and catalytic states are summarized in Table 2, and the k-space curves are displayed in Figure S4. For the as prepared film, an Mo−O interaction with a distance of R = 1.74 Å and an N value of 1.2 had to be included to model the peak at short R' value. The peak at R' = 1.90 Å was fit with an Mo−S interaction (R = 2.44 Å, N = 3.0), while the low intensity one at R' = 2.61 Å was fit with an Mo−Mo interaction (R = 2.76 Å, N = 0.8). For the film in the precatalytic state (poised at 0.3 V), the best fit was obtained with an Mo−S interaction at 2.40 Å with an N value close to 6 and an Mo−Mo interaction at 2.74 Å with an N value of 1.1. Under these conditions, the parameters of the Mo−S and Mo−Mo interaction are in good agreement with those of MoS_3. We therefore considered the film in the precatalytic state to be predominantly composed of MoS_3. When the potential was lowered to −0.3 V (catalytic state), the Mo−Mo peak is barely present in the EXAFS spectrum. Fitting the data with a single shell (fit #1), yields an Mo−S interaction with R = 2.36 Å and N = 6. This distance is slightly shorter (0.05 Å) than that of the film poised at 0.3 V. We also considered the presence of an Mo−Mo second shell (fit #2). In this fit, the N value for the Mo−Mo interaction dropped to 0.2, while it did not show a significant improvement in the fit quality. We therefore conclude that the Mo−Mo bond is significantly diminished in the MoS_x film in the catalytic state.

3.4. *In Situ* Sulfur K-edge XANES. Since the sulfur K-edge energy (ca. 2472 eV) is just below that of the molybdenum L-edges (ca. 2526 and 2631 eV for the L_3- and L_2-edges, respectively), we recorded spectra with both edges in one single scan (see Figure S5). Figure 2A shows the S K-edge spectra collected on the MoS_x film as prepared and in the precatalytic and catalytic states as well as the reference compounds listed in Table 1. The spectrum of Mo_3S_4 shows several features, with a main peak at 2471.6 eV (measured at peak top), a shoulder at 2472.8 eV, and an intense low energy peak at 2469.8 eV. In MoS_2, a single, sharp peak is observed at ca. 2471.4 eV, and a shoulder is observed at 2473.6 eV. The spectrum of MoS_3 shows a single, broad feature at 2472.5 eV.

The S K-edge spectra of the MoS_x film poised at 0.3, 0.1, −0.1, and −0.3 V are shown in Figure 2B, and the corresponding first moment energies are listed in Table 3. In the as prepared MoS_x film, the sulfur K-edge main peak energy (2472.1 eV) and shape are similar to that of MoS_3, although a shoulder is present at low energy (2469.7 eV) as in Mo_3S_4, but with a much smaller intensity. When the sample is set in a pH 2 nitric acid solution and the potential is poised to 0.3 V, the first moment energy of the main peak remains at 2472.0 eV, while the shoulder at lower energy (2469.8 eV) increases and the one at higher energy (2472.4 eV) decreases. When the potential is gradually decreased to −0.3 V, the first moment energy of the main peak shifts to a slightly higher energy (from 2472.0 to 2472.3 eV), which indicates an overall oxidation of the sulfur ligands. Concomitantly, the lower energy shoulder that is present in Mo_3S_4 decreases.

3.5. *In Situ* Molybdenum L-edge XANES. Figure 2C shows the molybdenum L_3-edge spectra recorded on the MoS_x film as prepared and in the precatalytic and catalytic states as well as the reference compounds listed in Table 1. The Mo L_3-edge spectrum of Mo_3S_4 shows one main, broad feature, centered at 2525.1 eV (measured at peak top), with a shoulder at 2523.25 eV. The spectrum of MoS_2 shows a single feature at 2524.7 eV, while that of MoS_3 has a main peak at 2525.8 eV with a shoulder at higher energy (2528.4 eV). The spectrum recorded on the as prepared MoS_x film is very similar to that of MoS_3. For instance, it has a shoulder at 2528.7 eV, which is a strong component of the MoS_3 spectrum. This is even more visible in the L_2-edge spectrum (see Figure 2E), where the as prepared spectrum shows the double peak feature (2629.3 and 2629.6 eV) that is also present in MoS_3.

The Mo L_3-edge spectra of the MoS_x film poised at 0.3, 0.1, −0.1, and −0.3 V are shown in Figure 2D, and the corresponding first moment energies (as well as those of the Mo L_2-edge spectra) are reported in Table 3. Under precatalytic conditions (pH 2 nitric acid, 0.3 V), the L_3-edge peak first moment energy shifts to a lower energy by ca. 0.4 eV as compared to the as prepared film, and the higher energy component (2528.4 eV) characteristic of MoS_3 disappears. When progressively decreasing the potential to −0.3 V, the first moment energy of the Mo L_3-edge peak shifts to lower values by ca. 0.06 eV, indicating a reduction of the Mo center. The same trend is observed for the L_2-edge part of the spectra (see Figure 2D) with an even more pronounced shift of the first

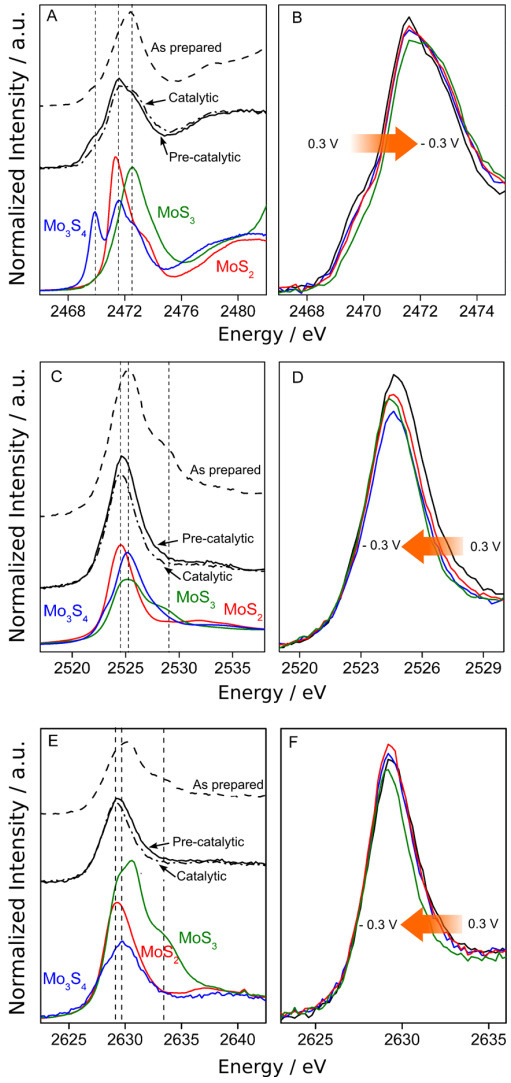

Figure 2. Top: Sulfur K-edge spectra of (A) the MoS_x film as prepared, in the precatalytic and catalytic states, together with Mo_3S_4, MoS_2 and MoS_3 reference spectra, and (B) the MoS_x film poised at 0.3 (black), 0.1 (blue), −0.1 (red), and −0.3 V (green) in nitric acid at pH = 2. Middle: Molybdenum L_3-edge spectra of (C) the MoS_x film as prepared, in the precatalytic and catalytic states, together with Mo_3S_4, MoS_2, and MoS_3 and (D) the MoS_x film poised at 0.3 (black), 0.1 (blue), −0.1 (red), and −0.3 V (green) in nitric acid at pH = 2. Bottom: Molybdenum L_2-edge spectra of (E) the MoS_x film as prepared, in the precatalytic and catalytic states, together with Mo_3S_4, MoS_2, and MoS_3 and (F) the MoS_x film poised at 0.3 (black), 0.1 (blue), −0.1 (red), and −0.3 V (green) in nitric acid at pH = 2.

moment to lower energies (by ca. 0.2 eV) as the potential decreases.

4.0. DISCUSSION

The MoS_x films studied in this paper were prepared by electrochemical cycling of an ITO electrode in an $[NH_4]_2MoS_4$ aqueous solution. This procedure was shown to involve anodic and cathodic deposition processes, as well as cathodic corrosion. Eventually, the final composition of the film was estimated from XPS and Electrochemical Quartz Crystal Microbalance (EQCM) analysis as a mixture of MoS_2 and MoS_3 phases.[22] In line with this first analysis, the X-ray spectroscopic data of the as prepared sample presented in this paper show features associated with several compounds, clearly indicating that the MoS_x electrocatalyst is a mixture of species. Table 4 summarizes the spectroscopic information collected on the as prepared, precatalytic and catalytic states. It also indicates the structural and electronic changes observed when the potential is gradually decreased from 0.3 (precatalytic state) to −0.3 V (*catalytic* state).

Table 3. Sulfur K-Edge and Molybdenum $L_{2,3}$-Edge Peak First Moment Energies (in eV) for the MoS_x Film As Prepared and Poised at 0.3, 0.1, −0.1, and −0.3 V in pH 2 Nitric Acid

		Mo	
sample	S K-edge	L_3-edge	L_2-edge
as prepared	2472.15	2526.95	2631.43
0.3 V	2472.00	2526.54	2631.00
0.1 V	2472.10	2526.51	2630.90
−0.1 V	2472.13	2526.49	2630.86
−0.3 V	2472.27	2526.48	2630.80

4.1. Initial Structure of the as prepared MoS_x Film. In the Mo K-edge EXAFS Fourier transform spectrum of the as prepared sample, the peak observed at low R' values (1.05 Å) indicates the presence of an Mo−O interaction. The Mo−O distance obtained from the fits (R = ca. 1.75 Å) is much shorter than usually observed in most $Mo_xO_yS_z$ oxysulfide compounds (typically $2.0 \leq R \leq 2.2$ Å)[37] or in $Mo_3S_4(OH_2)_9$ (*vide supra*), and is longer than the Mo−O distances observed in molybdenum oxides.[38,39] The presence of oxygen has also been observed previously in the XPS spectra recorded *ex situ* on the as prepared MoS_x film.[22] Given that the latter technique is only sensitive to the surface, we estimated that a layer of molybdenum oxide MoO_x covers the bulk MoS_3 material in the as prepared film, as a result of air oxidation during transfer from the synthesis laboratory to the synchrotron facility. Since the film is highly porous, the actual surface exposed to air and converted into an oxide could be significant. The EXAFS fits indicate the presence of 3 Mo−S interactions at R = 2.44 Å and one Mo−Mo interaction at R = 2.76 Å. All parameters corresponding to an MoS_3 structure, except for the lower number of Mo−S vectors.

This deviation can be explained by the presence of the outer-shell MoO_x layer in the as prepared film that decreases the average Mo−S bonds per Mo center. This analysis is consistent with the previous XPS observations showing the presence of Mo(IV) and of S^{2-} and S_2^{2-} ligands.[8] The presence of peaks characteristic of MoS_3 at 2528.7 and 2633.5 eV in the Mo L_3- and L_2-edge spectra, respectively, confirms an MoS_3 structure. The small intensity feature at 2470 eV that is characteristic of Mo_3S_4 suggests the presence of similar chemical motifs in the as prepared material. Indeed, the Mo_3S_9 trinuclear units proposed by Weber as constituents of MoS_3 are closely related to Mo_3S_4, since they share the same geometrical arrangement as well as μ-η^2 and μ-η^3 bridging S^{2-} ligands. It is, however, very difficult to distinguish small contributions of Mo_3S_4 within the MoS_3 K-edge EXAFS, since the Mo−S and Mo−Mo distances of these two materials are almost identical (see Table 2). The starting material is thus best described as an amorphous film of MoS_3 in the bulk, with a surface layer of MoO_x. The oxidation state of

Table 4. Summary of the Spectroscopic Features Observed for the MoS_x Film As Prepared and Under Pre-Catalytic (0.3 V) and Catalytic (−0.3 V) Conditions

	Mo K-edge EXAFS		S K-edge XANES	Mo L-edge XANES
sample	number and nature of interaction	R, Å	sulfur oxidation state and binding mode	formal oxidation states of molybdenum
dry (as prepared)	1 Mo−O	1.74	μ-η^2 S^{2-}, μ-η^3 S^{2-}, μ-η^2:η^2 S_2^{2-}	Mo(V) or Mo(IV)[a]
	3 Mo−S	2.44		
	1 Mo−Mo	2.75		
↓	shortening of Mo−S bond, increased number of Mo−Mo bonds		reduction	reduction
0.3 V (precatalytic)	6 Mo−S	2.40	μ-η^2 S^{2-}, μ-η^3 S^{2-}, μ-η^2:η^2 S_2^{2-}	Mo(IV)
	1 Mo−Mo	2.74		
↓	shortening of Mo−S bond, diminished Mo−Mo interactions		oxidation	reduction
−0.3 V (catalytic)	6 Mo−S	2.36	μ-η^2 S^{2-}, μ-η^3 S^{2-}, η^2 S_2^{2-}	Mo(IV), Mo(III)

[a]In MoS_3, the molybdenum ion is described as Mo(V) in the Hibble model and as Mo(IV) in the Weber model.

molybdenum centers is predominantly +IV, while the sulfur ligands are present as bridging sulfides (μ-η^2 and μ-η^3 S^{2-}) and disulfides (μ-η^2:η^2 S_2^{2-}).

4.2. Structure of the MoS_x Film in its Precatalytic State. When the MoS_x film is set in a nitric acid solution at pH = 2 and poised at 0.3 V, the Mo−O interaction in the Mo K-edge EXAFS spectrum of the as prepared material disappears, indicating that the molybdenum oxide fraction is hydrolyzed. This phenomenon was already observed by XPS on the surface of a similar system.[22] The current data extend these structural considerations to the bulk of the material. Under precatalytic conditions, the EXAFS fits indicate 6 Mo−S interaction at R = 2.40 Å and 1 Mo−Mo interactions at R = 2.74 Å, which correspond to the fitting parameters of MoS_3. However, the Mo $L_{2,3}$-edge and S K-edge XAS show that the material formed cannot be considered as pure MoS_3. In the S K-edge spectrum, the shoulder at 2470 eV characteristic of Mo_3S_4 is more intense than in the as prepared material, which suggests a larger fraction of trinuclear Mo_3S_x units as compared to the as prepared material. Hence, the overall S K-edge first moment energy is shifted to lower energy by 0.15 eV, indicating a reduction of the disulfide units originally present in the as prepared material. The features characteristic of MoS_3 in the Mo L_3- and L_2-edge spectra (at 2528.7 and 2633.5 eV, respectively) disappeared, and the first moment of these peaks are shifted to lower energy by ca. 0.4 eV, indicating a reduction of the molybdenum centers as well. These data indicate that, when placed in an acidic media, the as prepared material is reduced, both from the sulfur and the molybdenum side, into an amorphous material where molybdenum and sulfur are in the +IV and −II oxidation state, respectively. Although MoS_2 fits best with this description, the spectral features of the S K and Mo $L_{2,3}$-edge XAS suggest that a fraction of MoS_3 and/or Mo_3S_4 is still present. It is likely that the outer shell, which is accessible to the solvent, is converted into MoS_2. We suggest that the reduction under acidic conditions of the disulfide ligands in MoS_3 produces sulfide ligands, which in turn displaces the oxygen ligands in MoO_x to yield MoS_2. We note that the strong peak at R = 3.15 Å corresponding to the Mo−Mo interaction in microcrystalline MoS_2 is not observed, which can be explained by the amorphous nature of the MoS_2 layer.

4.3. Structure of the MoS_x Film in its Catalytic State. When the potential is decreased to −0.3 V, the Mo−Mo interaction observed at ca. R = 2.75 Å in the Mo K-edge EXAFS diminishes. The disappearance of this peak, corresponding to Mo−Mo interactions in Mo_3S_4 and MoS_3, can be interpreted as the formation of MoS_2 from MoS_3 and the corresponding disappearance of the bridging disulfide units in the bulk of the film. This hypothesis is supported by the Mo−S distance at −0.3 V, which is longer than that in Mo_3S_4 and matches the one found in MoS_2. As the potential is decreased from 0.3 to −0.3 V, the S K-edge XANES spectra of the MoS_x film shows a progressive increase in their first moment energy (Figure 2B), which indicates an overall oxidation of the sulfur ligands. The difference in peak position between the highest and lowest potentials is only of 0.27 eV (compared to the 1.1 eV shift observed in the sulfur oxidation state change from MoS_2 to MoS_3), indicating a partial fraction of sulfur being oxidized in the sample. This small shift can be explained by a modification of the material only at the surface in contact with the electrolyte. Since the Mo−Mo interaction disappears in the Mo K-edge EXAFS, the increase in the oxidation state of the sulfur ligands is likely due to the presence of terminal disulfide ligands (η^2 S_2^{2-}) rather than bridging ones (μ-η^2:η^2 S_2^{2-}). When the potential is decreased from 0.3 to −0.3 V, the Mo L-edge first moment concomitantly shifts to lower energies (−0.06 and −0.2 eV for the Mo L_3- and L_2-edges, respectively), which indicates that the molybdenum centers are reduced to a lower oxidation state. As for the S K-edge XANES, the energy shift is limited as compared to what is observed for pure, bulk compounds (−0.48 and −0.55 eV from MoS_3 to MoS_2 for the L_3- and L_2-edges, respectively). Namely, the S K-edge and Mo L-edge shifts are correlated to each other, and it suggests a change in oxidation state for the molybdenum centers located only at the solid−liquid interface.

In summary, the material's bulk structure at −0.3 V is modified from amorphous MoS_3 to amorphous MoS_{2+x}, in which bridging disulfides are absent and the predominant oxidation state of molybdenum is +IV. As mentioned before, the small changes observed at the S K- and Mo L-edges strongly suggest that these changes occur at the solid−liquid interface only, where the MoS_x material is in contact with the acidic media. At −0.3 V, this interface presents a significant amount of oxidized sulfur ligands (as terminal disulfide units) as well as reduced molybdenum (formally Mo(III)) centers. These conclusions are in line with the previous XPS and electrochemical quartz crystal microbalance (EQCM) analysis of the same film after the first reductive voltametric scan.[22] According to these techniques, which probe the surface and mass composition of the film, the surface of the material was converted upon immersion in acid from MoS_3 to a material very similar to MoS_2, with a slight excess of sulfur ligands. The

material was thus formulated as MoS_{2+x}, which corresponds to a loss of sulfur ligands. We did not, however, observe any decrease in the sulfur X-ray fluorescence intensity when the potential was reduced from +0.3 to −0.3 V. This indicates that the loss of sulfur occurs before setting the potential to the precatalytic conditions.

4.4. Implications for the Hydrogen Evolution Mechanism. Scheme 1 shows the proposed phase changes of the

Scheme 1. Proposed Changes and Catalytic Cycle for the MoS_x Film As Prepared and at pH = 2 under Pre-Catalytic and Catalytic Conditions[a]

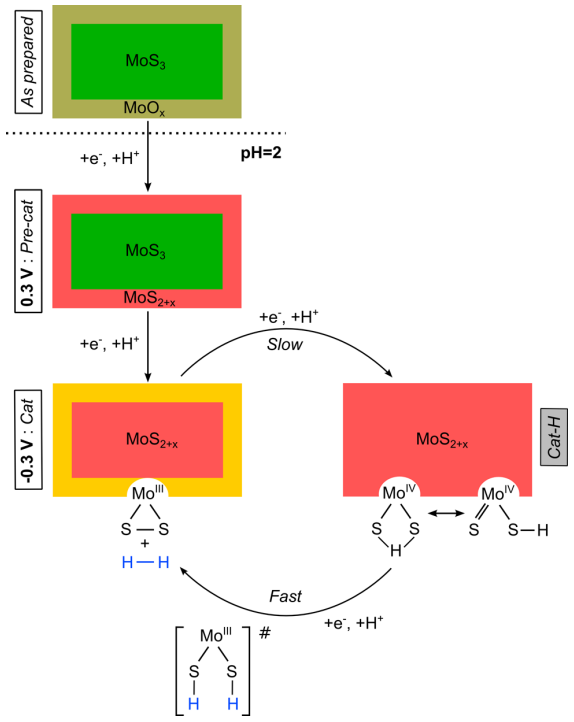

[a]The Cat−H species is putative and has not been observed experimentally.

MoS_x film under the various conditions studied in this paper, and proposes catalytic intermediates for the proton reduction reaction. The Cat species is the one predominantly observed at −0.3 V, while Cat−H stands for a putative species formed during the HER catalytic cycle. It is important to note that the species observed spectroscopically at a given potential represent the kinetically most populated state under these conditions. Therefore, in the case of a catalytic reaction, it also probes the rate-limiting step of the process, which involves the disappearance of the species observed spectroscopically.

In the MoS_x film, the interfacial Mo centers are in the +IV oxidation state when the potential is poised to 0.3 V, and the sulfur is protonated due to the highly acidic conditions. Since the potential is maintained at a quite high value, no hydrogen evolution is observed. When the potential is decreased, the driving force for the reduction of MoS_3 into Cat increases, leading to the reduction of the molybdenum centers from +IV to +III, the release of dihydrogen and the formation of terminal disulfide units. Although the Cat species may not be stable in the long-term under such acidic and reductive conditions (the terminal disulfides are likely to be reduced and/or protonated), it is longer-lived than Cat−H, which is consumed as soon as it is reformed. Consequently, the rate-limiting step under HER conditions appears to be the protonation and reduction of the interfacial $Mo^{III}(S_2)$ units formed together with the release of H_2.

The addition of a hydrogen atom to Cat−H is therefore favored (and thus faster) than it is to Cat, which accumulates and can be observed spectroscopically. DuBois et al. have also proposed[12,40] that dimeric, bis-μ-hydrosulfido $Mo_2(III)$ complexes can eliminate H_2 when reacting with alkenes or alkynes in 2 + 2 additions. This type of reaction parallels the HER studied here, where electrons are provided by the electrode in place of the unsaturated olefins. By analogy with this addition−elimination mechanism and on the basis of our own observations, we suggest that the last intermediate before the release of H_2 is an Mo(III) species with two terminal hydrosulfide ligands, generated by the facile addition of a hydrogen atom to the $Mo^{IV}(S)(SH)$ species in Cat−H.

5.0. CONCLUSION

By combining *in situ* X-ray spectroscopies with electrochemistry, we have investigated the structural changes that occur in an MoS_x hydrogen-evolving electrocatalyst under functional conditions. The starting material before catalysis is identified as predominantly MoS_3. When set in the acidic conditions used for catalysis, the material remains essentially the same, except for the outermost layer. As the potential is decreased to induce the production of H_2, a progressive reduction of the molybdenum centers is observed concomitantly with the oxidation of the sulfur ligands. We therefore suggest that Mo(III) units with terminal disulfide ligands (η^2 S_2^{2-}) are transiently formed at the interface with the solution when H_2 is released. As a corollary, the catalytic species prior to the release of H_2 is very similar to MoS_2, with terminal hydrosulfide ligands at the interface with the liquid. Following this analysis, we propose that the rate-limiting step under HER conditions is the protonation and reduction of interfacial $Mo^{III}(S_2)$ sites. These results show experimental evidence for the direct involvement of a disulfide unit in molybdenum sulfide-based HER and proposes new hypotheses for the mechanism of hydrogen evolution in these materials. Further investigations are currently underway to understand in more detail the structure of these films under functional conditions and their reaction mechanism.

■ ASSOCIATED CONTENT

Supporting Information

Polarization curve for the film at pH = 2, current density as a function of potential for the MoS_x film during *in situ* XAS measurements, *k*-space EXAFS spectra and corresponding fits for the MoS_x film and reference compounds and combined sulfur K-edge and molybdenum $L_{2,3}$-edge spectra. This material is available free of charge via the Internet at http://pubs.acs.org.

■ AUTHOR INFORMATION

Corresponding Authors

benedikt.lassalle@synchrotron-soleil.fr
xile.hu@epfl.ch
jyano@lbl.gov

Notes

The authors declare no competing financial interest.

dx.doi.org/10.1021/ja510328m | J. Am. Chem. Soc. 2015, 137, 314−321

■ ACKNOWLEDGMENTS

Dr. Delphine Vantelon of the LUCIA beamline at SOLEIL is greatly acknowledged for the collection of S K-edge and Mo L-edge spectra on reference samples. XAS data collection was carried out at the Stanford Synchrotron Radiation Lightsource (SSRL) beamlines 4-3, operated by Stanford University for the U.S. DOE Office of Science and supported by the DOE Office of Biological and Environmental Research and by the NIH (including P41GM103393). XAS work was funded by the Director, Office of Science, Office of Basic Energy Sciences (OBES), Division of Chemical Sciences, Geosciences, and Biosciences of the Department of Energy (DOE) under contract DE-AC02-05CH11231 (J.Y. and V.K.Y). The work at EPFL is supported by a starting grant from the European Research Council (no. 257096).

■ REFERENCES

(1) Armaroli, N.; Balzani, V. *Angew. Chem., Int. Ed.* **2007**, *46*, 52.
(2) Nocera, D. G. *Inorg. Chem.* **2009**, *48*, 10001.
(3) Turner, J. A. *Science* **1999**, *285*, 687.
(4) Merki, D.; Hu, X. *Energy Environ. Sci.* **2011**, *4*, 3878.
(5) Nguyen, M. T. D.; Ranjbari, A.; Catala, L.; Brisset, F.; Millet, P.; Aukauloo, A. *Coord. Chem. Rev.* **2012**, *256*, 2435.
(6) Cobo, S.; Heidkamp, J.; Jacques, P.-A.; Fize, J.; Fourmond, V.; Guetaz, L.; Jousselme, B.; Ivanova, V.; Dau, H.; Palacin, S.; Fontecave, M.; Artero, V. *Nat. Mater.* **2012**, *11*, 802.
(7) Di Giovanni, C.; Wang, W.-A.; Nowak, S.; Greneche, J.-M.; Lecoq, H.; Mouton, L.; Giraud, M.; Tard, C. *ACS Catal.* **2014**, *4*, 681.
(8) Popczun, E. J.; Read, C. G.; Roske, C. W.; Lewis, N. S.; Schaak, R. E. *Angew. Chem., Int. Ed.* **2014**, *53*, 5427.
(9) Laursen, A. B.; Kegnaes, S.; Dahl, S.; Chorkendorff, I. *Energy Environ. Sci.* **2012**, *5*, 5577.
(10) Chianelli, R. R.; Daage, M.; Ledoux, M. J. In *Advances in Catalysis*; Academic Press: San Diego, CA, 1994; Vol. *40*, pp 177−232.
(11) Riaz, U.; Curnow, O. J.; Curtis, M. D. *J. Am. Chem. Soc.* **1994**, *116*, 4357.
(12) Appel, A. M.; DuBois, D. L.; DuBois, M. R. *J. Am. Chem. Soc.* **2005**, *127*, 12717.
(13) Jaramillo, T. F.; Bonde, J.; Zhang, J.; Ooi, B.-L.; Andersson, K.; Ulstrup, J.; Chorkendorff, I. *J. Phys. Chem. C* **2008**, *112*, 17492.
(14) Kibsgaard, J.; Jaramillo, T. F.; Besenbacher, F. *Nat. Chem.* **2014**, *6*, 248.
(15) Hinnemann, B.; Moses, P. G.; Bonde, J.; Jorgensen, K. P.; Nielsen, J. H.; Horch, S.; Chorkendorff, I.; Norskov, J. K. *J. Am. Chem. Soc.* **2005**, *127*, 5308.
(16) Jaramillo, T. F.; Jorgensen, K. P.; Bonde, J.; Nielsen, J. H.; Horch, S.; Chorkendorff, I. *Science* **2007**, *317*, 100.
(17) Tang, M. L.; Grauer, D. C.; Lassalle-Kaiser, B.; Yachandra, V. K.; Amirav, L.; Long, J. R.; Yano, J.; Alivisatos, A. P. *Angew. Chem., Int. Ed.* **2011**, *50*, 10203.
(18) Li, Y.; Wang, H.; Xie, L.; Liang, Y.; Hong, G.; Dai, H. *J. Am. Chem. Soc.* **2011**, *133*, 7296.
(19) Merki, D.; Fierro, S.; Vrubel, H.; Hu, X. *Chem. Sci.* **2011**, *2*, 1262.
(20) Kibsgaard, J.; Chen, Z.; Reinecke, B. N.; Jaramillo, T. F. *Nat. Mater.* **2012**, *11*, 963.
(21) Vrubel, H.; Merki, D.; Hu, X. *Energy Environ. Sci.* **2012**, *5*, 6136.
(22) Vrubel, H.; Hu, X. *ACS Catal.* **2013**, *3*, 2002.
(23) Karunadasa, H. I.; Montalvo, E.; Sun, Y.; Majda, M.; Long, J. R.; Chang, C. J. *Science* **2012**, *335*, 698.
(24) Hibble, S. J.; Rice, D. A.; Pickup, D. M.; Beer, M. P. *Inorg. Chem.* **1995**, *34*, 5109.
(25) Weber, T.; Muijser, J. C.; Niemantsverdriet, J. W. *J. Phys. Chem.* **1995**, *99*, 9194.
(26) Shibahara, T.; Kuroya, H. *Polyhedron* **1986**, *5*, 357.
(27) Bediako, D. K.; Lassalle-Kaiser, B.; Surendranath, Y.; Yano, J.; Yachandra, V. K.; Nocera, D. G. *J. Am. Chem. Soc.* **2012**, *134*, 6801.
(28) Gorlin, Y.; Lassalle-Kaiser, B.; Benck, J. D.; Gul, S.; Webb, S. M.; Yachandra, V. K.; Yano, J.; Jaramillo, T. F. *J. Am. Chem. Soc.* **2013**, *135*, 8525.
(29) Newville, M. *J. Synchrotron Radiat.* **2001**, *8*, 96.
(30) Rehr, J. J.; Albers, R. C. *Rev. Mod. Phys.* **2000**, *72*, 621.
(31) Afanasiev, P.; Jobic, H.; Lorentz, C.; Leverd, P.; Mastubayashi, N.; Piccolo, L.; Vrinat, M. *J. Phys. Chem. C* **2009**, *113*, 4139.
(32) Hibble, S. J.; Walton, R. I.; Pickup, D. M.; Hamon, A. C. *J. Non. Cryst. Solids* **1998**, *232*, 434.
(33) Cramer, S. P.; Liang, K. S.; Jacobson, A. J.; Chang, C. H.; Chianelli, R. R. *Inorg. Chem.* **1984**, *23*, 1215.
(34) Hedoire, C. E.; Cadot, E.; Villain, F.; Davidson, A.; Louis, C.; Breysse, M. *Appl. Catal., A* **2006**, *306*, 165.
(35) Dickinson, R. G.; Pauling, L. *J. Am. Chem. Soc.* **1923**, *45*, 1466.
(36) Akashi, H.; Shibahara, T.; Kuroya, H. *Polyhedron* **1990**, *9*, 1671.
(37) Genuit, D.; Bezverkhyy, I.; Afanasiev, P. *J. Solid State Chem.* **2005**, *178*, 2759.
(38) Ijima, K.; Ohminami, Y.; Suzuki, S.; Asakura, K. *Top. Catal.* **2002**, *18*, 125.
(39) Menard, M. C.; Ishii, R.; Nakatsuji, S.; Chan, J. Y. *Inorg. Chem.* **2011**, *50*, 8767.
(40) Casewit, C. J.; Coons, D. E.; Wright, L. L.; Miller, W. K.; Dubois, M. R. *Organometallics* **1986**, *5*, 951.

ACS Energy LETTERS

Cite This: ACS Energy Lett. 2017, 2, 2545-2551 http://pubs.acs.org/journal/aelccp

LETTER

In Situ Observation of the Formation and Structure of Hydrogen-Evolving Amorphous Cobalt Electrocatalysts

Benedikt Lassalle-Kaiser,*[,†] Andrea Zitolo,[†] Emiliano Fonda,[†] Marc Robert,[‡] and Elodie Anxolabéhère-Mallart*[,‡]

[†]Synchrotron SOLEIL, L'Orme des Merisiers, Saint-Aubin, 91192 Gif-sur-Yvette, France

[‡]Sorbonne Paris Cité, Laboratoire d'Electrochimie Moléculaire, UMR 7591 Université Paris Diderot - CNRS, 15 rue Jean-Antoine de Baïf, 75205 Paris Cedex 13, France

Supporting Information

ABSTRACT: We have used in situ and operando X-ray absorption spectroscopy at the cobalt K-edge to study the formation of cobalt nanoparticles from a molecular precursor, as well as their structural evolution under hydrogen-evolving electrocatalytic conditions. We show that these particles, which are about 100−150 nm in diameter overall, are made of an uncommon form of amorphous metallic cobalt, the smallest ordered unit being 1 nm clusters of ∼50 cobalt atoms. In aqueous solution, these porous particles are partly oxidized into cobalt(II), a fraction of which remains present as an outer shell during hydrogen evolution electrocatalysis, even at very high cathodic potentials. Our operando measurements show that the activity of the particles is correlated to the oxidized layer thickness, a thinner layer exposing a larger fraction of the active metallic cobalt and leading to a higher activity. These findings expand our current understanding of the solid−liquid interface in hydrogen evolution catalytic species in neutral pH and suggest new directions for the improvement of hydrogen-evolving catalytic systems.

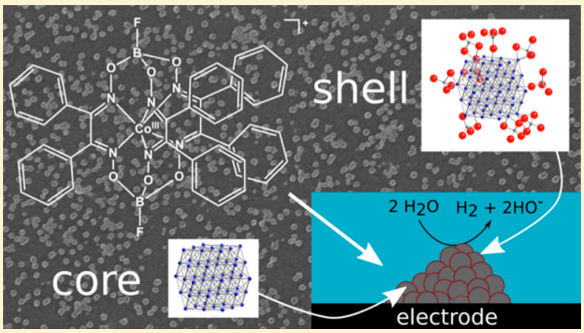

The production of storable fuels from renewable energy sources is a technological bottleneck that is strategic to our societies.[1−4] Among those fuels, hydrogen is considered a viable energy carrier[5] but is required in high purity to avoid poisoning the fuel cell's catalyst. High-purity hydrogen is produced in electrolyzers using platinum as a catalyst, which is too expensive for widespread use. The replacement of this noble metal by more abundant and cheaper ones has attracted a lot of research efforts in the last decades. For example, cobalt has been extensively studied because it is an interesting alternative to noble metals in terms of price, availability, and catalytic efficiency.[6] Several cobalt-based systems have been described as hydrogen evolution reaction (HER) catalysts under the form of molecules,[7−9] amorphous materials,[10,11] or nanoparticles[12,13] (NPs). Cobaloximes, for example, are a class of coordination complexes that have been widely studied in the past decade as molecular electrocatalysts for the reduction of protons into hydrogen.[14] Several recent studies have shown, however, that molecular bis-[15,16] and trisglyoxime[17,18] cobalt complexes dissolved in acetonitrile can be reduced and demetalated at cathodic potentials in the presence of a strong acid to form NPs, which in turn are HER-active under aqueous conditions. We have used in situ X-ray absorption spectroscopy (XAS) to show that the electro-deposited NPs consist of amorphous metallic cobalt, with very small size domains. Tracking the fate of these particles under operating conditions, we found that they are converted to about 50% of their volume into amorphous cobalt(II) phosphate and that the metal/phosphate ratio increases as a more negative electrochemical potential is applied to the electrode. These data provide structural and mechanistic insights on the formation of these particles and their reactivity, suggesting design principles for the improvement of HER-active electrocatalysts under neutral pH. In addition, they are highly relevant to HER catalysis but also to other energy-related reactions such as dioxygen,[19] carbon dioxide[20,21] reduction, or water splitting,[22] all processes for which the structure of metallic catalysts at the solid−liquid interface have been rarely studied.

Received: August 24, 2017
Accepted: October 9, 2017
Published: October 9, 2017

DOI: 10.1021/acsenergylett.7b00789
ACS Energy Lett. 2017, 2, 2545−2551

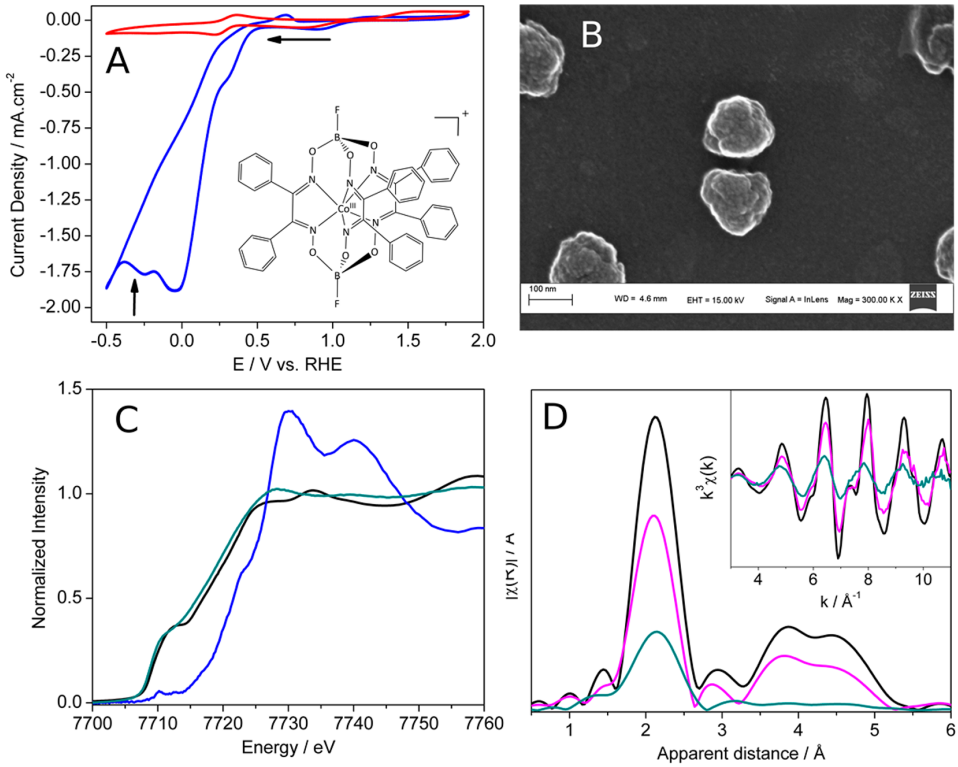

Figure 1. (A) Cyclic voltammograms of a 1 mM solution of $[Co(dpg)_3(BF)_2]^+$ in acetonitrile in the absence (red line) and the presence (blue line) of 30 mM perchloric acid ($HClO_4$); the vertical arrow indicates the potential at which electrodeposition was performed (−0.3 V vs RHE), and the inset shows the structure of the $[Co(dpg)_3(BF)_2]^+$ complex. (B) Electron micrograph of the cobalt NPs after the in situ XAS experiment. (C) XANES spectra (normalized to an edge-jump of 1) at the Co K-edge of a 1 mM solution of the $[Co(dpg)_3(BF)_2]^+$ precursor in acetonitrile (blue line), of a *hcp*-cobalt metal foil (black line), and of the *a*-Co NPs (cyan line). (D) Fourier transform and k^3 (insert) EXAFS spectra of a *hcp*-cobalt metal foil (black line), of *fcc*-cobalt nanorods[24] (magenta line), and of the *a*-Co NPs in acetonitrile (cyan line).

Cobalt Nanoparticle Formation and Structure. A 1 mM acetonitrile solution of the precursor complex $[Co(dpg)_3(BF)_2]^+$, whose structure is shown on Figure 1A, was set in a spectroelectrochemical cell suitable for in situ X-ray spectroscopy,[23] with a glassy carbon (GC) plate as the working electrode (see Figure S1). Figure 1A shows a cyclic voltamogram of this solution in the absence and in the presence of 30 mM perchloric acid ($HClO_4$). In the absence of acid, two successive waves corresponding to the Co^{II}/Co^{III} and Co^{I}/Co^{II} couples[17] are observed. In the presence of acid, the Co^{I}/Co^{II} process is strongly enhanced due to the reduction of the glyoxime ligands, as demonstrated elsewhere.[17] Applying a constant electrochemical potential of E_p = −0.3 V vs RHE leads to the formation of NPs at the surface of the GC electrode. The deposition process was monitored in situ by X-ray absorption near-edge spectroscopy (XANES) at the cobalt K-edge. The resulting particles were observed by scanning electron microscopy (SEM) at the very end of the spectroelectrochemical experiment (see Figure 1B). The NPs were found to be globular, with a diameter of about 100−150 nm but without any preferential growth direction. Figure 1C shows the XANES spectra of the $[Co(dpg)_3(BF)_2]^+$ precursor in acetonitrile and of the NPs deposited after constant potential electrolysis, together with the spectrum of a reference cobalt foil.

The starting $[Co(dpg)_3(BF)_2]^+$ complex in acetonitrile has a spectroscopic signature that is identical to the spectrum of the corresponding powder (see Figure S2), indicating that the geometry of the complex is maintained in acetonitrile. The spectrum of the final species after electrolysis is very similar to that of a reference cobalt foil, suggesting that after deposition the NPs consist of pure metallic cobalt. The differences observed between the two spectra are nevertheless significant. The *hcp* (hexagonal close-packed) form of cobalt is the most frequent and is found in the bulk metal, while *fcc* (face-centered cubic) cobalt is only observed in other elements favoring this structure at the nanoscale[24−26] or in thin films.[27,28] These two structures of cobalt are very close in terms of geometry, but they display slightly different XAS signatures (see Figure S3).[24] The XANES spectrum measured on the Co NPs deposited on the carbon surface does not correspond to the *hcp* nor the *fcc* structures, which suggests a very low order in the material. The Co NPs are thus best described as amorphous cobalt (*a*-Co). This is confirmed by the attenuation of the oscillations in the extended X-ray fine structure (EXAFS) region of the spectrum beyond 7780 eV (see Figure S3), and by the smaller intensity of the k-space signal of the NPs as compared to that of the *fcc*- or *hcp*-Co (see the inset in Figure 1D). The EXAFS Fourier transforms of the two allotropes and of the *a*-Co NPs shown in Figure 1D are in agreement with this attribution: the peak at R' = 2.1 Å, which corresponds to the first-shell Co−Co interaction, is present in both the bulk metals and the NPs, yet with a much smaller intensity for the latter. Even more striking is the absence in the *a*-Co NPs of the Co−Co interactions observed at longer distances with R' = 3.8 and 4.7

DOI: 10.1021/acsenergylett.7b00789
ACS Energy Lett. 2017, 2, 2545−2551

Table 1. Summary of the EXAFS Fit Parameters for a Metallic *hcp*-Cobalt Foil, for Bulk Cobalt(II) Oxide (CoO), for $Co_3(PO_4)_2$, and for the *a*-Co NPs in Acetonitrile and Poised at −1.1 V vs RHE in pH 7 KPi[a]

		r/Å				
sample	shell	XRD	EXAFS	N	σ^2	R/%
Co foil	Co−Co	2.50	2.49 *0.01*	**12**	0.006 *0.001*	1.1
CoO	Co−O	2.13	2.07 *0.03*	**6**	0.010 *0.003*	6.5
	Co−Co	3.01	3.01 *0.02*	**12**	0.007 *0.001*	
$Co_3(PO_4)_2$	Co−O	1.95	1.99 *0.04*	**5.5**	0.004 *0.003*	4.0
a-Co in CH_3CN	Co−Co	–	2.50 *0.01*	7.96 *1.16*	0.013 *0.001*	1.7
a-Co_{ox} in KPi	Co−O	–	1.89 *0.03*	0.53 *0.17*	0.010	0.4
at −1.1 V	Co−Co	–	2.45 *0.01*	5.68 *0.28*	0.010	

[a] *r* is the interatomic distance, *N* is the coordination number, σ^2 is the Debye−Waller factor, and *R* is the goodness of fit. Roman numbers correspond to fixed values, and uncertainties are given in italic.

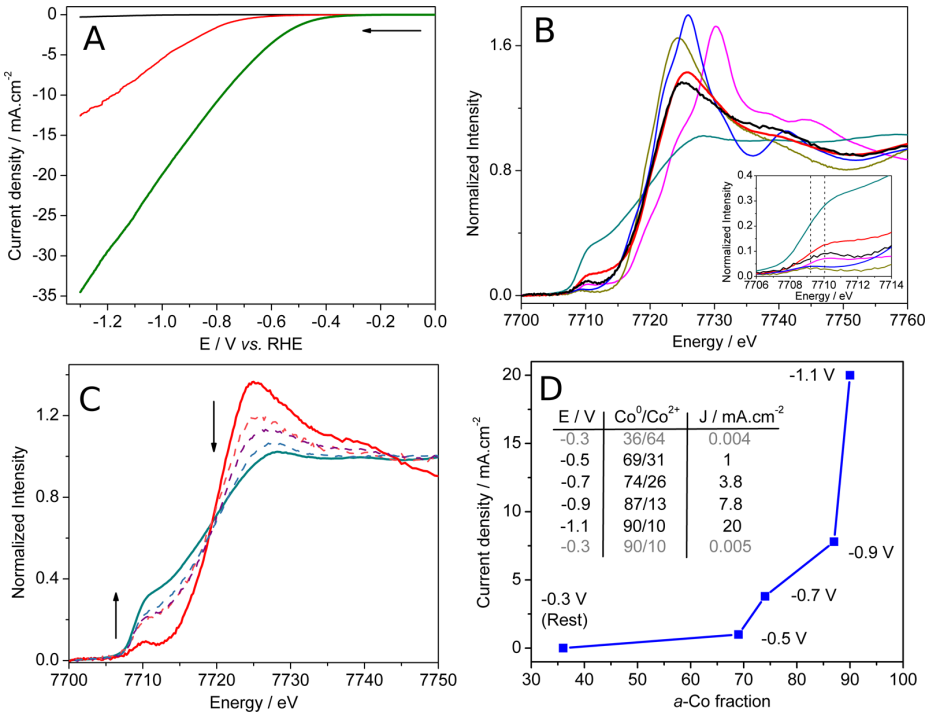

Figure 2. (A) Linear sweep voltammograms of a bare GC electrode (black) and of the *a*-Co NPs in pH 7 KPi before (red line) and after (green line) the X-ray spectroelectrochemical experiment. (B) Co K-edge XANES spectra (normalized to an edge-jump of 1) of the *a*-Co NPs in acetonitrile (cyan line), *a*-Co_{ox} (black line), CoO (blue line), Co_3O_4 (magenta line), and $Co_3(PO_4)_2$ (light green line) and a linear combination spectrum using the *a*-Co NPs (36%), CoO (4.5%), Co_3O_4 (4.5%), and $Co_3(PO_4)_2$ (55%) spectra (red line). The inset shows magnification of the pre-edge region. (C) Co K-edge XANES spectra (normalized to an edge-jump of 1) of *a*-Co_{ox} in a pH 7 potassium phosphate buffer poised at −0.3 (red plain line), −0.5, −0.7, and −0.9 V vs RHE (orange, purple, and cyan dashed lines, respectively) and of *a*-Co in acetonitrile as a comparison (plain cyan line). (D) Plot of the current density as a function of the metallic fraction in the NPs. The corresponding electrochemical potentials are indicated next to each data point, and the inset table indicates the Co^0/Co^{2+} fractions (in %) and current densities for each potential as determined by the XANES linear combination fittings.

Å in the metallic cobalt forms. Fitting the EXAFS data, we determined (see Figure 3B and Table 1) an average number of ca. 8 Co first neighbors at a distance of 2.50 Å, which corresponds to a cluster size of about 1 nm, made of ca. 55 cobalt atoms (see Table S1). Our data were correctly simulated using only one Co−Co shell, which further supports the amorphous nature of the electrodeposited NPs. Although the presence of impurities cannot be ruled out, the formation of a distinct CoB phase (with boron originating from the organic ligands of the starting compound) is excluded by the very different XANES spectrum obtained for this species (see Figure S4). The electrodeposited NPs can therefore be described as porous assemblies of about 100 nm made of smaller clusters of amorphous cobalt of ∼1 nm each. The formation of such small clusters of amorphous cobalt at room temperature under mild conditions is quite unexpected and in sharp contrast with the strictly controlled conditions usually described to produce such species.[24−28] It is noteworthy, however, that chemical routes for the room-temperature preparation of amorphous cobalt NPs have already been reported.[29,30] We hypothesize that the presence of the glyoxime decomposition fragments around the cobalt ions as well as the coordinating nature of acetonitrile is

DOI: 10.1021/acsenergylett.7b00789
ACS Energy Lett. 2017, 2, 2545−2551

Scheme 1. Proposed Structures of the *a*-Co and *a*-Co_{ox} 55 Atom Clusters and Schematic Representation of the Overall Behavior of the NPs in Acetonitrile and in pH 7 KPi Buffer under Resting and HER Conditions

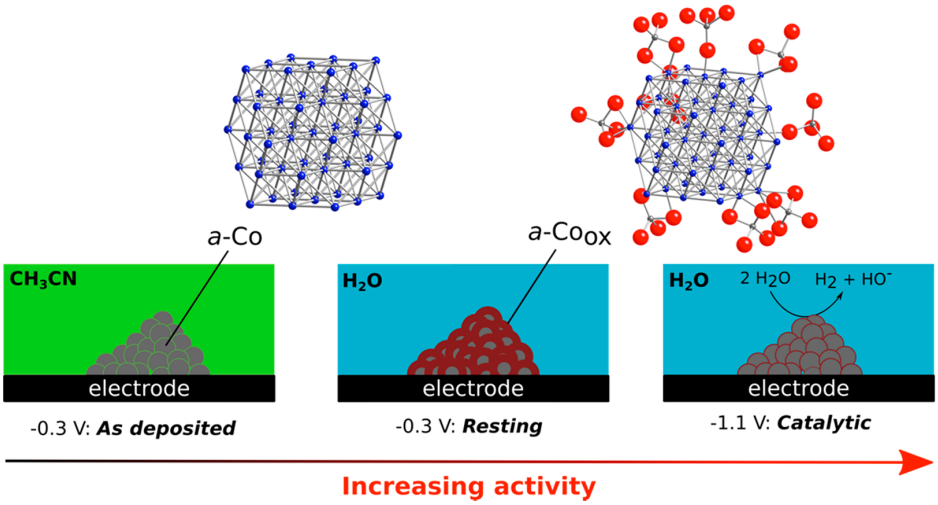

preventing the formation of larger crystalline domains during the NP growth. Such effects have already been reported for the formation of *a*-Co NPs in dimethyl sulfoxide (DMSO), another coordinating solvent.[29]

Structural Evolution under Aqueous Conditions. After electrochemical deposition of the NPs, the acetonitrile precursor solution was replaced by a 0.1 M degassed potassium phosphate (KPi) aqueous solution (pH 7). A linear sweep voltamogram (LSV) of the NPs under these conditions is displayed in Figure 2A, showing their proton reducing ability as compared to a bare GC electrode. Under aqueous conditions, the XANES spectrum is drastically modified (see Figure 2B, black line) as compared to the starting spectrum of *a*-Co (see Figure 2B, cyan line), suggesting oxidation of the metallic cobalt and important changes in the first coordination sphere. The spectrum of the new species, which we will refer to as *a*-Co_{ox}, is compared to those of cobalt oxides (CoO and Co_3O_4) and cobalt(II) phosphate ($Co_3(PO_4)_2$). The pre-edge feature of *a*-Co_{ox} at E = 7710.3 eV is 1 eV higher in energy and about twice as high in intensity than those of CoO or $Co_3(PO_4)_2$ (E = 7709.3 eV for both species). On the contrary, it presents a good match with the pre-edge feature of Co_3O_4, whose intensity arises from the presence of tetrahedral sites in this spinel structure. Given the position of the main edge peak top in *a*-Co_{ox} (E = 7724.8 eV) and its overall shape, $Co_3(PO_4)_2$ (E = 7724.4 eV) seems a better match than CoO (E = 7725.9 eV). Suspecting a partial conversion of the starting *a*-Co NPs into an oxidized species, we performed linear combination fittings of the *a*-Co_{ox} spectrum using the spectra of the starting *a*-Co NPs and of CoO, Co_3O_4, or $Co_3(PO_4)_2$ (see Figure S5A–C). It appears that using $Co_3(PO_4)_2$ as a reference sample gives a much better fit (r-χ^2 = 0.0012) than using CoO (r-χ^2 = 0.0046) or Co_3O_4 (r-χ^2 = 0.0229). Performing a fit with the three reference samples (see Figure S5D) led to a fit of good quality (r-χ^2 = 0.0014), where the phosphate contribution remained the major one (55%) and the oxides contribution was minor (ca. 5% each). The good match between pure Co_3O_4 and *a*-Co_{ox} in the pre-edge region nevertheless suggests the presence of nonoctahedral (5- or 4-fold coordinated) sites in the *a*-Co_{ox} species. Such defective cobalt oxides have been observed previously at the nanoscale[24,31] and can be rationalized in the present case by the coordination of phosphate and/or oxygen ligands in a nonoctahedral geometry at the solid–liquid interface.[32] In view of these data, we propose a model (see Scheme 1) where each cluster composing the *a*-Co particles has been partially oxidized at the solid–liquid interface, where they are coordinated either by oxygens or by phosphate ligands (hence the remaining fraction of starting *a*-Co at the core of the clusters). Given the size of the *a*-Co clusters (ca. 50 atoms), about 75% of the cobalt atoms are located on the outer shell, while only 25% (13 atoms) are in the core of the clusters. Considering that the clusters are not entirely in contact with the liquid media due to contacts between clusters, a ca. 50% conversion to Co(II) upon exposure to the electrolyte matches this structural model.

Structural Evolution under Catalytic Potential. We probed the structural evolution of the *a*-Co_{ox} NPs under catalytic conditions, using operando cobalt K-edge XANES. Figure 2C shows the spectra of the *a*-Co_{ox} NPs in aqueous KPi at pH 7 poised at −0.3 V vs RHE and at increasing cathodic potentials (−0.5, −0.7, and −0.9 V vs RHE). As the potential is set to more negative values, the spectra evolve toward a lower amount of cobalt(II) and a higher amount of metal. Each spectrum was fitted with linear combinations of the *a*-Co, CoO, Co_3O_4, and $Co_3(PO_4)_2$ spectra (see Figure S6 and Table S2) to determine the fraction of the three components. We found that CoO is negligible, independent of the potential, while the fraction of Co_3O_4 remains close to 5%. The cobalt(II) phosphate fraction and the metallic cobalt one are inversely linked to each other: the former decreases with more negative potentials while the latter increases. Figure 2D shows that the current density from HER activity increases with the metallic fraction, which clearly indicates that the active species is metallic cobalt. The starting, purely metallic cobalt composition observed in acetonitrile is, however, never recovered, the highest fraction of *a*-Co being ca. 90% at −1.1 V vs RHE. It should be noted that when the potential is set back to a resting (noncatalytically active) value of −0.3 V the Co^0/Co^{2+} fraction remains identical (90:10) to that obtained at a high catalytic potential (−1.1 V vs RHE), while the current density goes down to 0 mA·cm^{-2}. A LSV was

DOI: 10.1021/acsenergylett.7b00789
ACS Energy Lett. 2017, 2, 2545–2551

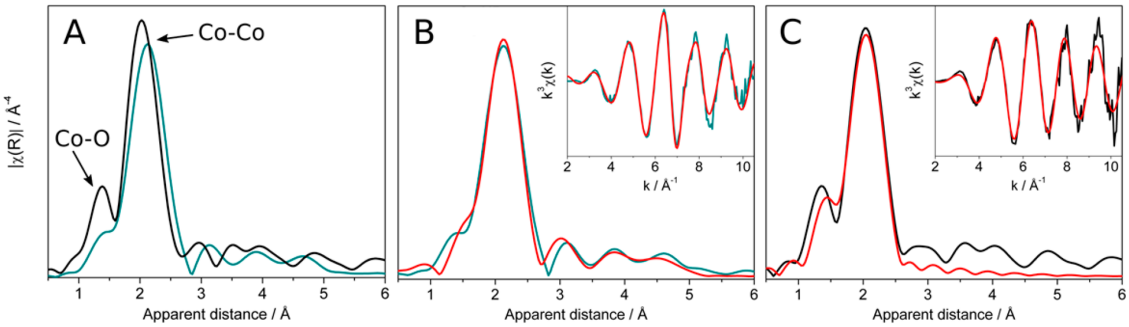

Figure 3. EXAFS Fourier transforms of (A) the *a*-Co NPs in acetonitrile (cyan line) and of the *a*-Co_{ox} NPs poised at −1.1 V in aqueous KPi at pH 7 (black line). (B) Fit to the *a*-Co NPs in acetonitrile (red line) compared to the experimental data (cyan line) and (C) fit to the *a*-Co_{ox} NPs poised at −1.1 V in aqueous KPi pH 7 (red line) compared to the experimental data (black line). The insets show the corresponding k-space experimental spectra (cyan, black lines) and fits (red lines).

recorded (see Figure 2A, green trace) at the end of the experiment, showing that the onset of catalysis is decreased by about 300 mV as compared to the first LSV recorded at the beginning of the experiment. These improved performances indicate that the material has been activated by application of a highly cathodic potential that led to the reduction of a substantial part of the oxidized layer in the NPs, thus exposing a higher surface of active metal.

In order to better describe the structure of the NPs under catalytic conditions, EXAFS data were collected on the electrode poised at −1.1 V vs. RHE. Figure 3A shows the EXAFS Fourier transform of *a*-Co in acetonitrile and of *a*-Co_{ox} in pH 7 KPi with the electrode potential set at −1.1 V vs RHE (catalytic conditions). The contribution of a short interaction at R' = 1.40 Å (R_{eff} = 1.89 Å) clearly stands out in *a*-Co_{ox} at −1.1 V vs RHE as compared to the starting *a*-Co NPs. Comparing the first peak position in the Fourier transform of *a*-Co_{ox} poised at −1.1 V vs RHE with CoO and $Co_3(PO_4)_2$ (see Figure S7) strongly suggests that the short interaction in *a*-Co_{ox} arises from the coordination of phosphates to the cobalt ions. This is further supported by the fit performed on the spectrum of *a*-Co_{ox} poised at −1.1 V vs RHE, which is shown in Figure 3C (see fitting parameters in Tables 1 and S3). The fit shows that the number of oxygen first neighbors is about 0.5, while the number of Co first neighbors is about 5 (see Tables 1 and S1). This ratio corresponds to the ca. 10% remaining oxidized form at this potential, as determined from XANES linear combination fittings. The Co−O distance found for *a*-Co_{ox} sample is significantly shorter than that found in CoO or $Co_3(PO_4)_2$, which can be rationalized by the presence of terminal, oxygen-based ligands (oxo, hydroxo, or phosphato), which are expected to make shorter bonds than their bridging counterparts. It should be noted that at very negative potentials (E < −0.5 V) the XANES linear combination fittings could not accurately distinguish between an oxide or a phosphate form for the Co^{2+} contribution. The presence of cobalt(II) oxide/hydroxide phases at these very negative potentials could be explained by the production of hydroxide anions by the HER reaction itself at neutral pH.

An overall picture of the structure and behavior of the cobalt-based HER electrocatalyst described in this study is summarized in Scheme 1. The ill-defined, porous nanostructure of this material is certainly playing an important role in its catalytic activity, particularly in the activation process that occurs when a very negative potential is applied. After the purely metallic particles partly convert to cobalt(II) in contact with the aqueous phosphate buffer, the application of a negative potential converts them back into metallic cobalt, although not completely. The highest cathodic potential applied in our study was −1.1 V vs RHE, which appeared to be an efficient way of converting back the thick, outer shell of oxidized cobalt into the metal, thus increasing the catalytically active surface. Moreover, this cobalt(II)-to-metal conversion is irreversible because the ratio observed after the activation process remains in favor of the metal for several hours. The activation of HER catalysts by applying a "burst" potential beyond the operating potential could therefore be used to convert the outermost layer of a catalyst and improve its activity at a lower potential.

The use of transition metal phosphates has been the subject of many studies for the oxygen-evolving reaction (OER). A few studies have also been directed toward utilizing and understanding these systems under HER conditions at neutral pH.[10,33−36] For example, a study by Cobo et al. suggested that cobalt(II) phosphate could be used as a bifunctional OER/HER catalyst.[10] More recently, Takanabe et al. have shown that the buffer concentration can play a significant role in the HER activity of metallic catalysts under neutral pH.[34] Our study shows that the coordinating nature of the buffer also has a significant effect on the chemical structure of the catalyst at the interface with the liquid medium and hence on its catalytic activity. Tuning the ability of the electrolyte components to bind to the catalyst itself while maintaining its buffering action on the reaction medium could therefore lead to improved activity.

On a broader perspective, metal/metal oxide core/shell materials are currently under scrutiny for overall photocatalytic water-splitting systems[37−39] or carbon dioxide reduction reactions.[40−42] Our study shows that understanding the structural modifications of metal catalysts at the solid−liquid interface is critical to energy-related catalysis and that operando X-ray techniques are powerful tools to study it.

■ ASSOCIATED CONTENT

Supporting Information

The Supporting Information is available free of charge on the ACS Publications website at DOI: 10.1021/acsenergylett.7b00789.

Experimental conditions, detailed spectroelectrochemical setup, additional XAS spectra, as well as EXAFS fitting parameters (PDF)

DOI: 10.1021/acsenergylett.7b00789
ACS Energy Lett. 2017, 2, 2545−2551

AUTHOR INFORMATION

Corresponding Authors

*E-mail: benedikt.lassalle@synchrotron-soleil.fr (B.L.-K.).
*E-mail: elodie.anxolabehere@univ-paris-diderot.fr (E.A.-M.).

ORCID

Benedikt Lassalle-Kaiser: 0000-0003-2141-2496
Marc Robert: 0000-0001-7042-4106
Elodie Anxolabéhère-Mallart: 0000-0002-8708-802X

Notes

The authors declare no competing financial interest.

ACKNOWLEDGMENTS

Financial support from Agence Nationale de la Recherche (ANR 2010 BLAN 0808) is acknowledged. H. Lecoq is gratefully thanked for recording SEM images. Drs. D. Portehault and G. Gouget from the Laboratoire de Chimie de la Matière Condensée de Paris, Université Pierre and Marie Curie in Paris are acknowledged for generously providing a CoB reference sample.

REFERENCES

(1) Lewis, N. S.; Nocera, D. G. Powering the planet: Chemical challenges in solar energy utilization. *Proc. Natl. Acad. Sci. U. S. A.* **2006**, *103*, 15729−15735.

(2) Armaroli, N.; Balzani, V. The future of energy supply: Challenges and opportunities. *Angew. Chem., Int. Ed.* **2007**, *46*, 52−66.

(3) Nocera, D. G. Chemistry of Personalized Solar Energy. *Inorg. Chem.* **2009**, *48*, 10001−10017.

(4) Tatin, A.; Bonin, J.; Robert, M. A Case for Electrofuels. *ACS Energy Lett.* **2016**, *1*, 1062−1064.

(5) Turner, J. A. A realizable renewable energy future. *Science* **1999**, *285*, 687−689.

(6) Artero, V.; Chavarot-Kerlidou, M.; Fontecave, M. Splitting Water with Cobalt. *Angew. Chem., Int. Ed.* **2011**, *50*, 7238−7266.

(7) Jacobsen, G. M.; Yang, J. Y.; Twamley, B.; Wilson, A. D.; Bullock, R. M.; Rakowski DuBois, M.; DuBois, D. L. Hydrogen production using cobalt-based molecular catalysts containing a proton relay in the second coordination sphere. *Energy Environ. Sci.* **2008**, *1*, 167−174.

(8) Jacques, P.-A.; Artero, V.; Pecaut, J.; Fontecave, M. Cobalt and nickel diimine-dioxime complexes as molecular electrocatalysts for hydrogen evolution with low overvoltages. *Proc. Natl. Acad. Sci. U. S. A.* **2009**, *106*, 20627−20632.

(9) Sun, Y.; Bigi, J. P.; Piro, N. A.; Tang, M. L.; Long, J. R.; Chang, C. J. Molecular Cobalt Pentapyridine Catalysts for Generating Hydrogen from Water. *J. Am. Chem. Soc.* **2011**, *133*, 9212−9215.

(10) Cobo, S.; Heidkamp, J.; Jacques, P.-A.; Fize, J.; Fourmond, V.; Guetaz, L.; Jousselme, B.; Ivanova, V.; Dau, H.; Palacin, S.; et al. A Janus cobalt-based catalytic material for electro-splitting of water. *Nat. Mater.* **2012**, *11*, 802−807.

(11) Kornienko, N.; Resasco, J.; Becknell, N.; Jiang, C.-M.; Liu, Y.-S.; Nie, K.; Sun, X.; Guo, J.; Leone, S. R.; Yang, P. Operando Spectroscopic Analysis of an Amorphous Cobalt Sulfide Hydrogen Evolution Electrocatalyst. *J. Am. Chem. Soc.* **2015**, *137*, 7448−7455.

(12) Popczun, E. J.; Read, C. G.; Roske, C. W.; Lewis, N. S.; Schaak, R. E. Highly Active Electrocatalysis of the Hydrogen Evolution Reaction by Cobalt Phosphide Nanoparticles. *Angew. Chem., Int. Ed.* **2014**, *53*, 5427−5430.

(13) Jin, H.; Wang, J.; Su, D.; Wei, Z.; Pang, Z.; Wang, Y. In situ Cobalt-Cobalt Oxide/N-Doped Carbon Hybrids As Superior Bifunctional Electrocatalysts for Hydrogen and Oxygen Evolution. *J. Am. Chem. Soc.* **2015**, *137*, 2688−2694.

(14) Dempsey, J. L.; Brunschwig, B. S.; Winkler, J. R.; Gray, H. B. Hydrogen Evolution Catalyzed by Cobaloximes. *Acc. Chem. Res.* **2009**, *42*, 1995−2004.

(15) Anxolabéhère-Mallart, E.; Costentin, C.; Fournier, M.; Robert, M. Cobalt-Bisglyoximato Diphenyl Complex as a Precatalyst for Electrocatalytic H_2 Evolution. *J. Phys. Chem. C* **2014**, *118*, 13377−13381.

(16) Sconyers, D. J.; Blakemore, J. D. Distinguishing between homogeneous and heterogeneous hydrogen-evolution catalysis with molecular cobalt complexes. *Chem. Commun.* **2017**, *53*, 7286−7289.

(17) Anxolabéhère-Mallart, E.; Costentin, C.; Fournier, M.; Nowak, S.; Robert, M.; Savéant, J.-M. Boron-Capped Tris(glyoximato) Cobalt Clathrochelate as a Precursor for the Electrodeposition of Nanoparticles Catalyzing H_2 Evolution in Water. *J. Am. Chem. Soc.* **2012**, *134*, 6104−6107.

(18) El Ghachtouli, S.; Fournier, M.; Cherdo, S.; Guillot, R.; Charlot, M.-F.; Anxolabéhère-Mallart, E.; Robert, M.; Aukauloo, A. Monometallic Cobalt-Trisglyoximato Complexes as Precatalysts for Catalytic H_2 Evolution in Water. *J. Phys. Chem. C* **2013**, *117*, 17073−17077.

(19) Friebel, D.; Miller, D. J.; O'Grady, C. P.; Anniyev, T.; Bargar, J.; Bergmann, U.; Ogasawara, H.; Wikfeldt, K. T.; Pettersson, L. G. M.; Nilsson, A. In situ X-ray probing reveals fingerprints of surface platinum oxide. *Phys. Chem. Chem. Phys.* **2011**, *13*, 262−266.

(20) Li, C. W.; Kanan, M. W. CO_2 Reduction at Low Overpotential on Cu Electrodes Resulting from the Reduction of Thick Cu2O Films. *J. Am. Chem. Soc.* **2012**, *134*, 7231−7234.

(21) Chen, Y.; Kanan, M. W. Tin Oxide Dependence of the CO_2 Reduction Efficiency on Tin Electrodes and Enhanced Activity for Tin/Tin Oxide Thin-Film Catalysts. *J. Am. Chem. Soc.* **2012**, *134*, 1986−1989.

(22) Townsend, T. K.; Browning, N. D.; Osterloh, F. E. Overall photocatalytic water splitting with NiO_x-$SrTiO_3$ - a revised mechanism. *Energy Environ. Sci.* **2012**, *5*, 9543−9550.

(23) Lassalle-Kaiser, B.; Gul, S.; Kern, J.; Yachandra, V. K.; Yano, J. In situ/Operando studies of electrocatalysts using hard X-ray spectroscopy. *J. Electron Spectrosc. Relat. Phenom.* **2017**, DOI: 10.1016/j.elspec.2017.05.001.

(24) Novikova, A.; Fonda, E.; Dumont, Y.; Zheng, Y.; Demaille, D.; Vidal, F. Structural stability of cobalt ferromagnetic nanowires embedded in CeO_2/$SrTiO_3$(001) after oxidative/reductive annealing. *J. Phys. D: Appl. Phys.* **2015**, *48*, 235001 DOI: 10.1088/0022-3727/48/23/235001.

(25) Castaner, R.; Prieto, C.; de Andres, A.; Martinez, J. L.; Martinez-Albertos, J. L.; Ocal, C.; Miranda, R. The structural characterization of Co-Cu(100) Superlattices by X-ray absorption spectroscopy. *J. Phys.: Condens. Matter* **1994**, *6*, 4981−4990, DOI: 10.1088/0953-8984/6/27/007.

(26) Zhang, G. L.; Wu, Z. Y.; Li, A. G.; Wang, Y. S.; Zhang, J.; Abbas, M. I.; Hu, R.; Ni, X. B.; Tong, Y. P.; Hwu, Y. K. XANES investigation of the local structure of Co nanoclusters embedded in Ag. *Phys. Rev. B: Condens. Matter Mater. Phys.* 2004, *69*, 10.1103/PhysRevB.69.115405.

(27) Magnan, H.; Chandesris, D.; Rossi, G.; Jezequel, G.; Hricovini, K.; Lecante, J. Determination of the local order in amorphous cobalt films. *Phys. Rev. B: Condens. Matter Mater. Phys.* **1989**, *40*, 9989−9992.

(28) Miyawaki, J.; Matsumura, D.; Nojima, A.; Yokoyama, T.; Ohta, T. Structural study of Co/Pd(111) and CO/Co/Pd(111) by surface X-ray absorption fine structure spectroscopy. *Surf. Sci.* **2007**, *601*, 95−103.

(29) Duggan, J. N.; Bozack, M. J.; Roberts, C. B. The synthesis and arrested oxidation of amorphous cobalt nanoparticles using DMSO as a functional solvent. *J. Nanopart. Res.* **2013**, DOI: 10.1007/s11051-013-2089-0.

(30) Song, Y.; Henry, L. L.; Yang, W. Stable Amorphous Cobalt Nanoparticles Formed by an in Situ Rapidly Cooling Microfluidic Process. *Langmuir* **2009**, *25*, 10209−10217.

(31) Zheng, F.; Alayoglu, S.; Guo, J.; Pushkarev, V.; Li, Y.; Glans, P.-A.; Chen, J.; Somorjai, G. In-situ X-ray Absorption Study of Evolution of Oxidation States and Structure of Cobalt in Co and CoPt Bimetallic Nanoparticles (4 nm) under Reducing (H_2) and Oxidizing (O_2) Environments. *Nano Lett.* **2011**, *11*, 847−853.

(32) Hunault, M.; Robert, J.-L.; Newville, M.; Galoisy, L.; Calas, G. Spectroscopic properties of five-coordinated Co^{2+} in phosphates. *Spectrochim. Acta, Part A* **2014**, *117*, 406−412.

DOI: 10.1021/acsenergylett.7b00789
ACS Energy Lett. 2017, 2, 2545−2551

(33) Sun, Y.; Liu, C.; Grauer, D. C.; Yano, J.; Long, J. R.; Yang, P.; Chang, C. J. Electrodeposited Cobalt-Sulfide Catalyst for Electrochemical and Photoelectrochemical Hydrogen Generation from Water. *J. Am. Chem. Soc.* **2013**, *135*, 17699−17702.
(34) Shinagawa, T.; Takanabe, K. Electrocatalytic Hydrogen Evolution under Densely Buffered Neutral pH Conditions. *J. Phys. Chem. C* **2015**, *119*, 20453−20458.
(35) Shinagawa, T.; Takanabe, K. New Insight into the Hydrogen Evolution Reaction under Buffered Near-Neutral pH Conditions: Enthalpy and Entropy of Activation. *J. Phys. Chem. C* **2016**, *120*, 24187−24196.
(36) De Silva Munoz, L.; Bergel, A.; Feron, D.; Basseguy, R. Hydrogen production by electrolysis of a phosphate solution on a stainless steel cathode. *Int. J. Hydrogen Energy* **2010**, *35*, 8561−8568.
(37) Zhang, L.; Liu, Q.; Aoki, T.; Crozier, P. A. Structural Evolution during Photocorrosion of Ni/NiO Core/Shell Cocatalyst on TiO_2. *J. Phys. Chem. C* **2015**, *119*, 7207−7214.
(38) Yoshida, M.; Takanabe, K.; Maeda, K.; Ishikawa, A.; Kubota, J.; Sakata, Y.; Ikezawa, Y.; Domen, K. Role and Function of Noble-Metal/Cr-Layer Core/Shell Structure Cocatalysts for Photocatalytic Overall Water Splitting Studied by Model Electrodes. *J. Phys. Chem. C* **2009**, *113*, 10151−10157.
(39) Nail, B. A.; Fields, J. M.; Zhao, J.; Wang, J.; Greaney, M. J.; Brutchey, R. L.; Osterloh, F. E. Nickel Oxide Particles Catalyze Photochemical Hydrogen Evolution from Water-Nanoscaling Promotes P-Type Character and Minority Carrier Extraction. *ACS Nano* **2015**, *9*, 5135−5142.
(40) Xie, S.; Zhang, Q.; Liu, G.; Wang, Y. Photocatalytic and photoelectrocatalytic reduction of CO_2 using heterogeneous catalysts with controlled nanostructures. *Chem. Commun.* **2016**, *52*, 35−59.
(41) Zhai, Q.; Xie, S.; Fan, W.; Zhang, Q.; Wang, Y.; Deng, W.; Wang, Y. Photocatalytic Conversion of Carbon Dioxide with Water into Methane: Platinum and Copper(I) Oxide Co-catalysts with a Core-Shell Structure. *Angew. Chem., Int. Ed.* **2013**, *52*, 5776−5779.
(42) Tsai, C.-W.; Chen, H. M.; Liu, R.-S.; Asakura, K.; Chan, T.-S. Ni@NiO Core-Shell Structure-Modified Nitrogen-Doped $InTaO_4$ for Solar-Driven Highly Efficient CO_2 Reduction to Methanol. *J. Phys. Chem. C* **2011**, *115*, 10180−10186.

DOI: 10.1021/acsenergylett.7b00789
ACS Energy Lett. 2017, 2, 2545−2551